



Aalto-yliopisto
Insinöörیتieteiden
korkeakoulu

Taiquan Liu

Thermal Management Solutions for Battery Electric Buses in Cold Climates

Master's Thesis
Aalto University
School of Engineering
Department of Mechanical Engineering

Thesis submitted as partial fulfilment of the requirements for
the degree of Master of Science in Technology

Espoo 21.08.2019
Supervisor: Professor Kari Tammi
Advisor: Pekka Rahkola

Author Taiquan Liu

Title of thesis Thermal management solutions for battery electric city buses in cold climates

Master programme Master's Programme in Mechanical Engineering

Code ENG25

Thesis supervisor Professor Kari Tammi

Thesis advisor(s) Pekka Rahkola

Date 21.08.2019

Number of pages 108

Language English

Abstract

In many cities around the world, electric buses including battery electric buses have been replacing traditional diesel-powered buses because of their benefit for the urban environment. Cabin thermal management is one of the prominent issues that prevent battery electric buses being widely used in cold climate such as Finland. Current solutions such as heat pumps and fuel burning air heaters could not totally satisfy the needs. The thesis evaluates several innovative thermal management solutions with the objectives of improving the cabin heating performance and driving range in cold conditions.

In the thesis, a system-level battery electric bus simulation model was developed using the Siemens AMESim software, based on the electric bus prototype e-Muuli of VTT. The simulation model uses multi-level simulation approach and focuses on the details of thermal simulation; the model includes a detailed cabin thermal model as well as a heating, ventilation and air conditioning (HVAC) system model. The powertrain, cabin, and HVAC simulation models are validated by experiments carried out on e-Muuli.

Based on the battery electric bus simulation model, several innovative thermal management solutions are developed, including positive temperature coefficient (PTC) heater, powertrain waste energy harvesting through the chiller (liquid-to-air heat pump), and thermal energy storage using phase change material (PCM). Different configurations are tested in real-world driving cycles in different ambient temperature from -20°C to 40°C. Some other factors, such as air flow through doors, passenger load, and heat generation from passengers are also considered in the simulation.

The simulation results show that low ambient temperatures will result in higher energy consumption and lower driving range. Compared to 20 °C, the driving range is reduced by 40% while using heat pump in -20 °C. Using PTC heater with heat pump will improve cabin heating performance but further reduce range. Combining a heat pump with the chiller, PCM, chiller and PCM respectively will improve the driving range by 8%, 23%, 24% in -20 °C. The simulation results also showed that frequent opening of bus doors will cause a significant difference in energy consumption for cabin heating, which is a factor that previous studies have not considered.

Keywords battery electric city bus; thermal management; system-level simulation; heating, ventilation and air conditioning (HVAC); heat pump; cabin; positive temperature coefficient (PTC) heater; phase change material (PCM)

Starting Words

The thesis work is accomplished in VTT Technical Research Centre of Finland, Electrical Powertrain and Storage research team. Because of the needs for improving the auxiliary calculation in an electric bus fleet simulation tool developed by the team, the topic of investigating HVAC consumption on battery electric city buses was drawn up. The topic was later extended to thermal management solutions for battery electric city buses. The funding of the thesis is from internal project funding in VTT.

During the thesis, I received assistance and help from many. My advisor, Pekka Rahkola provided knowledge in powertrain simulation and validation, and held weekly meeting with me to discuss the progress of the thesis. Jari Haavisto, Hannu Kuutti, and other colleagues in VTT offered technical help in setting up experiments for model validation. Professor Kari Tammi gave valuable suggestion in writing the thesis. I would like to give my sincere thanks to everyone who is involved. I am grateful for Mikko Pihlatie who offer me the chance to have my thesis work done in the research team, as well as the workplace and generous funding provided by VTT.

Espoo 21.08.2019

Taiquan Liu

Taiquan Liu

Table of Contents

Abstract.....	3
Starting Words	4
Abbreviations and Acronyms	8
1 Introduction	9
1.1 Thermal Management Systems for Conventional Vehicles.....	9
1.2 Thermal Management Systems for Electric Vehicles.....	11
1.2.1 Heat Pump.....	12
1.2.2 Thermal Energy Storage.....	13
1.2.3 Integrated Thermal Management.....	14
1.2.4 Other Approaches	15
1.3 Vehicle Cabin Simulation	16
1.3.1 Mono-zonal Model	16
1.3.2 Computational Fluid Dynamics (CFD) Model.....	17
1.3.3 Other Approaches	18
1.4 Tools for EV Thermal Simulations	19
1.5 Research Aims, Methods, and Scope.....	21
1.5.1 Research Aims	21
1.5.2 Simulation Tools and Methods.....	21
1.5.3 Research Scope.....	22
1.6 Thesis Structure Overview.....	23
2 Background Knowledge	23
2.1 Thermodynamics Basics	23
2.1.1 Heat Transfer	23
2.1.2 Phases of a Substance and Pressure-Enthalpy (PH) Diagram	24
2.2 HVAC Basics.....	26
2.2.1 Compressor, Condenser, Evaporator and Vapour Compression Cycle.....	27
2.2.2 Receiver-Drier	29
2.2.3 Accumulator.....	29
2.2.4 Metering Device – Thermal Expansion Valve	30
3 Formulation of the Simulation Model	33
3.1 The e-Muuli Prototype Bus.....	33
3.2 Simulation Model Overview	34
3.3 Driver and Vehicle Control.....	34
3.3.1 Driver.....	35
3.3.2 Vehicle Control Unit.....	36
3.4 Powertrain	37
3.4.1 Motor	38

3.4.2	Inverter.....	39
3.4.3	Body of the Bus	40
3.5	Battery	43
3.5.1	High Voltage Battery	43
3.5.2	Low Voltage Battery and Auxiliaries	45
3.6	Powertrain Cooling Loop.....	46
3.7	Cabin	48
3.7.1	Interfaces.....	49
3.7.2	Doors Opening Model	50
3.7.3	Air Infiltration.....	53
3.7.4	Human Factor	53
3.7.5	Solar Effects.....	53
3.8	Heating, Ventilation and Air Conditioning (HVAC) System	55
3.8.1	Compressor	57
3.8.2	Heat Exchangers	58
3.8.3	Thermal Expansion Valve	63
3.8.4	Blower and Fan.....	64
3.9	Thermal Management Controller.....	65
4	Model Characterization and Validation.....	67
4.1	HVAC Characterization	67
4.1.1	Temperature Characteristics	67
4.1.2	Compressor Characteristics	70
4.1.3	Blower Characteristics.....	71
4.1.4	Comparison to Eberspächer AC136 AE HP	72
4.2	Powertrain Cooling Performance.....	73
4.3	Powertrain Validation – Dynamometer Experiment.....	74
4.3.1	Experiment Setup.....	75
4.3.2	Results and Discussion	76
4.4	Thermal Validation – Temperature Experiments.....	77
4.4.1	Experiment Setup.....	77
4.4.2	Cabin Cool-down Test.....	81
4.4.3	Heat Pump Test.....	82
4.4.4	Results and Discussion	83
5	Thermal Management Solutions.....	86
5.1	Thermal Management Solutions and Modelling.....	86
5.1.1	Positive Temperature Coefficient (PTC) Heater	86
5.1.2	Powertrain Waste Energy Harvesting through Chiller	86

5.1.3	Thermal Energy Storage through Phase Change Material (PCM)	90
5.2	Simulation Setup	92
5.2.1	Driving Cycle	92
5.2.2	Thermal Management Configurations	95
5.3	Simulation Results	95
5.3.1	Heat Pump Results	97
5.3.2	PTC Heater Results	97
5.3.3	Chiller Results	98
5.3.4	PCM Heating Loop Results	98
5.3.5	Doors Opening Model	98
5.3.6	Driving Range	99
5.4	Results Discussion	100
6	Conclusion	103
6.1	Thesis Outcome	103
6.2	Limitations and Recommendations for Future Research	103
	Reference	105

Abbreviations and Acronyms

AC	air conditioning
AC	alternating current
AE	all-electric
CAD	computer-aided design
CFD	computational fluid dynamics
COP	coefficient of performance
DC	direct current
DSC	differential scanning calorimeter
EHX	external heat exchanger
EV	electric vehicle
GWP	global warming potential
HP	heat pump
HVAC	heating, ventilation, and air conditioning
ICE	internal combustion engine
IHX	internal heat exchanger
LTO	lithium-titanate
OCV	open circuit voltage
PCM	phase change material
PH	pressure-enthalpy
PMSM	permanent magnet synchronous motor
PTC	positive temperature coefficient
RMS	root mean square
RMSE	root mean square error
RV	recreational vehicle
SOC	state of charge
TMC	thermal management controller
TXV	thermal expansion valve
VCU	vehicle control unit

1 Introduction

Electric buses include hybrid electric, fuel cell electric, and battery electric buses (Mahmoud *et al.*, 2016). There are substantial environmental benefits in utilizing electric city buses. The simulation done by Lajunen and Lipman (2016) shows that hybrid and battery electric buses have much higher energy efficiency and lower local emission than traditional diesel and natural gas powered buses; the energy reduction potential for electric buses is as high as 75% due to high efficiency and regenerative braking.

With the rapid development of electric powertrain, battery and charging technology, electric buses, particularly battery electric buses, have gained popularity among many city bus operators around the globe. There are more than 40 cities in the world operating battery electric buses, with many more operating hybrid electric buses (International Energy Agency, 2018; Li, Castellanos and Maassen, 2018). Helsinki Region Transport Authority (HRT, or HSL) is also increasing the numbers of battery electric buses in city buses' fleet of Helsinki. There will be 30 new battery electric buses entering service by the autumn of 2019 and 30% of the buses in Helsinki will be electric by the year 2025 (HSL, 2018).

Despite the rapid growth, there are still some issues that need to be to further improve efficiency and decrease emission for electric buses. One specific issue for battery electric buses to be operated in cold climate region such as Finland is optimising thermal management of buses (Pihlatie *et al.*, 2015). In Helsinki, the buses could be operated in a temperature range from -20°C to 30°C . Innovative cabin thermal management solutions are needed for the extreme temperatures.

The thesis work is accomplished in VTT Technical Research Centre of Finland, Electrical Powertrain and Storage research team. The team is specialised in electric transportation topics such as electric buses powertrain, battery, and fleet simulation. The thesis work provides insights for future electric bus research. The simulation data for energy consumption in different environment are used improve an electric bus fleet simulation tool developed by the team.

1.1 Thermal Management Systems for Conventional Vehicles

In most conventional passenger vehicles with an internal combustion engine (ICE), the cabin cooling is achieved using a vapour-compression cycle in the air conditioning (AC) system, while the cabin heating is achieved by circulating engine coolant that carries engine waste heat to the cabin. Figure 1 presents a schematic drawing of an AC system of a conventional passenger vehicle.

The compressor is belt-driven by the crank shaft of the engine; hence, its speed is related to the engine speed and it consumes part of the output power from the engine. The details about the vapour compression cycle will be further discussed in Section 2.2.1.

The efficiency of an internal combustion engine is around 30% (Reif, 2004); consequently, 70% of the energy from the fuel is converted into heat and need to be removed from the engine. A coolant loop is used for the waste heat removal. A thermostat is used to keep the coolant at a certain temperature and direct the flow to the radiator once the temperature exceeds the designed level. In cold weather when cabin heating is needed, the coolant is

partially directed into a heat core inside the cabin, which transfers the heat from the coolant to cabin air.

As shown in Figure 1, in a passenger car, the radiator from the coolant loop and condenser from the vapour-compression cycle are located at the front of the car. The heat core from the coolant loop and evaporator from the vapour-compression cycle are located inside the cabin, with a blower that recirculates the cabin air.

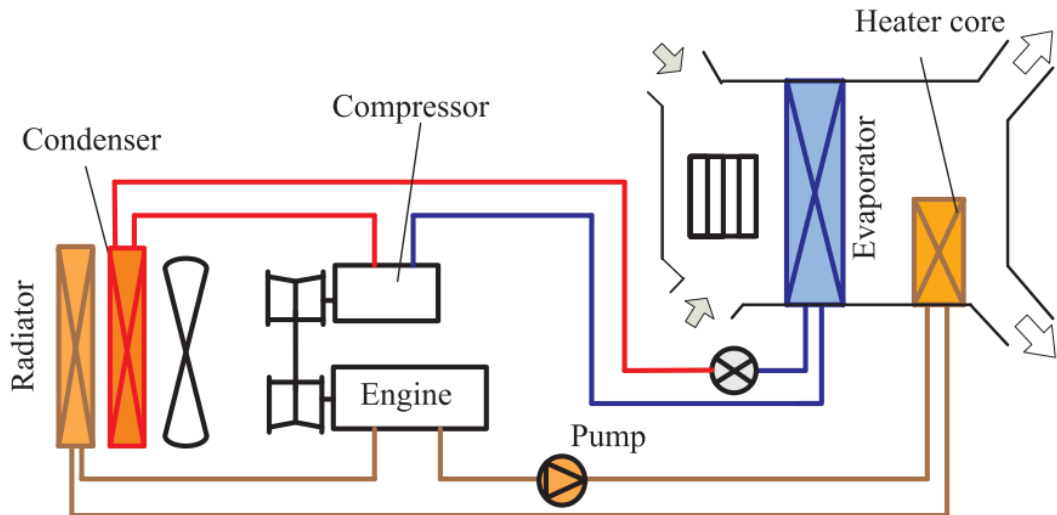


Figure 1. Schematic drawing of a typical AC system of a conventional passenger vehicle (Zhang *et al.*, 2018)

In modern city buses, the AC systems are similar to passenger vehicles, but with different layouts, and sometimes with various supplement.

The layout of the AC system (cooling) usually consists of two main units; 1) a roof-top unit which contains the condenser, the evaporator and the thermal expansion valve, as well as 2) a compressor which is located in the engine compartment with tubes that circles refrigerant with the roof-top unit. There is usually a front-box located near the driver, working as an evaporator for cooling the driver's cabin.

The heat cores (convector heaters) connected to the engine coolant loop are located at the lower left and right corners of the cabin. One typical example of an AC system on a city bus is shown in Figure 2.

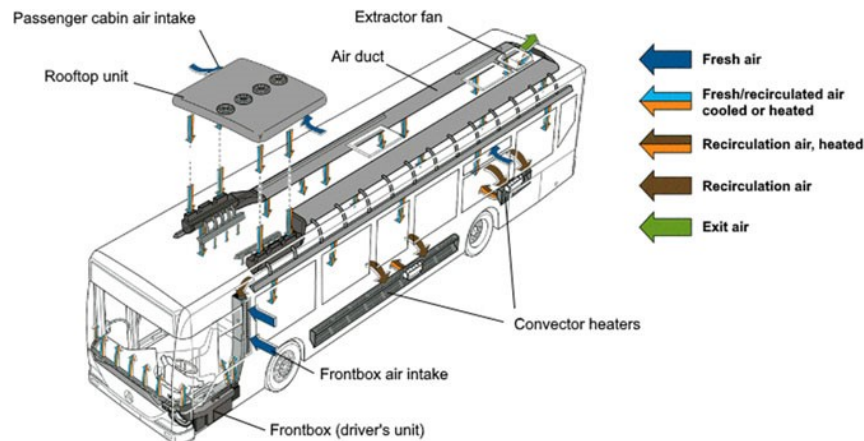


Figure 2. An AC system on a conventional city bus (Göhlich *et al.*, 2018)

It is usually insufficient using only engine waste heat to heat up the cabin in cold winter times. Therefore, various heating supplements are used on conventional city buses for cabin heating, such as electric heaters and fuel burning heaters. These heaters will be turned on for cabin heating when the engine of the bus is not sufficient, especially when the bus is not running, such as waiting in the terminals.

1.2 Thermal Management Systems for Electric Vehicles

Compare with internal combustion engines, the efficiency of electric motors are quite high, normally around 85-90% (Reif, 2004). Other parts of the powertrain such as main battery and inverters also generate waste heat. The waste heat generation during a real-life driving cycle for a battery electric bus simulation model is shown in Figure 3; the details of the simulation will be further discussed in the thesis. Compared with conventional vehicles, the powertrain of electric vehicles does not generate enough waste heat to heat up the cabin in cold weather.

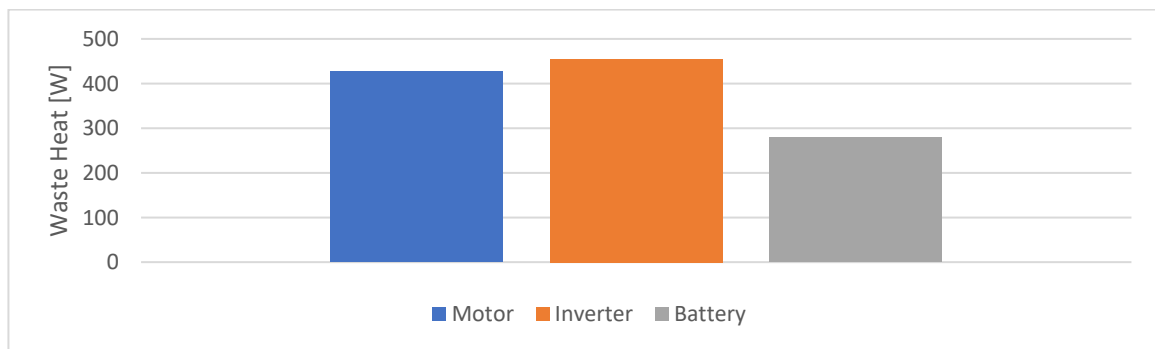


Figure 3. Simulation results of the average waste heat generation from powertrain components of a battery electric bus

Various solutions have been proposed for thermal management of electric vehicles (EVs) in general and cabin heating in particular. There are multiple ways to categorize the thermal management solutions. Zhang *et al.* (2018) grouped the solutions to electric vehicle air conditioning system into following categories:

- AC systems based on the vapour compression cycle, including dedicated heater, heat pump systems and other systems using low global warming potential (GWP) refrigerants and natural refrigerants.
- Non-vapour compression cycle, including thermal energy storage, applications of thermoelectric effects and magnetic effects, and waste heat driven systems.
- Integrated thermal management system combined AC and battery pack.

Similarly, Qi (2014) grouped air conditioning and heat pump system of electric vehicles into two categories:

- AC system based on the vapour compression cycle, including R134a, CO₂, and other working fluids systems.
- Non-vapour compression AC system, including applications of magneto-caloric and thermoelectric effects.

With the scope of the thesis, the following sections reviews previous studies related to heat pumps, thermal energy storage devices, and integrated thermal management.

1.2.1 Heat Pump

A heat pump (HP) is a feasible option for cabin heating in electric vehicles. Since the coefficient of performance (COP) of a heat pump could be greater than 1 in most conditions (Zhang *et al.*, 2018), it is more efficient to use heat pumps than resistive heaters. Lajunen *et al.* (2017) compared a heat pump system with a resistive heater in simulations using real-world driving cycles. The results showed that the benefits of using heat pump vary from 5% to 15%, with low speed cycles showing better results. The principles about heat pumps are discussed in detail in Section 2.2.

The heat pump of a bus unit resembles the look of an AC unit on a conventional bus; yet it has distinctive features. Figure 4 shows a comparison between a rooftop AC unit for conventional buses and a rooftop AC unit with heat pump mode for electric buses. The unit on the left is Eberspächer AC136 for conventional buses. The unit on the right is Eberspächer AC136 All-electric (AE) Heat pump (HP) for battery electric buses. The difference of the two systems are the following:

- AC136 features a vapour-compression loop for cooling; AC136 AE HP features two vapour compression loops for both cooling and heating. Therefore, a HP unit generally has more tubing and valves.
- The compressor of AC136 is located at the engine compartment, driven by the engine; The compressor of AC136 AE HP is located at the roof-top unit, driven by a battery-powered motor. Therefore, a HP unit always has a large hump at one end of the unit that houses the compressor.



Figure 4. Eberspächer AC136 for conventional buses (left) and AC136 AE HP for battery electric buses (right) (Eberspächer, 2019)

Because the compressor from a heat pump, as well as blowers and fans, are powered by the main battery, the driving range will be reduced when the heat pump is powered on. Figure 5 presents the simulation results that shows the energy consumption and driving range of a battery electric bus that uses a heat pump for cabin heating. The details of the simulation model will be later discussed in the thesis.

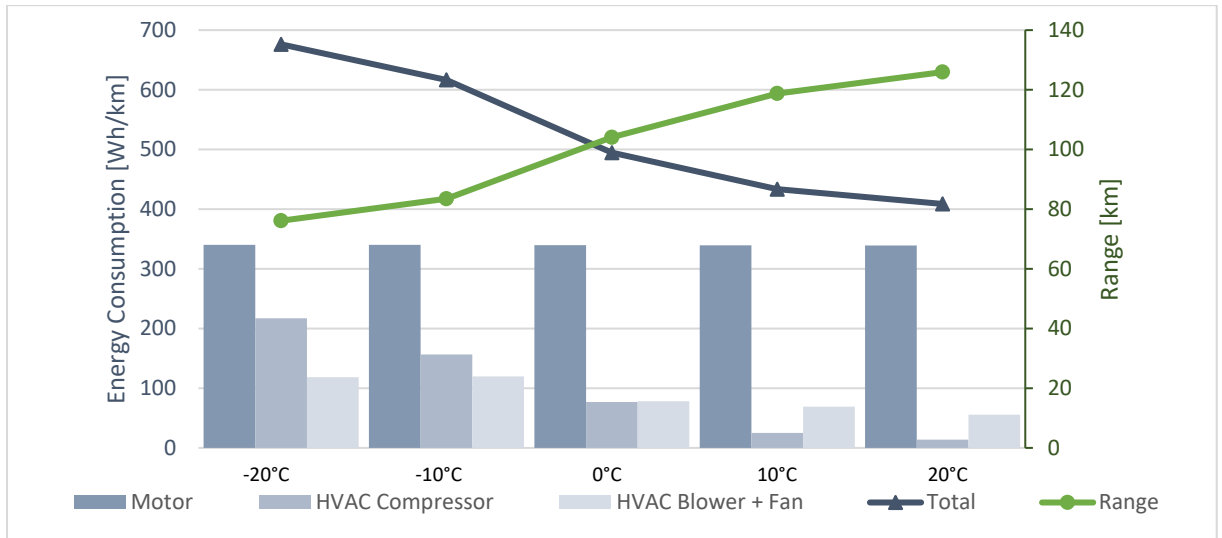


Figure 5. Energy consumption and driving range chart for a battery electric bus

As can be seen from this figure, in -20°C ambient temperature, the power consumption of heat pump (335.8 Wh/km for compressor, blower, and fans) reaches the level of the driving motor (340.4 Wh/km). Compared to the 126 km driving range in 20°C , the driving range is reduced to 76 km in -20°C . The significant range reduction (40%) could cause operation uncertainty for electrified bus lines since buses need to be charged more frequently; it will even exclude the electrification possibility of some existing bus lines.

1.2.2 Thermal Energy Storage

The idea of thermal energy storage is that the energy could be stored in the form of heat and released for cabin heating once needed. There are different substances where energy could be stored.

Some of the studies use more traditional substance, such as coolant or water, for thermal energy storage. Lajunen *et al.* (2017) proposed a thermal energy storage system that stores thermal energy in a coolant tank in a branch of the powertrain cooling loop. The branch could be activated once needed and the hot coolant would flow into the loop and transfer heat to a cabin heat exchanger.

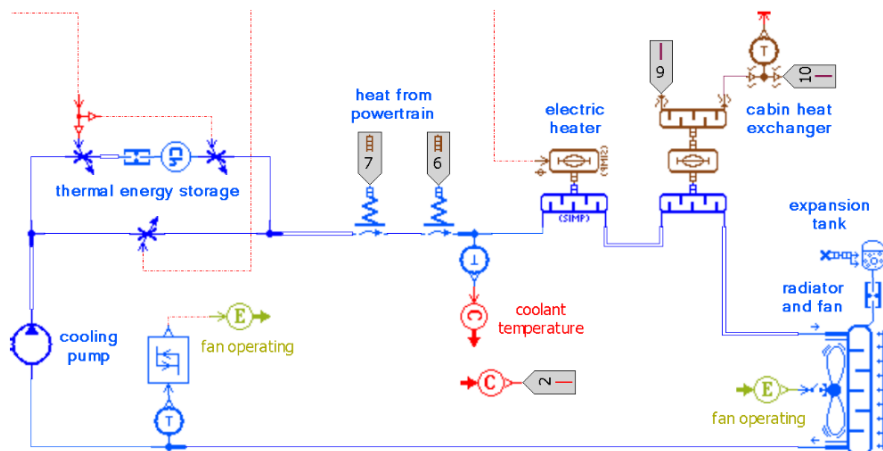


Figure 6. AMESim simulation model of a thermal energy storage system by Lajunen *et al.* (2017)

There is a trend of using phase change materials (PCM) as a substance for thermal energy storage. PCMs are a group of materials that uses latent heat while changing phase (typically melting and freezing) to absorb or release a relatively large amount of thermal energy at essentially constant temperature. Ianniciello, Biwolé and Achard (2018) used phase change material for the cooling of a Li-ion battery. Shahidinejad, Bibeau and Filizadeh (2012) evaluated a cabin heating system using phase change material in the physical model of an electric vehicle. The PCM could keep the cabin temperature at a constant 15°C and increase the driving range by 24%. Wang *et al.* (2016) built a novel climate control system that used PCM material for cabin heating. The liquid loop used in the heating system was coupled with a positive temperature coefficient (PTC) heater to address the situations when PCM is not able to heat up the coolant to the target temperature. Various PCM material were synthesized with different melting points and latent heat. The system was built and test on an EV and was able to extend the range of the EV from 68 km to 85.7 km in -10°C ambient temperature.

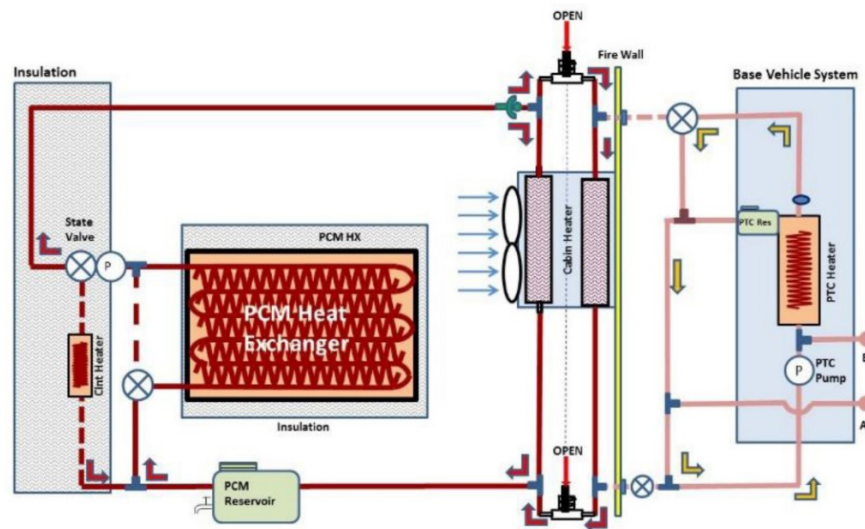


Figure 7. Cabin heating system using PCM material proposed by Wang *et al.* (2017)

1.2.3 Integrated Thermal Management

Integrated thermal management systems are the system level solutions that combine the thermal management of cabin, battery, powertrain components.

Lajunen *et al.*, (2017) added a cabin heat exchanger to the powertrain cooling loop. The waste heat from inverter and motor, together with a thermal energy storage tank, is transferred to the cabin through a coolant loop. Chowdhury *et al.* (2018) designed a system that integrated all the cooling/heating needs of an electric vehicle into two coolant loops – a cold coolant loop and a hot coolant loop. The two loops exchange energy using a vapour compression cycle (refrigerant loop). The hot coolant loop removes heat from the on-board charger (OBC), electric motor (EM) and powertrain (PE) as well as the condenser in the refrigerant loop if activated. When heating is needed, the cabin and battery are connected with the hot coolant loop. When cooling is needed, the cabin and battery are decoupled from the hot coolant loop and connected with the cold coolant loop. The chiller and refrigerant loop are activated and all the waste heat is rejected from the front-end heat exchanger (FEX, radiator). The system was built to an electric passenger car and tested in real-world

conditions. The results showed a 15-18% range improvement over the original thermal management system.

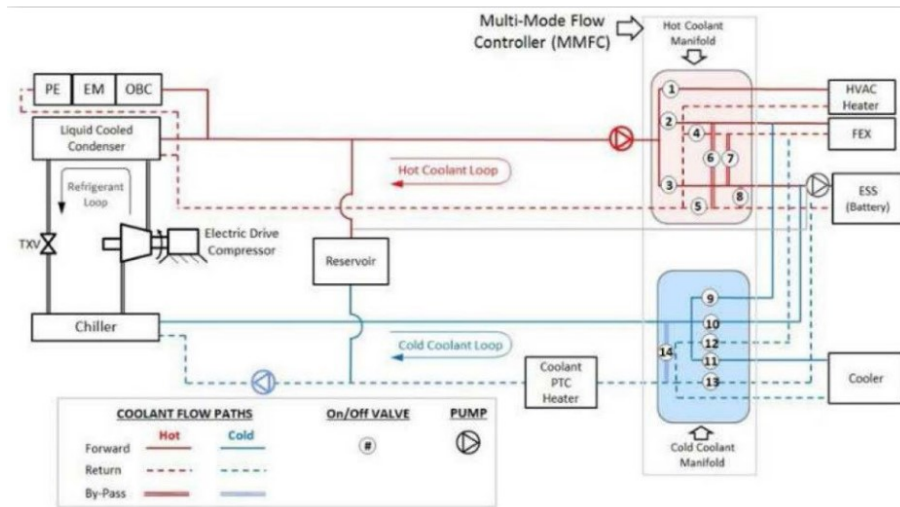


Figure 8. Integrated thermal management system for an electric vehicle proposed by Chowdhury et al. (2018)

1.2.4 Other Approaches

Positive temperature coefficient or PTC heaters used PTC element whose resistance will increase rapidly at a certain temperature. Jeong and Lee (2015) verified the possibility of using high voltage PTC heaters for cabin heating in electric vehicles. The parameters of the PTC heater are tested and optimized for better efficiency. A minimum efficiency of 93% could be achieved. Kim, Kim and Kim (2012) proposed a cabin heat solution that combined the heat pump with PTC heater. The PTC heater is placed behind the condenser (internal heat exchanger) to heat up the cabin air. At 20°C indoor temperature, the heating capacity is increased by 59% compared with a single PTC heater.

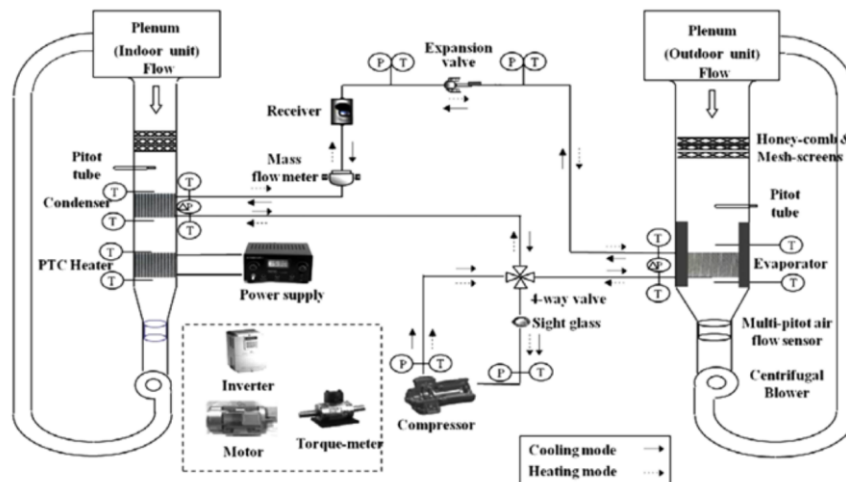


Figure 9. A combination of heat pump and PTC heater proposed by Kim, Kim and Kim (2012)

The fuel burning air heater is another solution to improve operation stability in cold conditions (Qi, 2014). Figure 10 shows a product from Webasto. These heaters are traditionally used for the rear compartment heating of recreational vehicles (RV). With the growing popularity of electric buses, these heaters are also suitable for cabin heating in hybrid buses (Webasto, 2017) and other electric buses. Fuel burning air heaters consume

fuels, such as diesel, biodiesel and gasoline. Just like internal combustion engine, burning fuels will cause emission that reduce the environmental benefits of electric buses.



Figure 10. Webasto Air Top Evo air heater (Webasto, 2019)

1.3 Vehicle Cabin Simulation

There is an immense amount of work done in electric vehicle simulation, focusing on different perspectives. Among all the systems, cabin is the most important part in thermal management simulation for bus. An accurate simulation of the cabin is the basics for evaluating different thermal management solutions. Depends on the level of detail considered during modelling, the cabin simulation could be divided into several categories.

1.3.1 Mono-zonal Model

The mono-zonal model is the simplest in terms of cabin thermal mass modelling, since the cabin air is considered a whole with homogeneous properties. The advantage of using mono-zonal model is that it is easy to define the thermal and air exchange between the cabin air and environment. This type of cabin model is often used in studying thermal management solutions in system level simulations of vehicles. The disadvantages are that the cabin air is considered with uniformed property; spatial distribution of cabin air properties is not considered.

Shahidinejad, Bibeau and Filizadeh (2012) formed a cabin model that considered the thermal mass of the cabin air and the cabin shell as a whole. Marcos *et al.* (2014) used Simulink to simulate a cabin of a passenger vehicle. Only the indoor and lower base have thermal mass (thermal inertia). The heat flow from the windows, ceiling, base, and human are considered. Lajunen *et al.* (2017) used AMESim to simulate a cabin of a passenger vehicle. The thermal mass of the cabin air, windshield, side windows, rear windows, side panels, roof, and interiors are taken into consideration. The model is then used to test several cabin thermal management solutions.

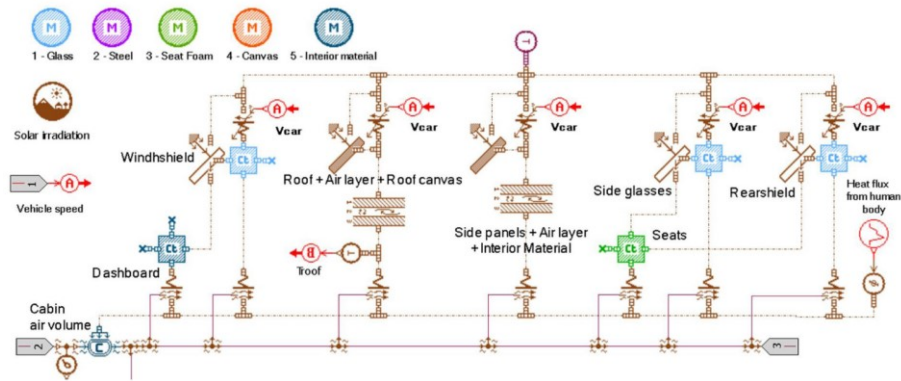


Figure 11. AMESim simulation model of a mono-zonal cabin model by Lajunen et al. (2017)

1.3.2 Computational Fluid Dynamics (CFD) Model

Computational fluid dynamics (CFD) models could provide a much more detailed insight of air properties distribution inside the cabin.

It is popular to use CFD models to investigate cabin climate details for cabin and heating, ventilation and air conditioning (HVAC) system planning. For this purpose, the cabin air is usually the interested domain. Hence, the thermal energy exchange and air exchange between the cabin and the environment is usually omitted or simplified. Zhu, Demokritou and Spengler (2010) built a CFD cabin model of a shuttle bus to investigate the ventilation efficiency, spatial distribution of air velocity and air temperature, passenger thermal comfort, as well as air quality conditions. The model did not consider the air exchange with the external environment. The surface temperature of windows, walls, floor and lights were fixed based on measurement. Solar radiation is not considered. Leong *et al.* (2011) built a computer-aided design (CAD) cabin model for a passenger car to investigate the effectiveness of a ventilation device. Only cabin air is modelled with surround surfaces defined as boundary layer with various temperatures.

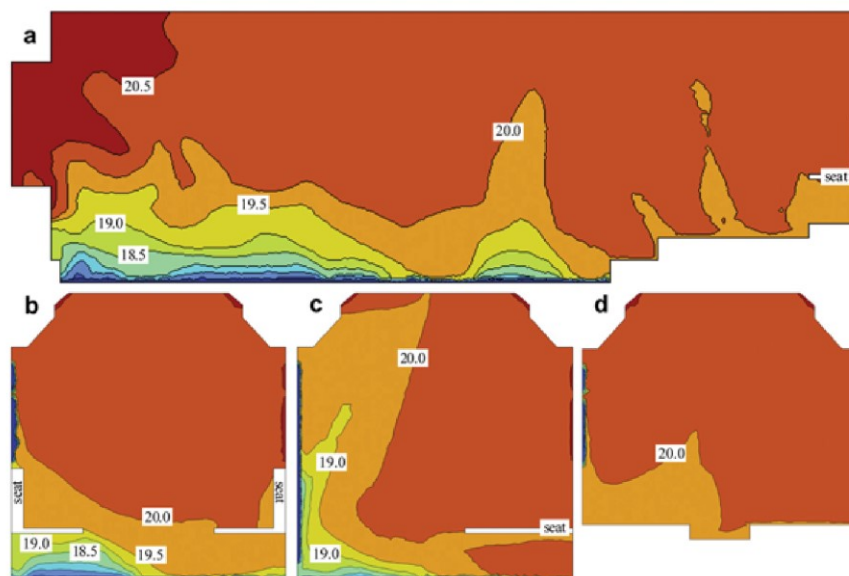


Figure 12. CFD simulation results of the spatial distribution of air temperature inside a bus cabin by Zhu, Demokritou and Spengler (2010)

Some other researches considered the interfaces between the cabin and the environment. Nassajfar (2018) built 1D and 3D CFD cabin simulation models of a passenger vehicle. In the 3D simulation, a build-in tool of solar radiation in StarCCM+ is used, which provide the solar flux, azimuth and altitude of the sun from given location and time. The windows are modelled as glass with transmissivity coefficient, and the solar radiation through the window as well as glass inner surface temperature is calculated. Wirth, Eimler and Niebling (2014) built a cabin CFD model with cabin insulation modelled. The thermal energy exchanges among the cabin air, cabin insulation and the environment are simulated.

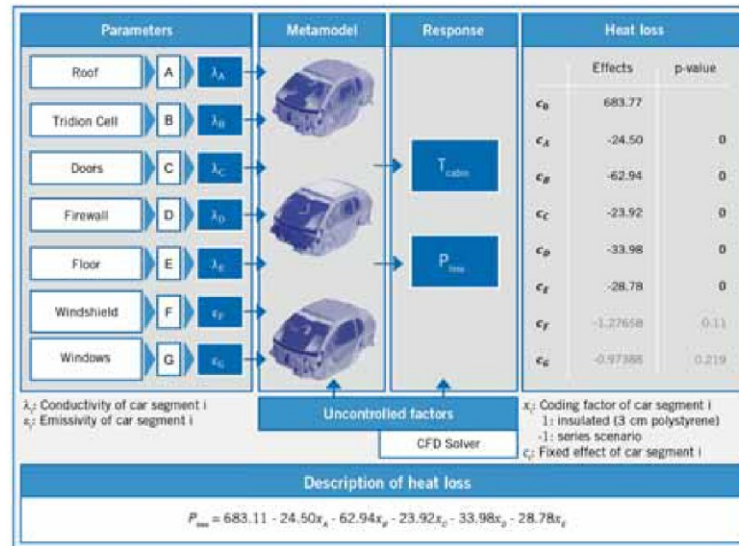


Figure 13. CFD cabin model by Wirth, Eimler and Niebling (2014)

1.3.3 Other Approaches

Lumped-parameter model is a multi-zonal approach where the cabin is divided into several discrete lumps with uniform. It could be considered as a simplified CFD model (Brèque and Nemer, 2017), or an advanced mono-zonal model. It is worth noting that there is some ambiguity in using the term ‘lump’ to describe cabin models. Li and Sun (2013) built a model of a train car that considered the thermal masses of the cabin air, roof, floor and walls, while calling the model ‘lumped’. Since the cabin air is considered a unified thermal mass, the model should be called mono-zonal by the standard discussed in the thesis.

Torregrosa-Jaime *et al.* (2015) presented a lumped-parameter cabin model of a mini-bus, in which the cabin air is divided into two thermal zones: the driver’s zone and the passengers’ zone. There is air circulation between zones, which will result in change of air properties.

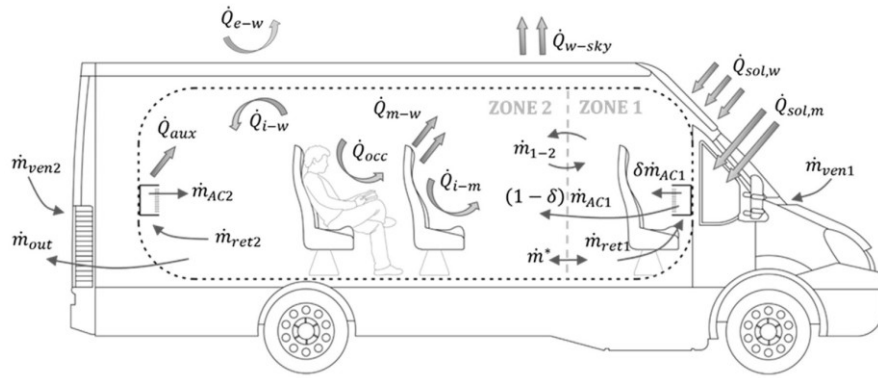


Figure 14. Lumped-parameter cabin model proposed by Torregrosa-Jaime et al., (2015)

Siemens AMESim has a built-in embedded CFD tool that could combine the system-level (mono zonal) simulation with CFD simulation. A simple cabin geometry could be defined, and the air properties, heat transfer coefficient, and mass flow rates at interfaces could be translated between 1D (system-level) and 3D (CFD) automatically. The tool is suitable for car cabin thermal management analysis at early design stage (Siemens, 2019).

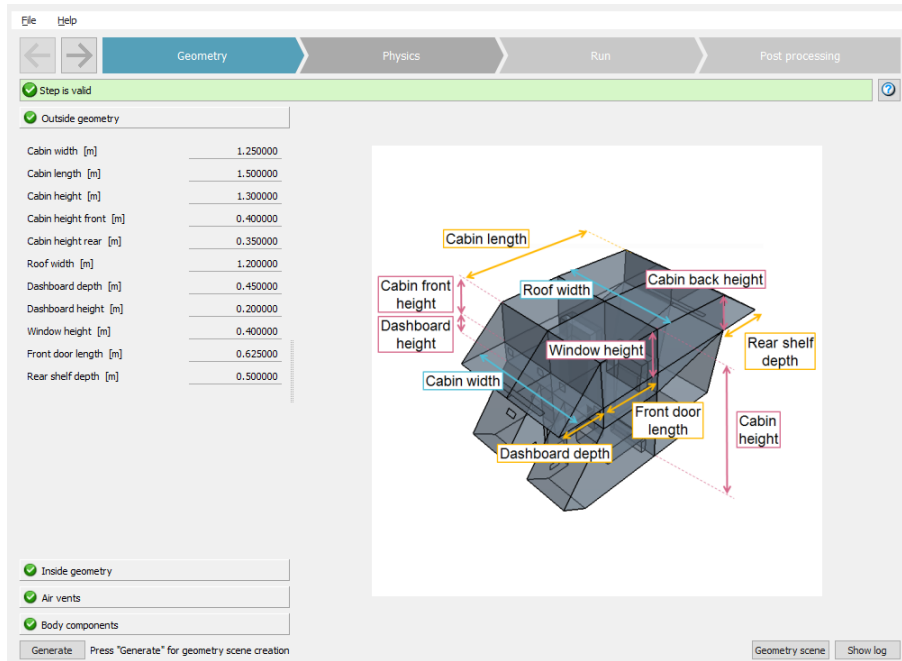


Figure 15. User interface for the Embedded CFD (ECFD) tool in AMESim (Siemens, 2019)

1.4 Tools for EV Thermal Simulations

For many electric vehicle simulation tools, HVAC and cabin thermal simulation is not present or only present as a part of auxiliary consumption calculation (Mahmud and Town, 2016). The tools discussed in this section are specifically for system-level electric vehicle thermal simulations. A list of related literature is presented in Table. Different tools have been used to fulfil different research scopes.

Table 1. Tools being used in system-level electric vehicle thermal simulations

Tools	Title (Authors)	Scope
	On auxiliary systems in commercial vehicles	Auxiliary (Hydraulic)

Matlab-Simulink	(Andersson, 2004)	
	Design and Simulation of a Thermal Management System for Plug-In Electric Vehicles in Cold Climates (Shahidinejad, Bibeau and Filizadeh, 2012)	Cabin
	Electric city bus and infrastructure demonstration environment in Espoo, Finland (Laurikko <i>et al.</i> , 2015)	Cabin
	Transient thermal model of a vehicle's cabin validated under variable ambient conditions (Torregrosa-Jaime <i>et al.</i> , 2015)	Cabin
	Modeling of an Electric Vehicle Thermal Management System in MATLAB/Simulink (Kiss, Lustbader and Leighton, 2015)	Cabin and powertrain coolant loop
	Total Thermal Management of Battery Electric Vehicles (BEVs) (Chowdhury <i>et al.</i> , 2018)	Cabin and powertrain coolant loop
	Battery Thermal Management Systems of Electric Vehicles (Ianniciello, Biwolé and Achard, 2018)	Battery and battery thermal management
Siemens AMESim	Investigation of thermal energy losses in the powertrain of an electric city bus (Lajunen and Kalttonen, 2015)	Electric vehicle (Powertrain)
	Thermal management model for a Plug-In Hybrid Electric Vehicle (Mater <i>et al.</i> , 2016)	Hydraulic, powertrain coolant loop, HVAC
	Thermal energy storage for increasing heating performance and efficiency in electric vehicles (Lajunen <i>et al.</i> , 2017)	Powertrain coolant loop
	Energy Efficiency and Performance of Cabin Thermal Management in Electric Vehicles (Lajunen <i>et al.</i> , 2017)	Cabin, HVAC, Electric vehicle
StarCCM+	Thermal Insulation of Electric Vehicle Cabins (Wirth, Eimler and Niebling, 2014)	Cabin (CFD)
Self-programming	The development and validation of a thermal model for the cabin of a vehicle (Marcos <i>et al.</i> , 2014)	Cabin
	Enhanced Battery Thermal Management Systems with Optimal Charge Control for Electric Vehicles (Rashid, Hofman and Rosca, 2018)	Battery and battery thermal management

As can be seen from the table that Matlab/Simulink and Siemens AMESim are popular tools in system level vehicle thermal simulation. Although Matlab/Simulink offers more freedom in an open-source point of view, the listed researches using the tool generally have narrower scope than using Siemens AMESim, mostly focusing on one or two sub-system of EVs only. Siemens AMESim offers libraries that fulfil the needs for electric vehicle powertrain simulation as well as thermal simulation, offering opportunity for a full-system EV

simulation. The interface between AMESim and StarCCM+ offers possibility to combine system-level simulation with cabin CFD simulation.

1.5 Research Aims, Methods, and Scope

1.5.1 Research Aims

Although there are much works focusing on simulation of electric vehicles, few studies have been devoted to the simulation of electric city buses. The first aim of the thesis is to build a system-level simulation model of a battery electric city bus based on the electric bus prototype of VTT, e-Muuli. The parameters in the model should generally follow the parameters of e-Muuli. Various experiments are used to validate the simulation model. The final simulation model should have the functionality of simulating the operation of electric buses on driving cycles in different ambient conditions.

Despite a number of studies investigating thermal management solutions for electric vehicles, less work has focused on combining the solutions with a system-level simulation of a battery electric city bus. Additionally, current solutions being used on battery electric city buses, such as heat pumps and fuel burning air heaters, all have their limitations and thus could not be considered optimal solutions. Therefore, a second aim of the thesis is to evaluate several innovative thermal management solutions with the objectives of improving the cabin heating performance and driving range in cold conditions. The solutions are built on the basis of the electric city bus simulation model and verified using real-life driving cycles in different ambient temperatures.

1.5.2 Simulation Tools and Methods

As a simulation tool, Siemens AMESim has the advantage in performing system-level simulation for whole systems in electric vehicles, featuring a more user-friendly modelling logic compared with Simulink. As a result, AMESim is selected as the simulation tool for the thesis.

AMESim also provides the possibilities for multi-level simulation; different systems of a battery electric bus could be simulated in different levels of details. Since the focus of the thesis is to investigate the thermal management solutions, the thermal-related systems in a battery electric vehicle are simulated with higher levels of details, such as electric machine (motor), battery and thermal systems (HVAC, heat exchangers and cabin). Other systems of a vehicle are simulated on a relatively low level of details, such as gearbox (transmission) and chassis. The approach is presented in Figure 16. The systems that are not related to the scope of the thesis, such as suspension system, are not considered in the thesis.

Thermal mgmt	Electric machine	Battery	Thermal systems	Gearbox	Chassis	Suspension	Range and Perfo
Level 1	Static	Generic battery	Map based	Ratios efficiency	One inertia	2D linear	Drivability
Level 2	Quasi-static	Advanced model (semi-empiric)	Dynamic models cooling loops HVAC	Flywheel inertia	3 DoF (2D)	3D multi-body	NVH
Level 3	Dynamic	Advanced model (semi-empiric) + thermal	Heat exchangers stacking	Detailed rotary stiffness and inertia	18 DoF (3D)		Emissions
Level 4	Cooperation with FEM	Advanced model (semi-empiric) + aging	Cosimulation with CFD				

Unrestricted © Siemens AG 2018

Figure 16. Multi-level simulation for electric vehicle (Siemens, 2018)

One example of multi-level simulation is that the cabin model could be simulated in AMESim in different levels of details, as shown in Figure 17. The first level is a pre-defined mono-zonal model that only considers the basic inputs and outputs of the cabin. The second level is also a mono-zonal model that considers the thermal mass of not only the cabin air but also the interfaces to the environment. The third level is a lumped-parameter model with CFD co-simulation.



Figure 17. Different levels of details for cabin modelling in AMESim

1.5.3 Research Scope

The object of the thesis is limited to the thermal management in battery electric city buses. Other types of buses, such as conventional buses, hybrid electric and fuel cell electric buses, have significant difference in vehicle design; hence, they are excluded from the scope of the thesis. Battery electric passenger cars have different powertrain layout as well as different demand in cabin heating; hence, they are also excluded from the scope of the thesis either. On the other hand, the simulation model addresses the unique characters of battery electric buses, such as frequently opened doors disrupting the cabin thermal balance which is not

necessary for passenger car simulation, and a powerful heat pump that are not needed for conventional and hybrid electric buses.

The detail of the simulation should be a balance between accuracy and feasibility. In ideal scenarios, the simulation model should be as detailed as possible. However, the models' levels of detail are limited by many factors, such as limitations in working time, limitations in computing power, and limitation in knowledge level on the topic. For example, as discussed in Section 1.5.2, AMESim provide three levels for cabin modelling. In the initial plan of the thesis, a level-three cabin model (using the embedded CFD tool) was set as the target of the thesis. However, the target was later readjusted to level two (detailed mono-zonal model) due to the limited amount of time.

1.6 Thesis Structure Overview

The rest of the thesis is organized as follows. Chapter 2 discusses some background knowledge needed for understanding the thesis. Chapter 3 describes the development of the electric bus simulation model based on e-Muuli. Chapter 4 presents the simulation results to show the characteristics of the model, as well as measurement data from the experiments to validate the simulation model. Chapter 5 describes the development of several innovative thermal management solutions based on previous electric bus model; the chapter also presents detailed simulation results of various thermal configurations used in real-world driving cycle under different ambient conditions. Chapter 6 discusses the problems faced during the thesis work and the next step for the development of the simulation model.

2 Background Knowledge

2.1 Thermodynamics Basics

2.1.1 Heat Transfer

Heat can be transferred in three ways: conduction, convection, and radiation (Cengel and Boles, 2004). All three modes of heat transfer happen from a higher-temperature medium to a lower-temperature one.

Conduction happens in all kind of materials, i.e., solids, liquids, and gases. It is a process of transferring energy between particles within a substance. In liquids and gases, the particles transfer energy by colliding with each other during random motion. In solids, the energy is transferred by a combination of vibration of molecules and energy transport by free electrons.

The conduction energy is regulated by Fourier's law of heat conduction (Cengel and Boles, 2004):

$$\dot{Q}_{cond} = -k_t \cdot A \cdot \frac{dT}{dx} \quad (1)$$

where k_t is thermal conductivity of the material, A is the area that is normal to the direction of heat transfer, dT is the temperature difference, dx is the thickness of the layer. k_t measures the ability of a material to conduct heat. Materials such as copper and silver, are good electric conductors as well as heat conductors, and hence have a high k_t level. Materials such as rubber and wood are poor conductors of heat, and hence have low k_t values. Fourier's law indicates that the rate of the heat conduction in a direction is proportional to the temperature gradient in that direction. Heat is conducted in the direction of decreasing temperature.

Convection is the type of heat transfer between a surface and the adjacent fluids. The speed of convective heat transfer is related to the movement of the fluid; the higher the speed of fluid, the greater the convective heat transfer. If there is no movement of the fluid, the heat will only transfer in the form of conduction.

The movement of the fluid could be caused by either external forces such as fans and pumps, or natural causes such as density differences; the convection is called forced convection and natural convection respectively.

The convective energy is regulated by Newton's law of cooling (Cengel and Boles, 2004):

$$\dot{Q}_{conv} = hA(T_s - T_f) \quad (2)$$

where h is the convection heat transfer coefficient, A is the surface area through which the heat transfer takes place, T_s is the surface temperature, and T_f is the bulk fluid temperature away from the surface.

The convection heat transfer coefficient is an experimental determined parameter that is affected by many factors, such as surface geometry, the properties of fluid, and the velocity of the fluid. Table 2 lists some typical values of the coefficient. (Cengel and Boles, 2004)

Table 2 Typical values for convection heat transfer coefficient

Fluid type adjacent to solid	h value in different types of convection (in $W/m^2 \cdot K$)	
	Natural convection	Forced convection
Gas	2-25	25-250
Liquid	50-1000	50-20000
Gas liquid mixture during boiling and condensation	2500-100000	

Radiation is the type of energy transfer by electromagnetic waves or photons. Radiation does not need intervening medium to happen, which is the way sun transfer energy to earth through the space.

The maximum rate of radiation that can be emitted from a surface at an absolute temperature T_s is given by the Stefan–Boltzmann law as (Schenubel, 2017)

$$\dot{Q}_{emit,max} = \varepsilon\sigma AT_s^4 \quad (3)$$

Where ε ($0 \leq \varepsilon \leq 1$) is the emissivity of the surface, $\sigma = 5.67 \cdot 10^{-8} W/m^2 \cdot K^4$ is the Stefan–Boltzmann constant, A is the surface area, and T_s is the surface temperature.

In the thesis, conduction and convection are the major concerns. When using liquid to the air heat exchanger, two steps heat transfer happens: from liquid to metal, and from metal to air. Both could be considered a combination of conduction and convection, the proportion of which is regulated by Nusselt number:

$$Nu = \frac{\dot{Q}_{conv}}{\dot{Q}_{cond}} \quad (4)$$

2.1.2 Phases of a Substance and Pressure-Enthalpy (PH) Diagram

Substances exist in different phases: solid, liquid, and gas. The phases could be interpreted from the strength of the intermolecular bonds. The molecules in a solid are arranged in a

three-dimensional pattern (lattice) that is repeated throughout. The molecules in a solid cannot move relative to each other, they continually oscillate about their equilibrium positions. The molecular spacing in the liquid phase is not much different from that of the solid phase, except the molecules are no longer at fixed positions relative to each other and they can rotate and translate freely. In the gas phase, the molecules are far apart from each other, and a molecular order is non-existent. The energy level of a substance in the liquid phase is higher than in the solid phase. Gas molecules move about at random, continually colliding with each other and the walls of the container they are in. The energy level of a substance in the gas phase is the highest among the three.

At a given pressure, the temperature at which a pure substance changes phase is called the saturation temperature T_{sat} . Likewise, at a given temperature, the pressure at which a pure substance changes phase is called the saturation pressure P_{sat} . The amount of energy absorbed or released during a phase-change process is called the latent energy. During phase changing, the temperature of many substances will stay at T_{sat} , and thus the change of energy will be latent to temperature sensors. On the contrary, the amount of energy absorbed or released during one phase is called sensible energy, because the energy change will be represented by change of temperature. In daily life, we frequently refer to both latent and sensible energy as heat. In the thesis, those forms of energy are referred to as heat or thermal energy.

The heat added to a saturated mix of liquid and gas will result in more liquid in the mix changing into gas until the mix become saturated gas, while the temperature remains the same. If more heat is added to the saturated gas, the gas temperature will rise above its saturation (boiling) point; the gas in this state is called superheated gas (vapour). On the contrary, the heat removed from a saturated mix of liquid and gas will result in more gas in the mix changing into liquid until the mix become saturated liquid, while the temperature remains the same. If more heat is removed from the saturated liquid, the liquid temperature will drop below its saturation (boiling) point; the liquid in this state is called Subcooled liquid (Stanfield and Skaves, 2017). Generally speaking, latent heat is more suitable for energy storage than sensible heat. For example, the vaporization latent heat of water is 2265.5 kJ/kg (Cengel and Boles, 2004) while the specific (sensible) heat for liquid water and water vapour are $4.2 \text{ kJ/(kg} \cdot \text{K)}$ and $2.0 \text{ kJ/(kg} \cdot \text{K)}$ (Dartmouth College, 2019) respectively.

There are several property diagrams that could be used for phase-change processes. T-v diagram demonstrates the change of phase in a diagram with temperature T versus the specific volume v. P-v is similar, but only change the y-axis to pressure P. For researches related to HVAC or generally about refrigerant cycle, PH (Pressure-enthalpy) diagram is used.

Enthalpy is the amount of heat in a substance, represented by the uppercase letter H . Specific enthalpy is the amount of heat per kilogram (kJ/kg in SI units), represented by lower case letter h . PH diagrams show the relationships between pressure, heat, temperature, volume, and state of a refrigerant. One example of PH diagram of refrigerant R134a is shown in Figure 18.

In the diagram, y-axis is indication pressure while x-axis is indicating specific enthalpy. The reverse u-shape curve is called saturation curve, which shows where the substance will change phase; the left side to the curve is subcooled liquid; right side to the curve is superheated gas; in the middle of two sides are mixture of liquid and gas. The critical point

is located at the very top of the curve. The critical point is the pressure and temperature at which liquid and vapour are indistinguishable; refrigerant cannot be saturated above the critical point (Stanfield and Skaves, 2017).

There is more information included in the PH diagram. Inside the saturation curve, there are constant-quality lines that start at the bottom and extend upward toward the critical point. They represent the percentage of vapour in the saturated refrigerant. The constant temperature lines start along the left top of the diagram and drop nearly vertically to a point where they intersect the saturated liquid line. At this point, they travel horizontally across to the saturated vapour line, where they drop nearly vertically again. The constant entropy lines start at the bottom of the PH diagram and slope upward to the right. The constant volume lines are nearly horizontal lines start at the saturated vapour line and gradually slope up to the right. The lines represent the change in density of the refrigerant at a constant pressure due to the increase in enthalpy and temperature.

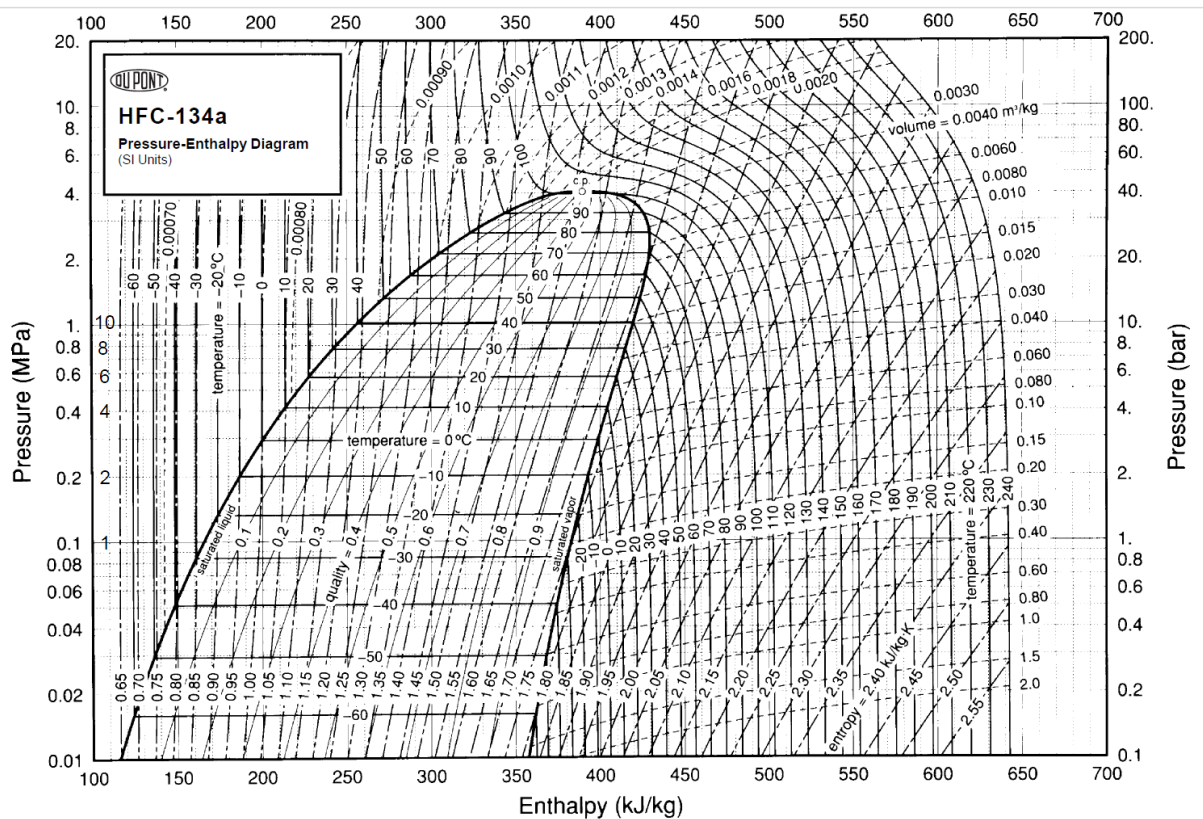


Figure 18. Pressure-Enthalpy (PH) diagram of R134a (Du Pont, 2015)

Phase changing is an important topic in the thesis because latent heat is more suitable to be utilized in energy storage than sensible heat. In the vapour-compression cycle used in the vehicle HVAC system, the refrigerant changes back and forth between liquid and gas, while carrying thermal energy with it. For phase change material, the latent heat between the liquid and solid phase is used to store thermal energy to heat up the cabin. PH diagram will be used to demonstrate the performance of the HVAC system.

2.2 HVAC Basics

Heating, ventilation and air conditioning (HVAC) is the system that is designed to provide thermal comfort inside the house or vehicular cabin. In the vehicle, HVAC is considered a part of auxiliary systems together with the air compressor, power steering, lighting, etc (Reif,

2004). HVAC is the most energy consuming auxiliary in a battery electric vehicle (Göhlich *et al.*, 2018b).

It is worth noting that sometimes academia uses the terms ‘air conditioning’ and ‘heat pump’ differently than in daily life. In daily usage, the term ‘air conditioning (conditioner)’ is often used to describe the HVAC system that only has cooling mode while ‘heat pump’ is used to describe HVAC system that is designed for heating (Carrier, 2019). On the other hand, many research papers use the term ‘air conditioning’ is used to cover the whole meaning of HVAC. Schenubel (2017) define air conditioning as a process by which air is: cooled, heated, cleaned or filtered, humidified or dehumidified, circulated or recirculated. Zhang *et al.*, (2018) define air conditioning (AC) as a system that provides cool, heating and ventilation in the vehicle cabin. In this thesis, the term ‘HVAC’ is used to describe the system, while simple ‘heating’ and ‘cooling’ are used to describe different modes.

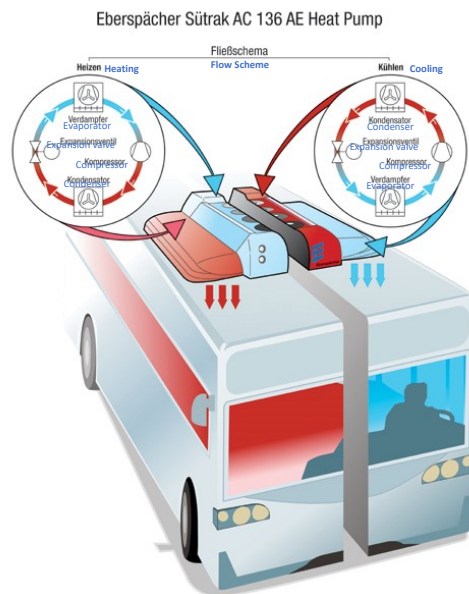


Figure 19. Eberspächer AC136 AE HP HVAC flow scheme (Eberspächer, 2019)

2.2.1 Compressor, Condenser, Evaporator and Vapour Compression Cycle

The term ‘refrigeration’ is used to describe the thermodynamics procedure where heat is transferred from a lower temperature region to a higher temperature region. Both heating and cooling mode of the HVAC system is considered as refrigeration. The cycle on which the refrigeration is operated is called refrigeration cycle. Vapour-compression cycle is the most frequently used refrigeration cycle, in which the refrigerant is vaporized and condensed alternately and the compression happens in the vapour phase (Cengel and Boles, 2004).

The efficiency of a vapour compression cycle is evaluated by the coefficient of performance (COP), which is defined by the following equations (Cengel and Boles, 2004).

$$COP_{cool} = \frac{\text{Desired output}}{\text{Required input}} = \frac{\text{Cooling effect}}{\text{Work input}} = \frac{Q_L}{W_{net,in}} \quad (5)$$

$$COP_{heat} = \frac{\text{Desired output}}{\text{Required input}} = \frac{\text{Heating effect}}{\text{Work input}} = \frac{Q_H}{W_{net,in}} \quad (6)$$

Q_L is the magnitude of the heat absorbed by the evaporator; Q_H is the magnitude of the heat released by the condenser; $W_{net,in}$ is the net work input to the cycle. Both COP_{cool} and COP_{heat} could be greater than 1.

One common way to visualize the vapour-compression cycle is through PH-diagram, shown in Figure 18 and Figure 20. With the example of HVAC cooling mode with R134a refrigerant, the PH diagram is explained. The transfer of heat in an HVAC system is accomplished by two pressure and two temperature systems in one cycle: a low-pressure side with low temperature (from 4 to 1 in Figure 20) and a high-pressure side with high temperature (from 2 to 3 in Figure 20). For an R134a cooling HVAC system, the pressure and temperature of the low-pressure side are normally ranged at 145-241 kPa and -4°C to 4°C , and the high-pressure side is at 1241-1517 kPa and 51°C to 58°C (Schenubel, 2017). The low-pressure side is sometimes referred to as suction side, while the high-pressure side is referred to as discharge side.

During the pressure-temperature change, there is also a change of state. On the low-pressure side, the refrigerant changes from liquid to vapour inside evaporator; on the high-pressure side, the refrigerant changes from vapour to liquid in the condenser. If all the liquid refrigerant in the evaporator core has gone through a change of state from liquid to gas before reaching the end of the evaporator, the gas will continue to pick up heat from the evaporator and becomes superheated gas (from 1s to 1 in Figure 20). Similarly, 3s to 3 shown in Figure 20 is subcooled liquid. Both lines are horizontal to the pressure lines because the pressure remains the same throughout the condensing and evaporating processes.

The pressure of the refrigerant is increased by the compressor. The compressor pumps low-pressure refrigerant vapour from the evaporator to the condenser at the high pressure (from 1 to 2 in Figure 20). In the figure, the compressor line follows the entropy lines up. The pressure of the refrigerant is decreased by the metering device which is a thermal expansion valve (TXV) in this case (from 3 to 4 in Figure 20). The line drops vertically because no heat is gained or lost in the metering device, but the pressure drops dramatically.

For cooling mode, the evaporator is located inside the cabin while the condenser is located outside the cabin. For HVAC systems with heat pump mode, the positioning of the evaporator and condenser is reversed, shown in Figure 19 and Figure 62. Because the HVAC systems that are going to be investigated in the thesis are HVAC with heat pump, the terms internal heat exchanger (IHX) and external heat exchanger (EHX) are used for avoiding ambiguity.

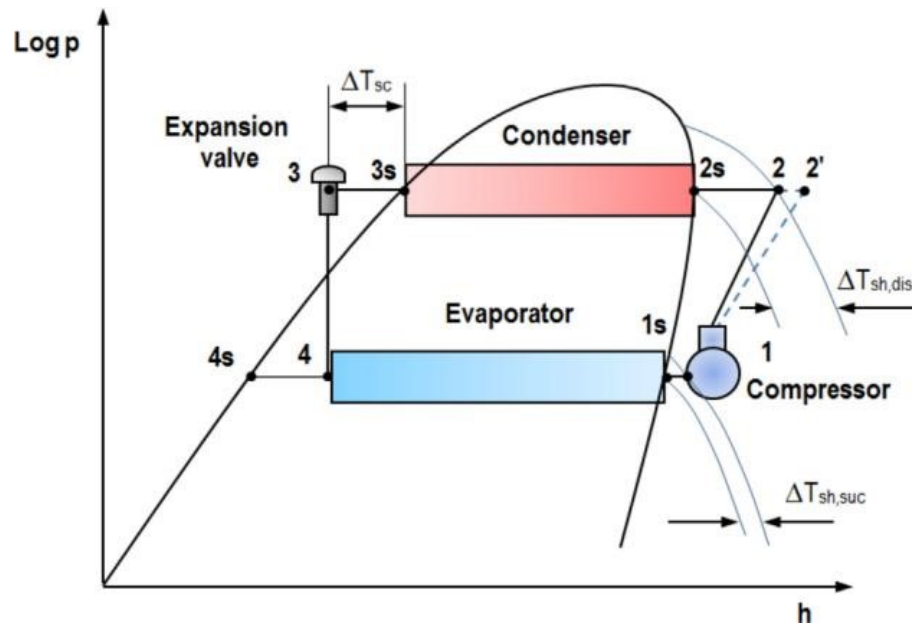


Figure 20. Vapour-compression cycle schematic diagram (Raghunatha Reddy, Bhramara and Govindarajulu, 2015)

2.2.2 Receiver-Drier

Receiver-drier is a bottle-like device located at the end of the high-pressure (discharge) side, between the condenser and the metering device. The receiver-drier performs three functions in the HVAC system (Schenubel, 2017):

- The receiver stores liquid refrigerant reserve to ensure a constant liquid supply to the metering device.
- The drier section collects small droplets of moisture that may have entered the system at the time of installation or repair.

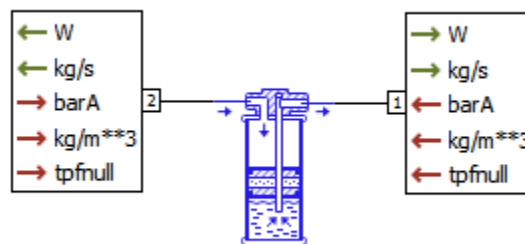


Figure 21. Schematic drawing for the receiver-drier model in AMESim (Siemens, 2019)

2.2.3 Accumulator

The accumulator locates at the end of the low-pressure (suction) side, between the evaporator and the compressor. The accumulator has a similar external appearance to the receiver-drier, but their function is different.

The purpose of the accumulator is to trap excess liquid refrigerant, prevent it from entering the compressor. Liquid refrigerant in the compressor could cause serious damage. The accumulator is a storage container for refrigerant vapour and any small amount of liquid refrigerant that did not reach the vapour point as it passed through the evaporator as well as lubrication oil that may be atomized and traveling with the refrigerant.

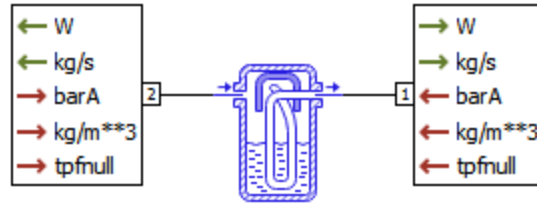


Figure 22. Schematic drawing for the accumulator model in AMESim (Siemens, 2019)

2.2.4 Metering Device – Thermal Expansion Valve

At the present time, there are two types of metering device used in the automotive HVAC system. The most widely used device is the thermostatic expansion valve or thermal expansion valve (TXV). Another device originally introduced by General Motors and now found on many car lines (Schenubel, 2017), is the expansion tube, more commonly referred to as an orifice tube.

The TXV separates the high-pressure and low-pressure side of the system. A small variable orifice in the valve allows only a small amount of liquid refrigerant to enter the evaporator (from port 2 to port 1 in Figure 23). The amount of refrigerant passing through the valve is governed by the evaporator outlet temperature. A tapered pin is raised or lowered in an orifice to change the size of the opening up to the maximum (often in several tenths of mm range). The TXV is designed to provide two basic functions:

- Based on various heat loads and compressor output, the expansion valve meters the flow of refrigerant into the evaporator.
- Refrigerant pressure is reduced as high-pressure liquid entering the valve passes through a restriction and suddenly expands and vaporized into a low-pressure mist.

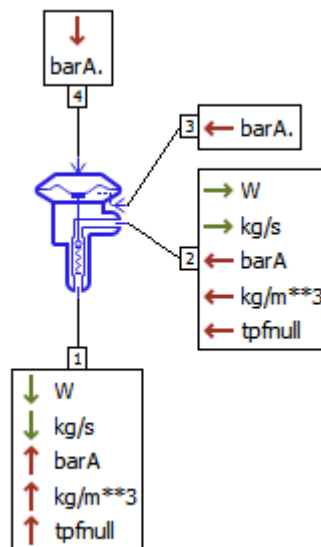


Figure 23. Schematic drawing for the TXV model in AMESim (Siemens, 2019)

H-valve is a newer type of TXV. The refrigerant enters the valve (port 4 in Figure 24) through the high-pressure liquid line and passes through a variable restriction that regulates

the pressure to the evaporator. As the refrigerant leaves the evaporator, it travels back through the upper outlet port (port 2 in Figure 24) of the H-valve and passes over the temperature-sensing sleeve (internal sensing bulb) contained in the passage, transferring some heat to the refrigerant contained in the power dome diaphragm. This causes the refrigerant contained in the power dome to expand and contract based on the temperature of the refrigerant leaving the evaporator. The expansion and contraction exert pressure on the sensing cavity diaphragm, causing the valve pin to move up and down and in turn regulates the flow of the refrigerant through the evaporator core, thus regulating core temperature. Its purpose, like the standard TXV, is to sense suction line refrigerant temperature. Operation and function of the H-valve are essentially the same as for the TXV (Schenubel, 2017).

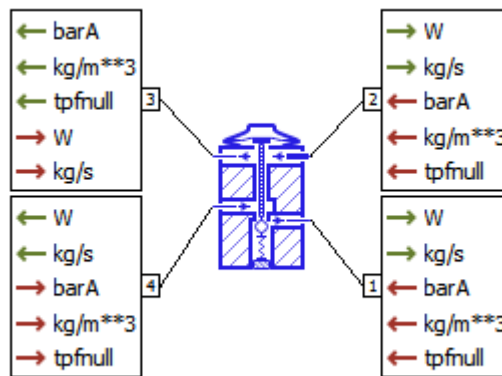


Figure 24. Schematic drawing for the H-valve model in AMESim (Siemens, 2019)

The TXV characteristic curves are described in a four-dimension diagram shown in Figure 25. In quadrant 1, the refrigerant saturation curve and valve opening curve as a function of thermal sensing bulb fluid are defined. In quadrant 2, the evaporator outlet pressure is defined as a function of the valve lift for different constant temperature values (Figure 25 only shows the curve for one temperature). In quadrant 3, the evolution of the reference mass flow rate is defined as a function of the valve lift, which is an asymptotic curve to the maximum mass flow rate. In quadrant 4, the evolution of the reference mass flow rate is defined as a function of the evaporator outlet temperature. The curves in four quadrants depend on each other (Niu, Lai and Wei, 2018).

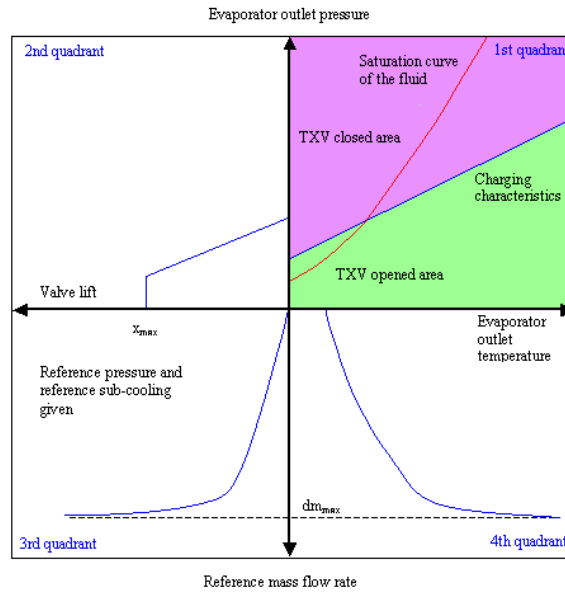


Figure 25. Four-dimension diagram of TXV model in AMESim (Siemens, 2019)

3 Formulation of the Simulation Model

This chapter discusses the system level simulation that was made based on e-Muuli, the prototype electric city bus from VTT. The focus of the simulation is to accurately simulate the current system on e-Muuli, especially the thermal related system such as the cabin and HVAC. The final simulation model has the functionality of simulating the operation of electric buses on driving cycles in different ambient temperatures. This chapter will mainly focus on the model itself and the next chapter will mainly focus on the characterization and validation of the model.

3.1 The e-Muuli Prototype Bus

The e-Muuli (e-Mule) is a battery electric city bus prototype owned by VTT Technical Research Centre of Finland and has been used for various research projects in VTT and other companies, universities and organizations.

The e-Muuli was converted from a KABUS-branded 12m diesel-powered city bus into a battery electric bus in the eBUS project (Erkkilä *et al.*, 2013). The project was a comprehensive research and demonstration project funded by TEKES and participated by VTT, Aalto University, Metropolia and many other partners (Laurikko *et al.*, 2015). The choice for converting a city bus was made because the city bus is a typical application for heavy-duty electric components and offers enough space for prototype structures. It provides a neutral test environment to test individual components or partial system of a battery electric vehicle.

The e-Muuli has a full aluminium self-supporting lightweight body. It has a total length of 11.47 m and a total weight of 11515 kg (the version which is used in the dynamometer test in 2017, as discussed in 4.3).



Figure 26. The E-Muuli prototype bus (Ari-Pekka Pellikka, 2017)

3.2 Simulation Model Overview

The simulation model of e-Muuli was developed using the components and libraries available in AMESim. The model is built on a demo model of a battery electric vehicle in combination with several other demo models, such as car cabin, powertrain cooling, and HVAC control. As discussed in Section 1.5.2, the simulation model is made under the idea of Multi-level modelling. Since the focus of the thesis is on thermal design, the thermal-related systems in a battery electric vehicle are simulated in detail, such as cabin and HVAC, while other parts are simulated on a relatively simple way, such as chassis and transmission.

The work is focused on redesigning the existing system and parameterization of the components to make the model an accurate simulation of E-Muuli. Some parts of the model, including the HVAC system, are built from scratch. The parameters of the model are measured from the e-Muuli directly or from technical documents and CAD files.

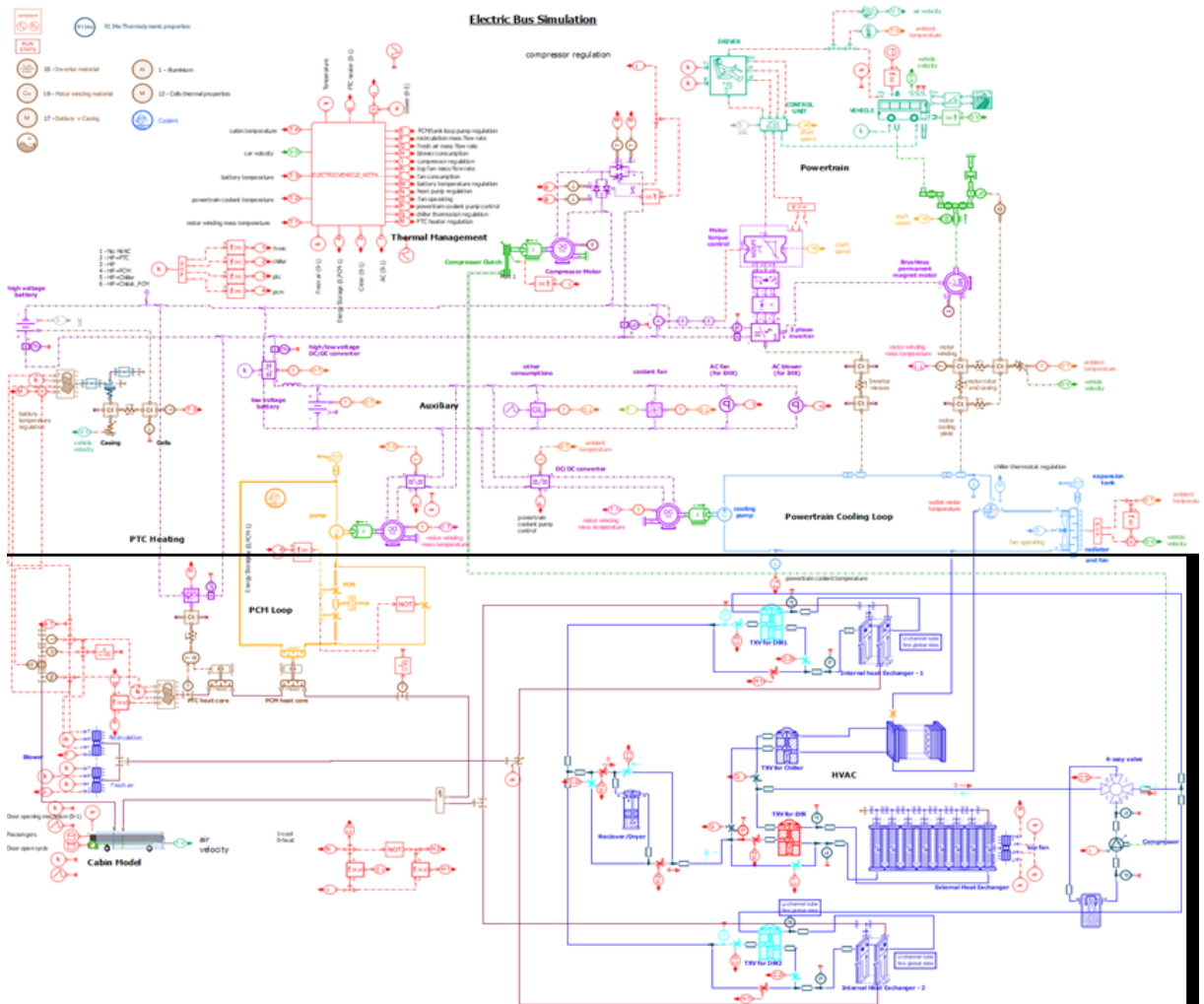


Figure 27 Battery Electric Bus Simulation Model in AMESim

3.3 Driver and Vehicle Control

Figure 28 shows the driver and the vehicle control unit of the model.

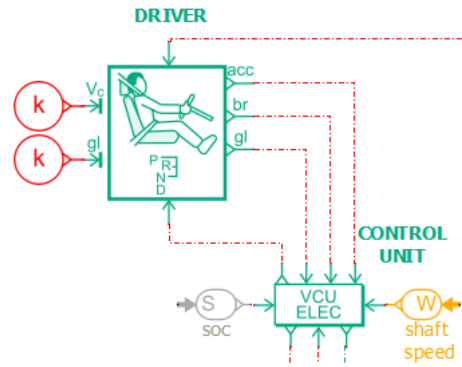


Figure 28. Driver and vehicle control unit model in the simulation

3.3.1 Driver

In the model, the driver is in charge of controlling the speed of the vehicle to follow the input speed profile. The driver gives the signal, such as the accelerator, brake, and gear, to the vehicle control unit. Figure 29 shows the parameters for the component.

Title	Value	Unit	Name
cycle type	cycle with slopes		slp
advance time for control anticipation	1	s	advAnt
▼ <input type="checkbox"/> cycle definition			
driving cycle	personal		timecycle
filename for target vehicle velocity [m/s] = f(time [s])	...rom Pekka/speed_1.data		tpcyclevtime
data out of range mode for data files	extreme value		mode
discontinuity handling	inactive		disc
▼ <input type="checkbox"/> acceleration control			
(#) integral part of the acceleration control loop	0	m	Iacc
anticipative gain for acceleration control loop	0.3	1/(m/s/s)	GAacc
proportional gain for acceleration control loop	0.5	1/(m/s)	GPacc
integral gain for acceleration control loop	0.5	1/m	GIacc
▼ <input type="checkbox"/> braking control			
(#) integral part of the braking control loop	0	m	Ibr
anticipative gain for braking control loop	0.3	1/(m/s/s)	GAbr
proportional gain for braking control loop	1	1/(m/s)	GPbr
integral gain for braking control loop	0.5	1/m	GIbr
use braking pedal during stops	no		BrakeVehStop
brake value during vehicle stop	80	percent	brkstop

Figure 29. Parameters for the driver model in the simulation

In the driver model, the acceleration command and brake command are calculated based on the error of the speed e between the controlled speed V_{cont} and vehicle speed V_{veh} .

$$e = V_{cont} - V_{veh} \quad (7)$$

The dimensionless acceleration control output $acc \in [0,1]$ from the acc port is a linear combination of the error of speed e , the integral of the error and a term function of the future anticipated speed $dv_{contAnt}$. The gains associated with each term ($GPacc$, $GIacc$, $GAacc$) are defined by the user, so that:

$$a = GPacc \cdot e + GIacc \cdot \int e \cdot dt + GAacc \cdot dv_{contAnt} \quad (8)$$

with

$$dv_{contAnt} = \frac{v_{contAnt} - v_{cont}}{advAnt} \quad (9)$$

where $v_{contAnt}$ is the control speed at the time $t + advAnt$.

The dimensionless braking control output $br \in [0,1]$ is also a linear combination of the error of speed e , the integral of the error and a term function of the future anticipated speed $dv_{contAnt}$. The gains ($GPbr, Glbr, GAbr$) are associated with each term so that:

$$br = -GPbr \cdot err - Glbr \cdot \int err \cdot dt - GAbr \cdot dv_{contAnt} \quad (10)$$

3.3.2 Vehicle Control Unit

The vehicle control unit (VCU) gathers the information from the driver and the vehicle, sends the required torque command to the motor inverter and sends the brake command to the vehicle. The information it gathers includes battery SOC, motor shaft speed, maximum available torque from the motor, and commands from driver mentioned above. Figure 30 shows the parameters of the component, in which two global parameters are defined as Figure 31.

Title	Value	Unit	Name
acceleration command type at port 5	signal [0..1]		typec
brake command type at port 6	signal [0..1]		typeb
use regenerative braking	yes		useregbrake
maximum braking torque for the vehicle	maxbraketorq	Nm	maxtorqveh
gear ratio between the electric motor and the vehicle	gearratio	null	gearratio
<input type="checkbox"/> regenerative braking			
regenerative braking strategy	series		regstrategy
high rpm threshold for regenerative braking	50	rev/min	speedregactive
low rpm threshold for regenerative braking	40	rev/min	speedregdeactive
high SOC threshold for regenerative braking	100	percent	SOCregdeactive
low SOC threshold for regenerative braking	99	percent	SOCregactive

Figure 30 Parameters for the vehicle control unit model in the simulation

maxbraketorq	maximum brake torque	6000 Nm
gearratio	gear ratio between the electric motor and the vehicle	4.88 null

Figure 31. Global parameters used in the vehicle control unit model in the simulation

Inside the model, the driving torque is calculated as follow:

$$T_{driving} = acc \cdot T_{max\ inv} \quad (11)$$

where $T_{max\ inv}$ is maximum electric motor torque from the inverter.

The brake torque is calculated as follow:

$$T_{brake} = br \cdot T_{max\ brake} \quad (12)$$

where $T_{max\ brake}$ is maximum braking torque for the vehicle.

There are various strategies for regenerative braking, shown in Figure 32. In the simulation, the series method is selected. The motor is used to brake the vehicle and regenerate the battery. If the motor is not able to provide the requested torque, the VCU uses vehicle brakes to complete the braking.

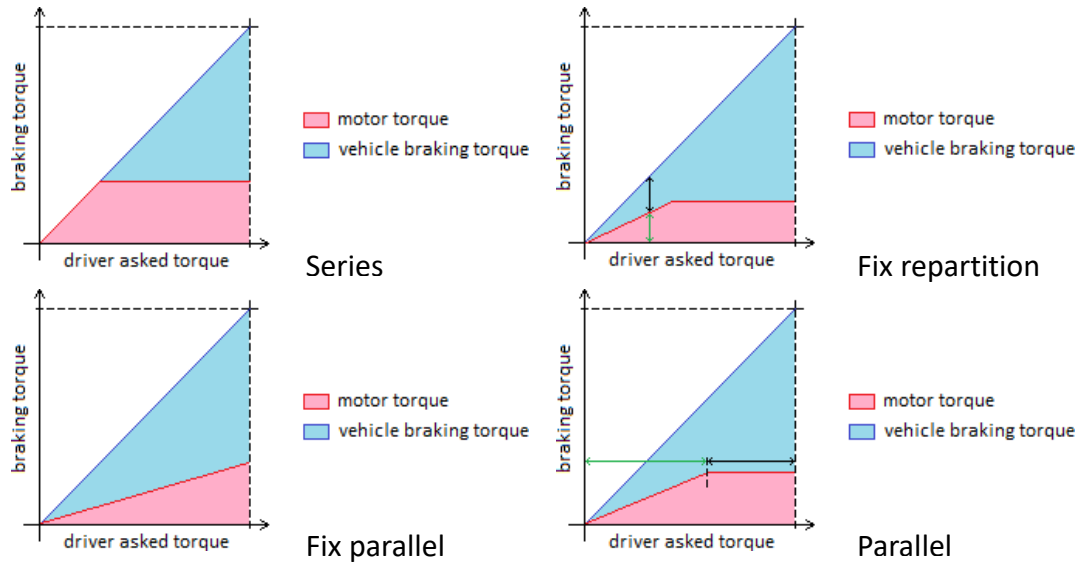


Figure 32. Different strategies for regenerative braking used in AMESim (Siemens, 2019)

3.4 Powertrain

Figure 33 shows the powertrain of the battery electric bus model, which includes a permanent magnet synchronous motor (PMSM), the inverter for the motor, the transmission, and the bus itself.

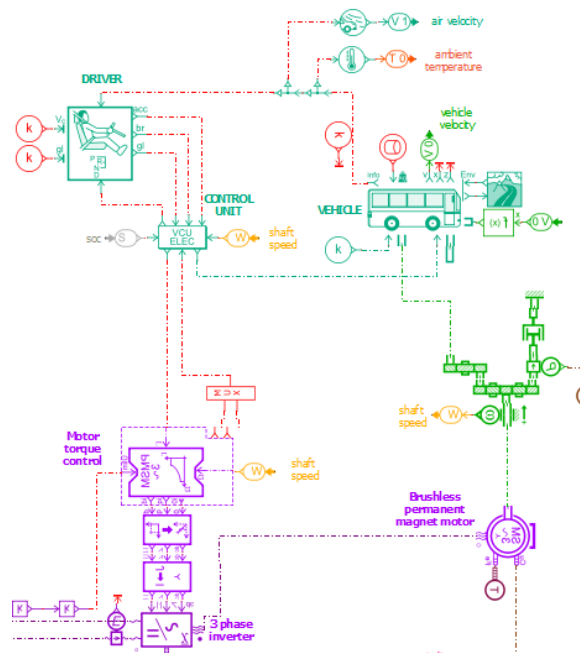


Figure 33. Powertrain model in the simulation

The motor and inverter that are used are both quasi-static sub-models for PMSM; the transient behaviours, such as electrical inductive dynamics of the motor, are neglected. Figure 34 demonstrates the difference between a quasi-static inverter model (the blue curve) and a more detailed 3 arm average inverter model (the red curve).

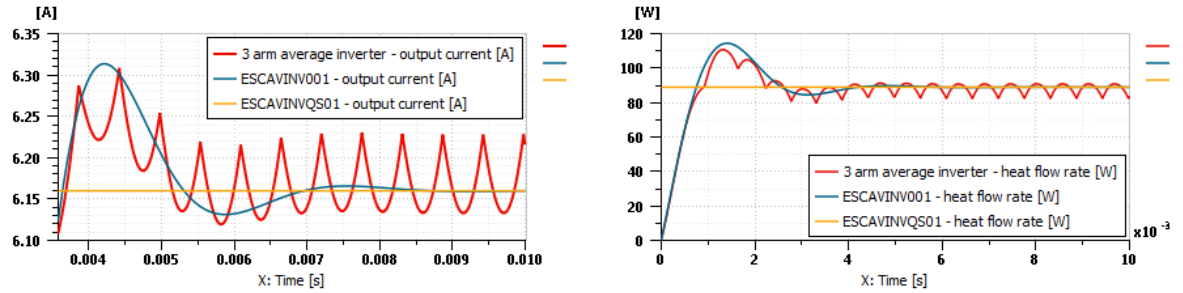


Figure 34. Simulation results comparing quasi-static and transient sub-models of PMSM (Siemens, 2019)

3.4.1 Motor

The motor is modelled based on the direct-cooled ‘Kooler’ prototype motor currently installed in e-Muuli, developed by LUT University and Saimia (Lindh *et al.*, 2019). Some of the parameters of the ‘Kooler’ motor are shown in Table 3. It uses a dedicated liquid cooling loop to cool down both the stator and rotor of the motor, contrary to the general liquid cooling loop that cools down all the powertrain components used in many commercial electric city buses (Lajunen and Kalttonen, 2015). Therefore, the electronics characteristics of the ‘Kooler’ motor are modelled in the simulation while the direct cooling behaviour of the motor is not modelled. The parameters of the motor are shown in Figure 36, in which several global parameters are defined as Figure 37.

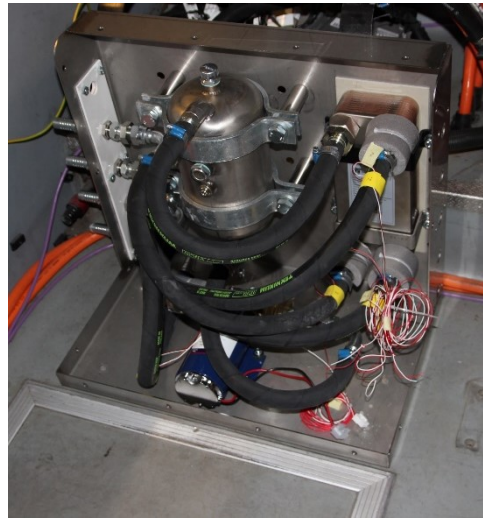


Figure 35. Coolant pump for the direct-cooled ‘Kooler’ motor (Lindh *et al.*, 2019)

Table 3. Parameters for the ‘Kooler’ motor on e-Muuli

Unit	Model	Parameters	Value
Motor	Saimia & LUT Direct water-cooled PM motor	Power	205 kW (norm)
		Torque	1300 Nm (norm)
		Speed	1500 rpm (norm)
		Current	300 A _{rms} (norm)

Title	Value	Unit	Name
Ⓜ electrical angle		0 degree	thetae
iron losses computation	yes		dhiComp
characterization coordinates	Cartesian (d,q)		CharactType
winding connection	connectType		connectType
number of pole pairs	p		p
stator windings reference temperature	25	degC	Tw0
stator winding resistance at reference temperature	Rs	Ohm	Rs0
corrective coefficient on stator winding resistance	0	1/K	alphaRs
stator end winding inductance	0	H	lsew
flux linkage d filename or expression [Wb] as a function of current d [A] and current q [A] ('Id' and 'Iq' i...	Lsd*Id+sqrt(3/2)*Phif		filePsisdC
flux linkage q filename or expression [Wb] as a function of current d [A] and current q [A] ('Id' and 'Iq' i...	Lsq*Iq		filePsisqC
iron losses filename or expression [W] as a function of current d [A], current q [A] and speed [rev/min]...	400		fileIronLC
▾ <input type="checkbox"/> numerical parameters			
Iq sign transition type	sharp		ITransType
minimum speed for full iron losses	100	rev/min	WminIron
▾ <input type="checkbox"/> interpolation parameters			
interpolation type	linear		intType
linear data out of range mode	linear extrapolation		lmode
discontinuity handling	active		disc

Figure 36. Parameters for the motor model in the simulation

s	salient ratio	Lsq/Lsd	null
r	relative ratio	Lsd*Imax/Phif	null
Lsq	machine stator cyclic inductance q	Rs*1.1	H
Lsd	machine stator cyclic inductance d	Rs*0.9	H
Imax	Maximum rms current	410	null
p	pole pairs	4	null
Phif	machine permanent magnet flux linkage	1	Wb
connectType	winding connection	star	
Rs	machine stator resistance	0.016	Ohm
Ls	machine stator cyclic inductance	0.002	H

Figure 37. Global parameters used in the motor model in the simulation

The motor receives the line current with RMS magnitude and the phase angle information from the inverter and return the line to neutral voltage RMS magnitude and the phase angle information back to the inverter. The connecting port to the transmission gives the torque based on the rotation speed of transmission. It also has two thermal ports, for both rotor heat generation (Fe loss) and stator winding heat generation (Cu loss).

The electromagnetic torque is computed using flux linkage and currents, minus iron losses:

$$T_{em} = p(\Psi_{sd}I_{sq} - \Psi_{sq}I_{sd}) - \frac{\delta h_{iron}}{\omega_{dif}} \quad (13)$$

In which Ψ_{sd} and Ψ_{sq} are the d and q axes flux linkage, I_{sq} and I_{sd} are the stator current on d and q axes, p is the number of pole pairs, δh_{iron} is the iron losses, ω_{dif} is the speed difference between stator and rotor.

3.4.2 Inverter

The inverter is modelled based on the Visedo PowerMASTER PMA-M-250 inverter currently installed in e-Muuli. There are two units installed in e-Muuli as shown in Figure 38, one of which is for the driving motor (on the left) and the other for the compressor for the HVAC system and air compressor for the pneumatic loop (on the right). Some of the parameters of the Visedo inverter are listed in Table 4. In the simulation model, the parameters of the inverter are presented in Figure 39.



Figure 38. Inverters for PMSM (left) and auxiliary compressors (right)

Table 4. Parameters for the Visedo Inverters

Unit	Model	Parameters	Value
Inverter for PMSM	Visedo PowerMASTER PMA-M-250	DC Connection	750 V (norm), 950 V (max)
		AC Connection	0-560 V _{EFF} , 0-580 Hz, 300 A _{rms} (norm)
		Nominal Power	250 kW
		Cooling	water cooling (max 50:50 % glycol/water, >10 l/min, max 2 bar)

Title	Value	Unit	Name
losses definition	semiconductor characteristics		lossCalcMethod
space vector modulation	with neutral voltage = 0		modMet
<input type="checkbox"/> semiconductor characteristics			
transistor forward threshold voltage	0.65	V	Vtth
transistor on-state resistance	(0.0087+0.013)/2	Ohm	Rton
diode forward threshold voltage	0.65	V	Vdth
diode forward resistance	(0.0087+0.013)/2	Ohm	Rdon
switching frequency	8000	Hz	Fc
switching energy per period per phase at reference voltage and current	0.01	J	Eswref
reference DC voltage	750	V	Uref
reference current	300	A	Iref
<input type="checkbox"/> numerical parameters			
minimum power for efficiency calculation	0.05	W	minP
minimum input voltage	1e-06	V	Umin

Figure 39. Parameters for the inverter model in the simulation

The inverter transfer DC current from the high-voltage battery to 3-phase current that supports the motor. Three other components – torque to current command for PMSM, dq0 to space phasor transformation, and space phasor (phase to line current transformation) – are needed to transfer torque command from VCU to the commands that the inverter could directly read; in this case, the commands are line current RMS magnitude command, line current phase angle command, and DC current command.

3.4.3 Body of the Bus

The body model of the bus simulates the physics of the vehicle. The model is based on the physical parameters of e-Muuli, which are listed in Table 5. There are different vehicle configurations available in the bus model, including ‘road’ mode and ‘roller test bench’ mode, for which different parameters are needed. In road mode, rolling friction, road slope

and aerodynamic drag is taken into account. In roller test bench mode, resistance is calculated from user-defined roller test bench friction coefficients. For this and next chapter, roller test bench mode is used since the simulation model of the powertrain is validated with roller test bench experiment data for e-Muuli. For Chapter Thermal Management Solutions in which thermal management simulation is discussed, the road mode is used for simulating real-world bus lines. The parameters for both modes are presented in Figure 40 and Figure 41 respectively.

Table 5. Parameters for the body of e-Muuli

Unit	Model	Parameters	Value
Body	KABUS	Length	11467 mm
		Width	2483 mm
		Height	2343 mm
		Empty Weight	10715 kg
		Tire Radius	0.43 m
		Frontal Area	6.2 m ²
		Rolling Resistance Coefficient	0.008
		Drag Coefficient	0.493

Title	Value	Unit	Name
Ⓜ vehicle linear velocity at port 5	0	m/s	v5
Ⓜ vehicle position at port 5	0	m	x5
Ⓜ vehicle linear displacement at port 12	0	m	disp
vehicle index	1		index
vehicle configuration	road		vehetype
longitudinal slip configuration	without slip		sliptype
icon	bus		icon
total vehicle mass	10715	kg	mtot
▾ aerodynamic and rolling parameters			
Coulomb friction coefficient (rolling resistance coef)	0.008	null	f
viscous friction coefficient (rolling resistance coef)	0	1/(m/s)	k
windage coefficient (rolling resistance coef)	0	1/(m/s)**2	wind
air penetration coefficient (Cx)	0.493	null	Cx
vehicle active area for aerodynamic drag	6.2	m**2	S
stiction coefficient	1.2	null	Cstat
▾ wheel characteristics			
front/rear wheels	same dimension		wheelsdef
number of wheels on the front axle	2		nbrwheelfrontaxle
number of wheels on the rear axle	2		nbrwheellrearaxle
wheel inertia	16	kgm**2	Jw
wheel radius definition	with radius		wheelradiusdef
wheel radius	0.43	m	wheelradius
filename or expression for wheel radius dynamic gain [fraction] = f(vehicle velocity: Vveh [m/s], vehicle mass: mass [kg])	0.97		tpRdyn
▾ brake characteristics			
maximum braking torque on rear axle	0	Nm	maxbrakerear
maximum braking torque on front axle	maxbraketorq	Nm	maxbrakefront
rotary stick velocity threshold for brake	1e-06	rev/min	dvel

Figure 40. Parameters for the bus model in the simulation - road mode

Title	Value	Unit	Name
vehicle configuration	roller test bench		vehetype
longitudinal slip configuration	without slip		sliptype
icon	bus		icon
total vehicle mass	10715	kg	mtot
▾ aerodynamic and rolling parameters			
roller test bench config: coefficient 'a'	852.42	N	coefA
roller test bench config: coefficient 'b'	0.983	N/(m/s)	coefb
roller test bench config: coefficient 'c'	0.1253	N/(m/s)**2	coefc
stiction coefficient	1.2	null	Cstat

Figure 41. Parameters for the bus model in the simulation - roller test bench mode

The total vehicle mass m_{veh} accounting for wheel inertia effect in linear motion is:

$$m_{veh} = m + m_{add} + n_{front} \cdot \frac{J_{W_{front}}}{R_{W_{front}}^2} + n_{rear} \cdot \frac{J_{W_{rear}}}{R_{W_{rear}}^2} \quad (14)$$

where m is the total mass of the vehicle, m_{add} is the additional mass, n_{front} is the number of wheels on front axle, $J_{W_{front}}$ is the inertia of a front wheel, $R_{W_{front}}$ is the front wheel radius, n_{rear} is the number of wheel on rear axle, $J_{W_{rear}}$ is the inertia of a rear wheel, $R_{W_{rear}}$ is the rear wheel radius.

The driving force $F_{driving}$ is calculated as follows:

$$F_{driving} = \frac{T_2}{R_{dyn_{rear}}} + \frac{T_4}{R_{dyn_{front}}} \quad (15)$$

where T_2 and T_4 are the input torques at the rear and front axle, $R_{dyn_{front}}$ is the front wheel dynamic wheel radius, $R_{dyn_{rear}}$ is the rear wheel dynamic wheel radius.

The resistive forces of the vehicle consist of braking torques, climbing resistance, and other resistance, the last part of which is calculated differently in road and roller test bench mode.

For each axle, the braking torque $T_{b,i}$ is calculated by a hyperbolic tangent approach. It is obtained from the dynamic braking torque $T_{dyn,i}$ which is modulated as a function of the relative rotary speed ω_{rel} between the wheel and the brake calliper:

$$T_{b,i} = T_{brake,max,i} \cdot \tanh\left(2 \cdot \frac{\omega_{rel,i}}{d\omega}\right) = \mu \cdot F_N \cdot \tanh\left(2 \cdot \frac{\omega_{rel}}{d\omega}\right) \quad (16)$$

$$T_{dyn,i} = T_{brake,max,i} \cdot sig_i \quad (17)$$

where $T_{b,i}$ is the braking torque on axle i , sig_i is the braking command on axle i , $T_{brake,max,i}$ is the maximum braking torque that the braking system can apply on axle i , $d\omega$ is the rotary stick velocity threshold for brake.

Then the braking force applied to the vehicle from the braking system is given by:

$$F_b = \frac{T_{b,front} + T_{b,rear}}{R_{dyn}} \quad (18)$$

The climbing resistance F_{cl} is given by:

$$F_{cl} = mass \cdot g \cdot \sin\left(\arctan\left(\frac{\alpha}{100}\right)\right) \quad (19)$$

where $mass$ is the total mass of the vehicle, g is the gravity acceleration, α is the road slope in percentage.

In road configuration, the resistive forces applied to the vehicle are calculated as:

$$F_{res} = F_{cl} + F_{aero} + F_{roll} \quad (20)$$

The aerodynamic drag is calculated as:

$$F_{aero} = \frac{1}{2} \cdot \rho_{air} \cdot S \cdot C_x \cdot (v + v_{wind})^2 \quad (21)$$

where ρ_{air} is air density, C_x is the air penetration coefficient, S is the vehicle active area, v is the vehicle linear velocity, v_{wind} is the input wind velocity.

The rolling friction forces are given by:

$$F_{roll} = mass \cdot g \cdot (f + k \cdot v + wind \cdot v^2) \quad (22)$$

Where rolling resistance is calculated in three segment with three coefficient defined by user – Coulomb friction coefficient f , viscous friction coefficient k , and windage coefficient $wind$.

In the roller test bench configuration, the resistive forces are calculated as follows:

$$F_{res} = F_{cl} + a + b \cdot v + c \cdot v^2 \quad (23)$$

where a , b , c are user defined parameters.

The vehicle linear acceleration is given by:

$$\gamma = \frac{F_{dr} - F_b + F_{res}}{m_{veh}} \quad (24)$$

The powertrain the simulation with driver and VCU are further validated with the dynamometer test of e-Muuli, the result of which is presented in the next Chapter.

3.5 Battery

3.5.1 High Voltage Battery

The high voltage battery pack is the power source for the whole electric bus. The simulation model of the high voltage battery pack and its cooling solution is shown in Figure 42.

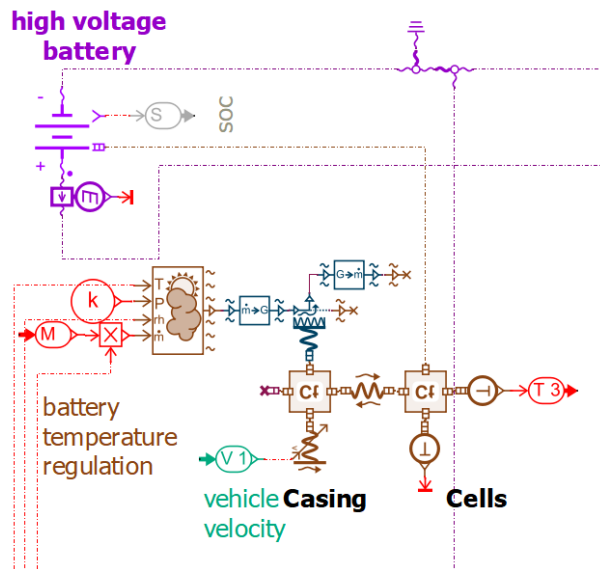


Figure 42. High voltage battery model in the simulation

In e-Muuli, 8 packs of LTO battery from Leclanché are installed, 4 of which are located at the front cabin under the side floor while the others are located at the rear cabin, as shown in Figure 43 and Figure 44. The parameters for the battery are listed in Table 6. The 8 battery

packs are in series. Each pack includes 32 ‘boxes’ of battery which are arranged in series. Inside each ‘box’, there are three battery cells in parallel.



Figure 43. Leclanché LTO battery packs at the front cabin (VTT, 2016)



Figure 44. Leclanché LTO battery packs at the rear cabin (VTT, 2016)

Table 6. Parameters for the Leclanché LTO battery pack of e-Muuli

Unit	Model	Parameters	Value
High-voltage battery	Leclanché	Cell type	Lithium Titanite ($Li_4Ti_5O_{12}$ or LTO)
		Arrangement	8 packs * 32 series * 3 parallel
		Capacity	~90 Ah
		Voltage	min 435 V, norm 540 V, max 691 V

The simulation model is built based on the Leclanché LTO battery. The general parameters for the high voltage battery in the simulation are shown in Figure 45. The open circuit voltage (OCV) curve of one battery cell used in the simulation is shown in Figure 46. The OCV data is provided by Leclanché.

Title	Value	Unit	Name
Ⓢ state of charge at port 4	98	null	soc
Ⓢ output voltage	645	V	U
temperature influence	no		tinfl
scope of the nomcap, Cf, ocvFile and resistFile parameters	one cell		scope
number of cells in series in one branch	256		ns
number of branches in parallel	3		np
nominal capacity	30	Ah	nomcap
open circuit voltage [V] as a function of state of charge [null] ('soc' in expres...	...OCV_Leclanche_cell_SOC.data		ocvFile
ohmic resistance [Ohm] as a function of state of charge [null] ('soc' in expres...	0.00225		resistFile
▾ numerical parameters			
filtering capacitance	25*114	F	Cf
minimum admissible value of resistance	1e-10	Ohm	rmin
▾ interpolation parameters			
interpolation type	linear		inttype
linear data out of range mode	extreme value		lmode
discontinuity handling	active		disc

Figure 45. Parameters for the high voltage battery model in the simulation

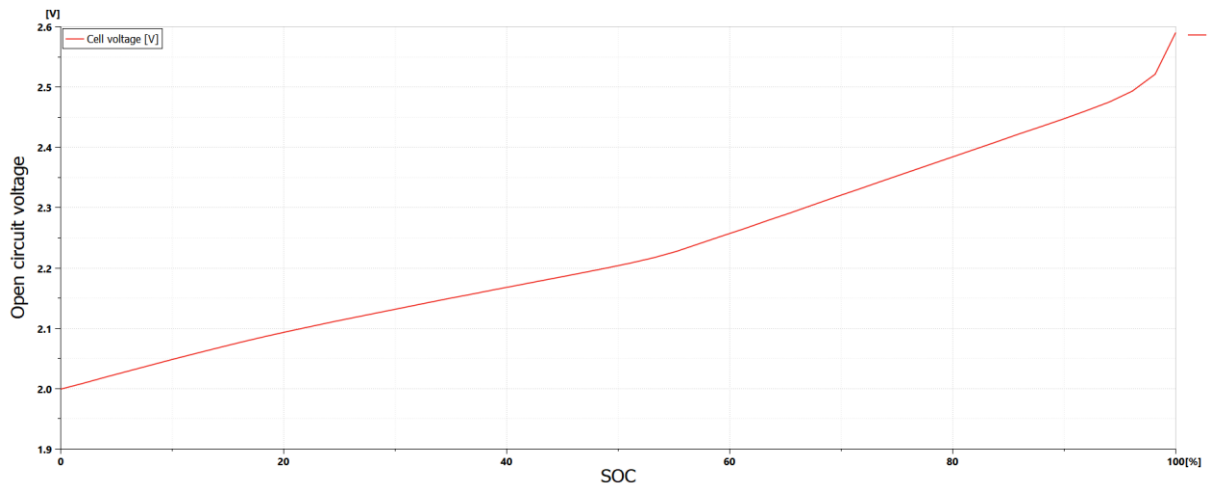


Figure 46. Open circuit voltage curve for one Leclanché LTO battery cell used in the simulation

In e-Muuli, the high voltage battery pack is planned with liquid cooling circuits but was not installed. In the simulation model, the battery pack is air-cooled. The moist air source from the cabin is blown to the case of the battery, which conducts heat with battery cells. The cooling regulation is integrated into the thermal management controller.

3.5.2 Low Voltage Battery and Auxiliaries

The low voltage battery pack is used as a power source for auxiliaries. The 24V battery pack is connected to the high voltage circuit with a DC-DC converter and is always floating-charged when the high voltage battery is in use.

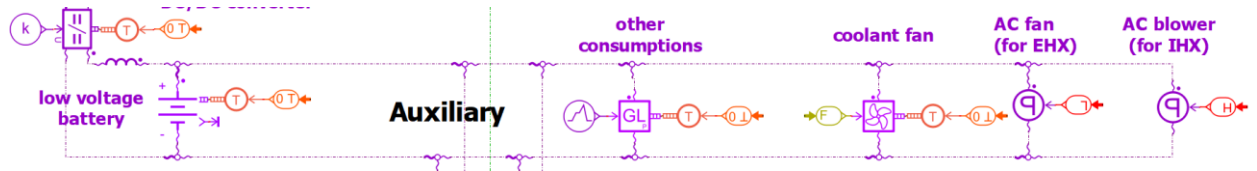


Figure 47. Low voltage battery model with the auxiliary circuit in the simulation

The parameters for the low voltage battery in the simulation is shown in Figure 48. The open circuit voltage (OCV) curve of one battery cell used in the simulation is shown in Figure 49. The OCV file is the approximation of an average low voltage battery cell.

Title	Value	Unit	Name
Ⓢ state of charge at port 4	80	null	soc
Ⓢ output voltage	24	V	U
temperature influence	no		tinfl
scope of the nomcap, Cf, ocvFile and resistFile parameters	one cell		scope
number of cells in series in one branch	10		ns
number of branches in parallel	1		np
nominal capacity	10	Ah	nomcap
open circuit voltage [V] as a function of state of charge [null] ('soc' in expression)	...files/low_v_battery_ocv.data		ocvFile
ohmic resistance [Ohm] as a function of state of charge [null] ('soc' in expression)	0.00225		resistFile
▾ <input type="checkbox"/> numerical parameters			
filtering capacitance	5/6	F	Cf
minimum admissible value of resistance	1e-10	Ohm	rmin
▾ <input type="checkbox"/> interpolation parameters			
interpolation type	linear		intItype
linear data out of range mode	extreme value		lmode
discontinuity handling	active		disc

Figure 48. Parameters for the low voltage battery model in the simulation

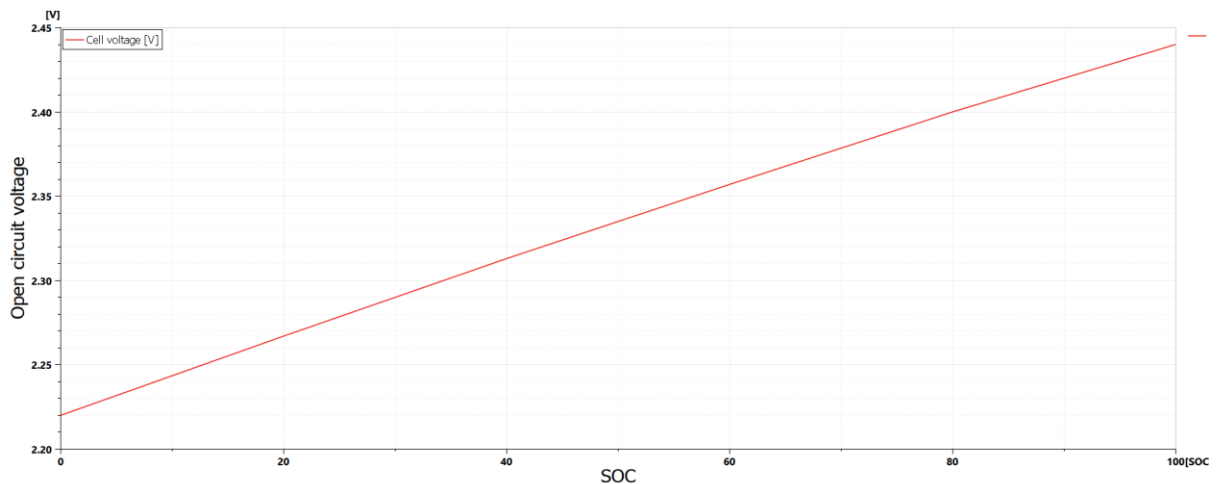


Figure 49. Open circuit voltage curve for one low voltage battery cell used in the simulation

The 24V auxiliary circuit is powering the coolant pump, coolant fan, HVAC top fan, HVAC blower, and an input port which includes other auxiliary load such as air compressor and lights.

3.6 Powertrain Cooling Loop

The powertrain cooling loop used in the simulation model is based on a predefined electric passenger car model in AMESim. Parameters are changed to match the cooling requirement for a battery electric city bus.

The cooling loop is connected with the thermal ports from the inverter and the stator of the motor, while the rotor of the motor is air-cooled. The loop is driven by a DC-motor-powered compressor. The compressor motor is connected to the 24V low voltage circuit with a DC-DC converter that controls the voltage to the motor in order to control the speed. The control scheme of the compressor and the radiator fan will be presented in the form of simulation results in Section 4.2.

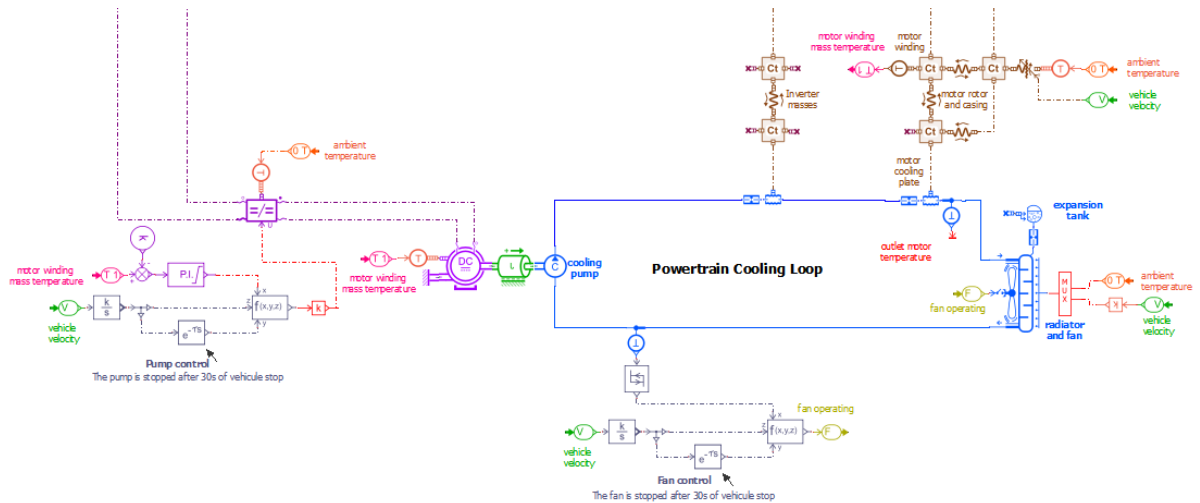


Figure 50. Powertrain cooling loop model in the simulation

The pump used in the cooling loop is a thermal-hydraulic centrifugal pump. The pressure increases of the fluid passing through the pump are calculated using affinity laws. The characteristics of a reference pump in reference operating conditions are known. The behaviour of the pump model is deduced from the reference pump. The fluid temperature at the pump outlet is computed from the temperature at the pump inlet and the energy provided (with an overall efficiency) by the pump to the fluid. The parameters for the pump are shown in Figure 51. The pressure characteristics of the reference pump are shown in Figure 52.

Title	Value	Unit	Name
⊕ pressure at port 2		Pamb barA	p2
⊕ temperature at port 2		Tcoolant degC	t2
index of thermal hydraulic fluid		1	fi
characterization mode		f(qv)	charmode
fluid volume associated with the pump		0.001 L	pvol
time constant		1e-05 s	tau
pump diameter		10 mm	dia
▾ <input type="checkbox"/> reference parameters			
reference pump diameter		13 mm	dref
reference speed		1200 rev/min	refspeed
reference density setting		direct	refprop
reference density		1049 kg/m**3	refrho
▾ <input type="checkbox"/> pressure difference table	AMETable		
interpolation type		cubic	interp
discontinuity handling		inactive	disc
boundary conditions along X axis		natural (y'=0)	bcond
cubic data out of range along X axis		cubic	cmode
filename for pressure increase[bar] = f(qv[L/min], w[rev/min], T[degC])	Cooling_loop_lv1_v3_datafiles/dP.data		dpfile
▾ <input type="checkbox"/> efficiency			
global efficiency		constant	effi
constant global efficiency		1 null	consteff

Figure 51. Parameters for the pump model in the simulation

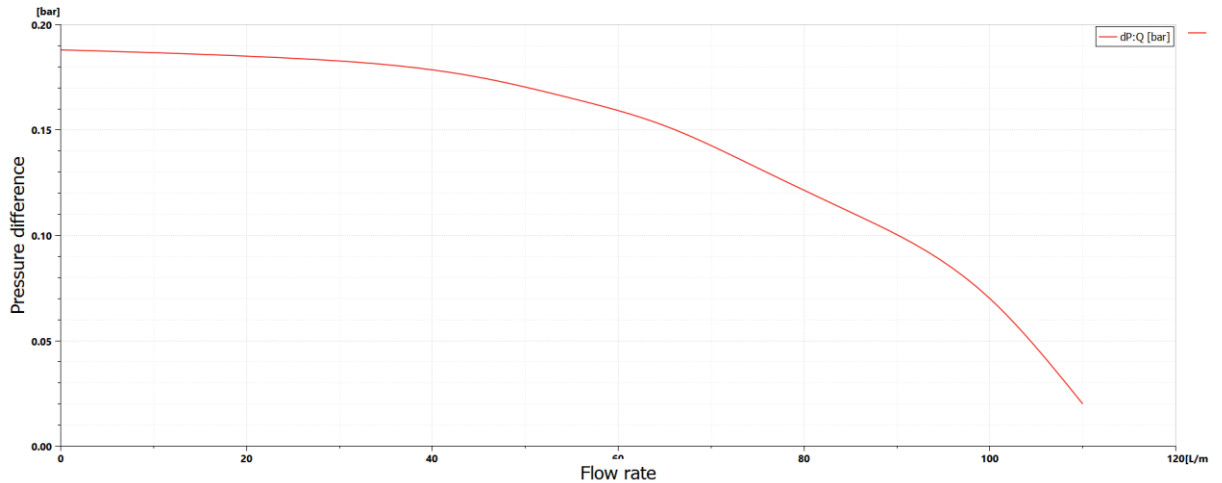


Figure 52. Pressure difference curve for a reference pump used in the simulation

The mass flow rate at port 1 is calculated so that the output pressure (high pressure) reaches the following value:

$$p_{out} = p_{in} + \Delta p \quad (25)$$

where p_{in} is the input pressure (low pressure) and Δp is the pressure difference. The pressure difference into the pump is interpolated thanks to the reference data.

The fluid outlet temperature and pressure are calculated using TFC utility in AMESim. The power P_{mech} provided by the pump to the fluid is as follows:

$$P_{mech} = \frac{Q \cdot \Delta p}{f_{eff}} \quad (26)$$

where Q is the volumetric flow rate, Δp the pressure difference and f_{eff} the global efficiency.

The controller for coolant pump and the radiator fan is separated from the coolant loop model and is integrated into the thermal management controller, which is discussed in section 3.9.

3.7 Cabin

The cabin model is a mono-zonal model that considers cabin air as a uniformed thermal mass with homogeneous properties. The cabin air could interact with the environment through various other thermal masses (interfaces). The model is shown in Figure 53. The moist air is depicted in brown solid line, while the thermal flow is depicted in brown dash line. The cabin is modelled based on a predefined advanced cabin model for passenger cars, which is modified and enhanced for the simulation of the cabin of e-Muuli. Compared to passenger cars, city buses will open doors more frequently. Hence, doors opening model is built to the cabin model to simulate the effects of opening doors to the thermal management. The data used in the doors opening model is the CFD simulation data from Aku Karvinen of VTT. The cabin of e-Muuli is not as airtight as many commercial city buses, so the air infiltration effect is also added to the model.

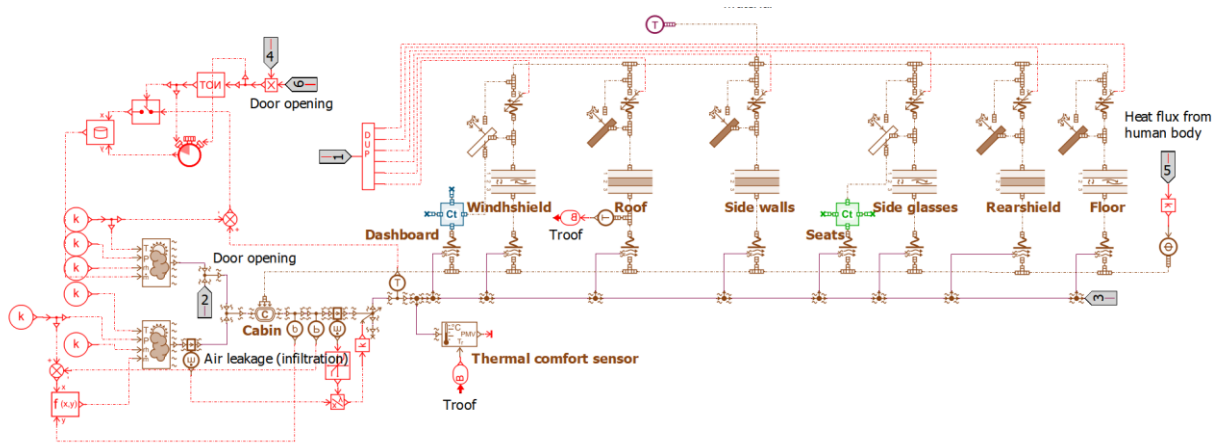


Figure 53. The cabin model in the simulation

Table 7. Dimensions of the Cabin

Cabin Length	11.467 m
Cabin Width	2.483 m
Cabin Height	2.343 m
Cabin Occupation Rate	~25 %
Cabin Volume	$11.467 \cdot 2.483 \cdot 2.343 \cdot (1-25\%) = 50.033 \text{ m}^3$
Cabin Cross Section	$2.483 \cdot 2.343 = 5.818 \text{ m}^2$

The cabin model is validated by a cabin cool-down experiment introduced in Section 4.4.2, in which a warm cabin exchange heat with a cold environment.

3.7.1 Interfaces

Six interfaces that could transfer heat between the cabin and the environment are modelled – windshield, roof, side walls, side glasses, rear shield (wall), and floor. The interfaces are thermal masses with different layers of materials and have convective energy exchange from both external and internal side. Additionally, solar radiation is taken into account, which is discussed in Section 3.7.5. Table 8 lists the details of each interface. The areas for each interface are measured from the 3D CAD file of the cabin showing in Figure 54. 3D CAD model of the cabin of e-Muuli, while the thickness of each layer is measured directly from the bus.

Table 8. Details for cabin interfaces with the environment

	Area (m^2)	Materials (out to in)	Thickness (out to in, mm)	Angle to horizontal β	Angle to north ζ
Windshield	3.053	Glass+Air+Glass	10 + 15 + 10	90°	270°
Roof	23.914	Aluminum+Foam+Interior	4 + 60 + 5	0°	0°
Side wall 1	8.591	Aluminum+Foam+Interior	4 + 50 + 5	90°	0°
Side wall 2	8.591	Aluminum+Foam+Interior	4 + 50 + 5	90°	180°
Side glass 1	10.904	Glass+Air+Glass	10 + 5 + 10	90°	0°
Side glass 2	10.904	Glass+Air+Glass	10 + 5 + 10	90°	180°
Rear shield	3.356	Aluminum+Foam+Interior	4 + 60 + 5	90°	90°
Floor*	8.128	Aluminum+Air+Interior	10 + 5 + 5	180°	0°

* only middle part of the floor is considered because left and right part the floor is well insulated.

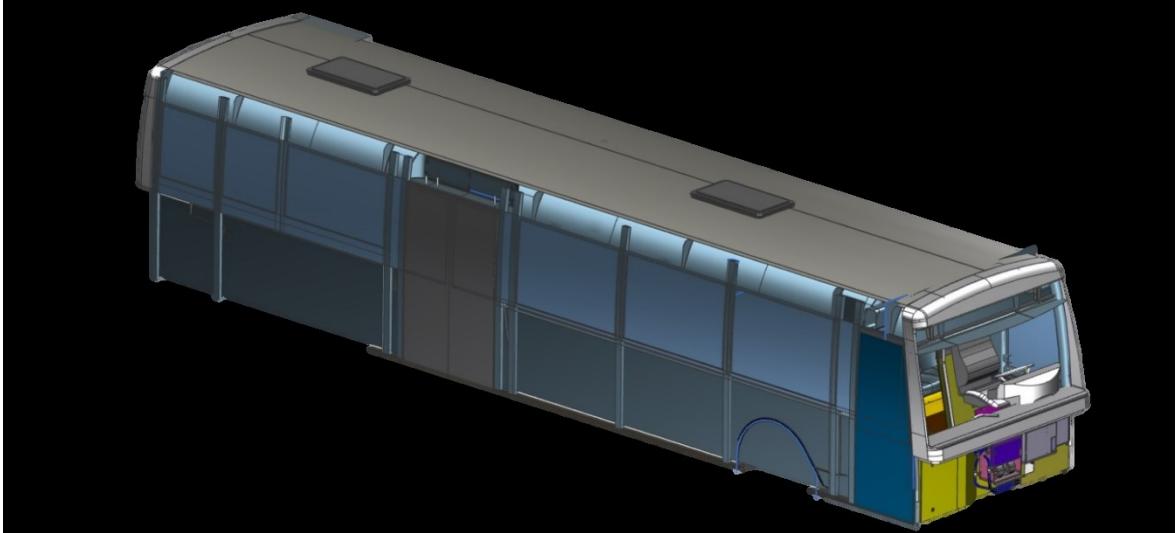


Figure 54. 3D CAD model of the cabin of e-Muuli

The angles β and ζ are defined for solar radiation. A visualization of a surface with its β and ζ angles are shown in Figure 55. Surface angles definition in the simulation (Siemens, 2019).

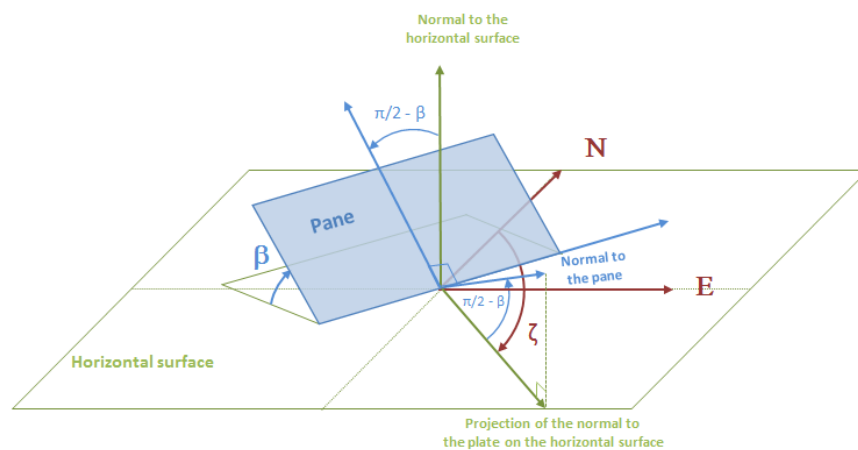


Figure 55. Surface angles definition in the simulation (Siemens, 2019)

3.7.2 Doors Opening Model

Compared with passenger cars, buses will open doors in a much higher frequency during operation. In cold/hot weather, the air that pours into the cabin through open doors will affect the thermal balance of the cabin, resulting in higher cabin heating/cooling demands. However, few researches have addressed the effects. To simulate the effects and evaluate the impacts on thermal simulation, a doors opening model, which simulates the air exchange through open doors, is built to the cabin model.

Figure 56. Net air flow through bus door CFD simulation data shows the CFD simulation data by Aku Karvinen. The data presents the air mass flow through opening bus doors with various internal-external temperature difference. In the CFD simulation, the initial cabin temperature was set to be 25°C, and ambient temperature varied from 30°C to -20°C. The air flow shown in the figure is the net flow through one bus door; the air flow into the cabin and out from the cabin is exactly half the magnitude of the data. It could be seen that air flow increases with increasing temperature difference.

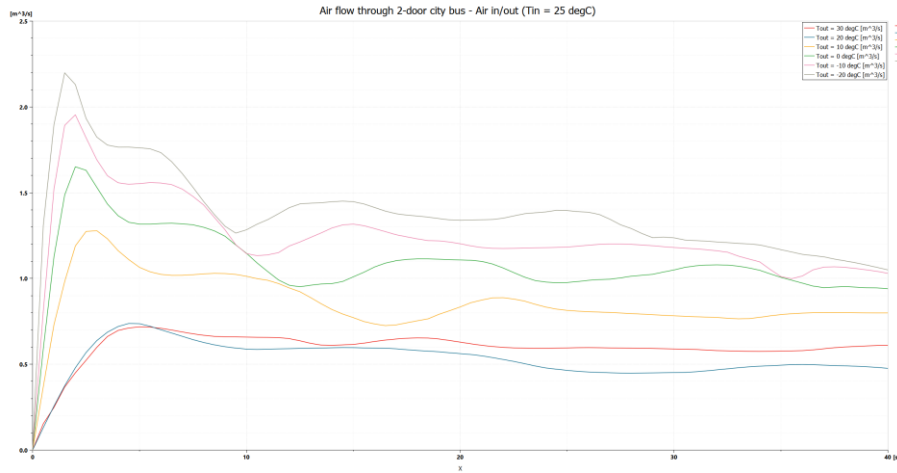


Figure 56. Net air flow through bus door CFD simulation data (Aku Karvinen, 2016)

Due to the limited amount of CFD simulation data, two assumptions are made in order to use the data in the cabin simulation model:

- The air flow through the cabin door is only related to the initial temperature difference. All the other factors, such as pressure and surface temperature, are ignored. For example, $T_{in} = 10^{\circ}\text{C}$ with $T_{out} = -5^{\circ}\text{C}$ will result in the same air flow as $T_{in} = 25^{\circ}\text{C}$ with $T_{out} = 10^{\circ}\text{C}$.
- It could be seen from the data that -5°C and 5°C temperature differences result in similar air flow. Therefore, it is assumed that the air flow is only related to the absolute value of the temperature difference. For example, $T_{in} = 10^{\circ}\text{C}$ with $T_{out} = -5^{\circ}\text{C}$ will result in the same air flow as $T_{in} = -5^{\circ}\text{C}$ with $T_{out} = 10^{\circ}\text{C}$.

With the two assumptions, a lookup table of air flow Q related to initial temperature difference ΔT_0 and doors opening time t is created:

$$Q = f(\Delta T_0, t) \quad (27)$$

Figure 57. Lookup table for air flow shows the 3D visualization of Q related to ΔT_0 and t .

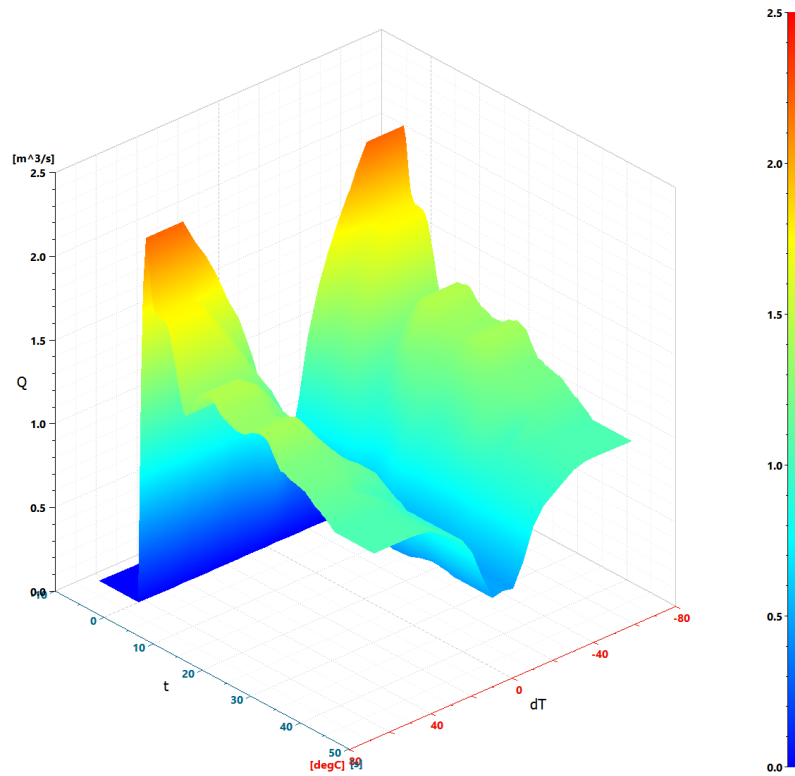


Figure 57. Lookup table for air flow used in the simulation

Figure 58. Air flow through open door model shows the doors opening model built into the cabin model, in which the lookup table $Q = f(\Delta T_0, t)$ is used. Every time the door is opened, the temperature difference ΔT_0 is measured, and the clock is triggered to measure t until the door is closed. ΔT_0 and t is then used in the lookup table to calculate the air flow, which is then used as the mass air flow rate of a moist air source of the cabin.

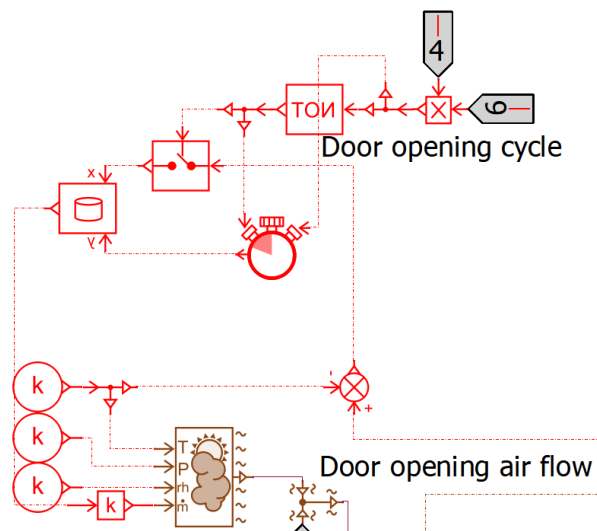


Figure 58. Air flow through open door model in the simulation

The effects of the doors opening model are discussed in Chapter 5, in which the battery electric bus model is simulated on real-life driving cycle with and without doors opening model. The results are discussed in Section 5.4.

3.7.3 Air Infiltration

The cabin of e-Muuli is not air-tight. Air can infiltrate through narrow openings such as gap around the door and holes on the floor. An air infiltration model is made to simulate the effects. It is assumed that the air flow through the narrow openings is turbulent, thus the orifice equation is used to calculate the infiltrated air flow (Liddament, 1986):

$$Q = C_d A \left[\frac{2}{\rho} \Delta p \right]^{\frac{1}{2}} \quad (28)$$

where Q is the air flow rate in m^3/s , C_d is discharge coefficient, ρ is air density in kg/m^3 , Δp is pressure difference across opening in Pa , and A is the area of opening in m^2 . In the model: $C_d = 0.64$, $\rho = 1.225 kg/m^3$, $A = 0.06 m^2$.

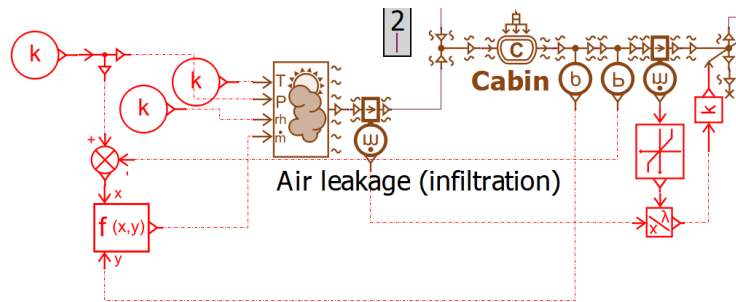


Figure 59. Air infiltration model in the simulation

3.7.4 Human Factor

Human passengers inside the cabin exchange heat with the environment in multiple ways. Human could release heat to the environment by convection with ambient air, radiation with surrounding surfaces, evaporation of sweat; human could also absorb heat from irradiation from high-temperature sources (Fiala, 1998). Additionally, environmental factors such as humidity, temperature, and solar radiation, as well as individual characteristics such as age, body weight, and sex could all affect the heat exchange between human and the environment (Havenith *et al.*, 1998).

For the purpose of the thesis, a simplified approach is taken – every human passenger inside the cabin is modelled as a heat source of an empirical value of $100 W$ (Brèque and Nemer, 2017).

3.7.5 Solar Effects

The solar effects to the bus are divided in two categories: solar radiation absorbed by the external surfaces of the cabin body and solar radiation going through the glasses and absorbed by the interior.

The solar radiation absorbed by a surface is calculated from the solar irradiance (in W/m^2), the angle of the sun, the angle and surface area of the surface, as well as the absorption factor of the surface. The solar irradiance is calculated by specifying the coordinate of the location and the time. The absorption factor for non-transparent surfaces is set to 0.9 because the external surfaces of e-Muuli are mostly white; the absorption factor for windshield and side windows are both set to 0.4 (Mitalas and Stephenson, 1962).

The angle of the sun is defined by solar azimuth α and altitude γ , which are represented in Figure 60. Solar angle definition in the simulation (Siemens, 2019).

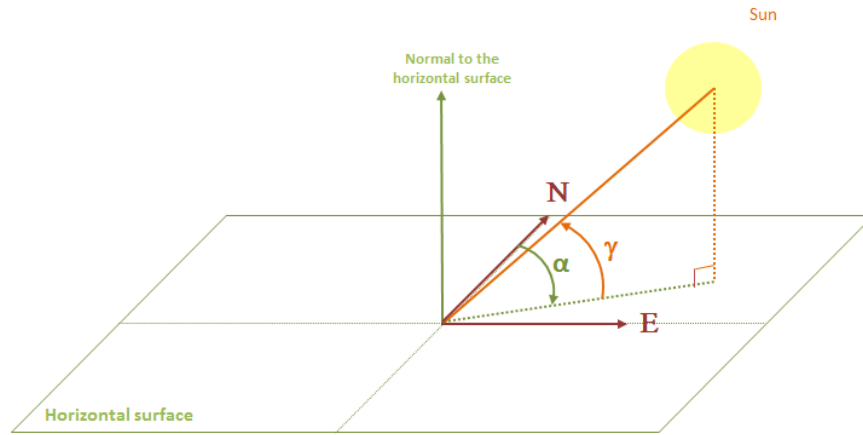


Figure 60. Solar angle definition in the simulation (Siemens, 2019)

Combined with the surface angle β and ζ introduced in Section 3.7.1, the incidence angle θ between sun ray and the normal to the surface is calculated. The cosine of θ is computed as follows:

$$\cos \theta = \sin \gamma \cdot \cos \beta + \cos \gamma \cdot \sin \beta \cdot \cos \delta \quad (29)$$

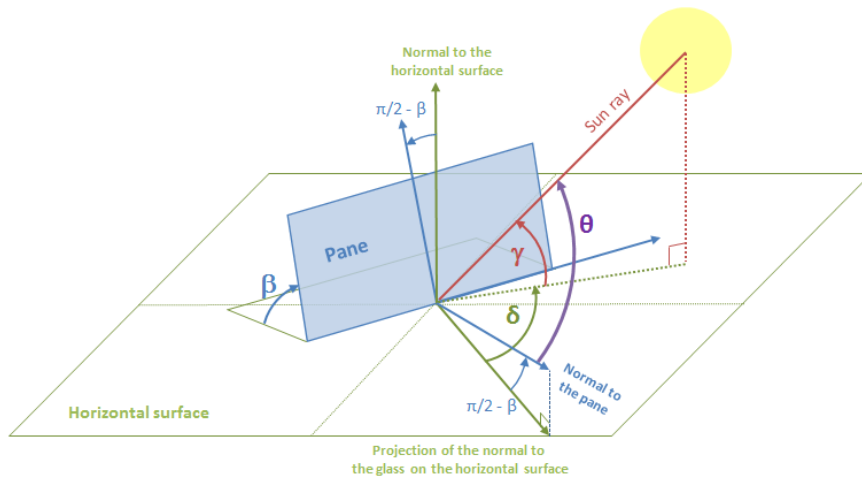


Figure 61. Incidence angle calculation in the simulation (Siemens, 2019)

Solar irradiance I (in W/m^2) is the power per unit area received from the sun to a certain geographical location. The solar irradiation power q_{solar} to a surface with area A is calculated as:

$$q_{solar} = I \cdot A \cdot \cos \theta \quad (30)$$

In many occasions, the solar power data is available in forms other than solar irradiance, such as solar illuminance E (in lx or lm/m^2), which represents the amount of sun light received by a unit area. In this case, the solar illuminance E need to be changed into solar irradiance I to be used in the simulation. Luminous efficacy K (in lm/W) is used to make the conversion between the two using the following equation.

$$I = \frac{E}{K} \quad (31)$$

Littlefair (1985) measured and calculated that the diffuse skylight average luminous efficacies range from 130 lm/W for clear skies and 110 lm/W for overcast skies; the global efficacies are around 105 lm/W for clear skies and average conditions. Lam and Li (1996) measured that the global efficacy under overcast skies range from 82 to 142 lm/W . In the thesis, $K = 105 \text{ lm/W}$ is used. To convert solar illuminance to solar irradiance,

$$I = \frac{E}{K} = 0.0095 \cdot \frac{W}{\text{lm}} \cdot E \quad (32)$$

The solar radiation absorbed by the interior is related to the properties of the glass and the volume of the interior materials that are exposed to the sun. Apart from the absorption factor, there is also a transmission factor which is set to 0.5 for windshield and side glasses (Mitalas and Stephenson, 1962). The interior is represented by the dashboard and the seats, the volume of which are 0.005845 m^3 and 0.31455 m^3 respectively.

3.8 Heating, Ventilation and Air Conditioning (HVAC) System

The HVAC simulation model is purposely built to simulate Eberspächer AC136 AE (all-electric) HP (heat pump) HVAC unit (AC136 AE HP). It is the key component in cabin thermal management. Several models and documents provided the data needed for modelling the system. Figure 62 shows the schematics of the HVAC system, in both cooling (air conditioning) and heating (heat pump) mode. Figure 63 shows the 3D CAD model of the unit. The 3D model only includes the case of the AC136 AE HP, while the detailed layout is further provided by the 2D CAD drawings of the HVAC system.

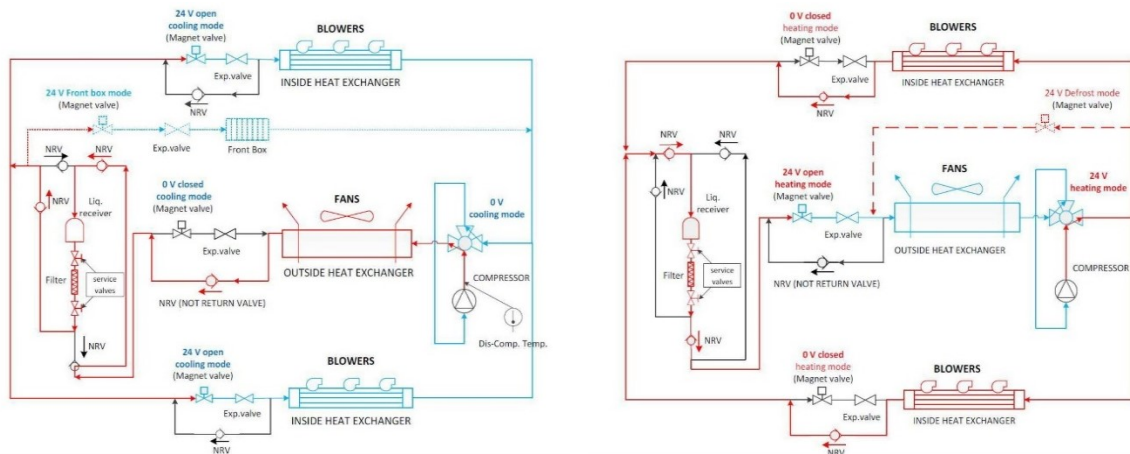


Figure 62. Schematics of AC136 AE HP cooling and heating mode (Eberspächer, 2019)

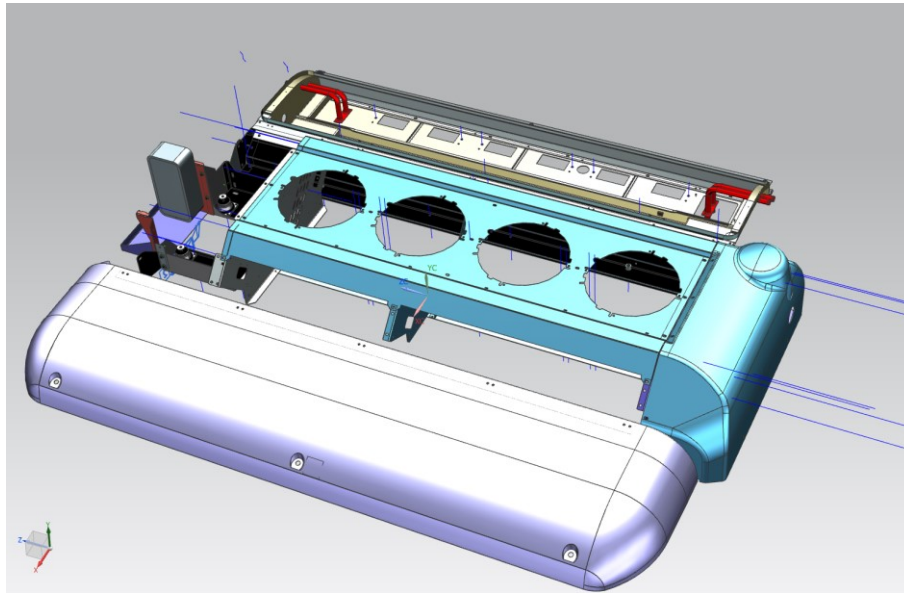


Figure 63. 3D CAD model for AC136 AE HP case

Additionally, the technical data of AC136 AE HP could be found on the website of Eberspächer (Eberspächer, 2019), which is listed in Table 9 below.

Table 9. Technical Data of AC136 AE HP (Eberspächer, 2019)

Technical Data	AC136 AE HP
Refrigerant	R134a
Nominal cooling performance (50/70 Hz)	20 / 22 kW
Max. cooling performance (50/70Hz)	26 / 29 kW
The nominal cooling performance was determined under the following conditions: exterior temperature 35 °C, interior temperature 27 °C. The max. cooling performance was determined under the following conditions: exterior temperature 35 °C, interior temperature 40 °C.	
Nominal heating performance (50/70 Hz)	11 / 13 kW
Max. heating performance (50/70 Hz)	18 / 22 kW
The nominal heating performance was determined under the following conditions: exterior temperature -5 °C, interior temperature 16 °C. The max. cooling performance was determined under the following conditions: exterior temperature 10 °C, interior temperature 20 °C.	
Heating performance, water convection	18 kW
Length * width * height	2590 * 2010 * 420 mm
Weight	299 kg
Evaporator air flow rate	6600 m ³ /h
Current draw at 24 VDC	88 A
Nominal power consumption, cooling, at 400 V AC (50/70 Hz)	4.8 / 7.1 kW
Max. power consumption, cooling, at 400 V AC (50/70 Hz)	5.4 / 8.6 kW
Nominal power consumption, heating, at 400 V AC (50/70 Hz)	2.4 / 3.3 kW
Max. power consumption, heating, at 400 V AC (50/70 Hz)	3.3 / 4.8 kW

The HVAC simulation model is shown in Figure 64. For a minimalistic look, the system is setup as a ‘super-component’ which has an icon as Figure 65.

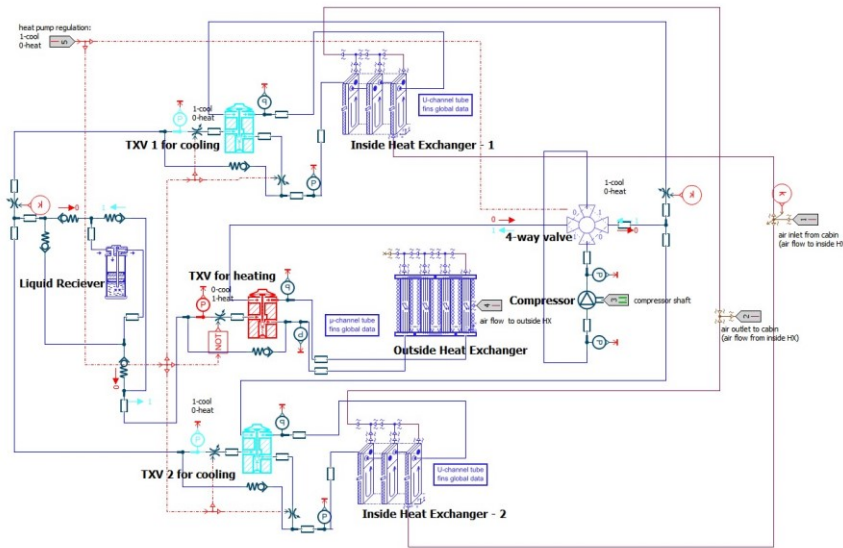


Figure 64. HVAC system model in the simulation

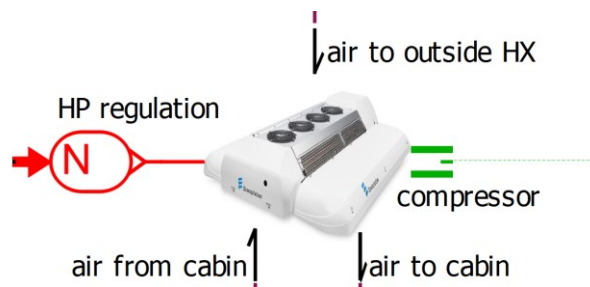


Figure 65. HVAC system super-component icon in the simulation

The HVAC model is a heat pump system that uses a four-way valve to direct flow to different directions in cooling and heating mode. The system includes a compressor, an outside heat exchanger with a corresponding thermal expansion valve, two inside heat exchangers with two corresponding thermal expansion valves, a four-way valve, several magnetic valves, check valves, a liquid receiver/dryer, and some pipelines and sensors. The controller of the HVAC unit is separated from the HVAC model itself and is integrated into the thermal management controller, which is discussed in section 3.9.

The characterization of the HVAC system, including the temperature, compressor, and blower characteristics are investigated in Section 4.1. The heat pump mode is further tested and validated by a heat pump test in Section 4.4.3.

3.8.1 Compressor

The compressor used in the model is a fixed displacement two-phase flow compressor/pump. The parameters of the compressor are set as Figure 66.

Title	Value	Unit	Name
index of fluid		1	fi
input data out of range	extreme value		mode
discontinuity handling	active		disc
compatibility with stop and start	yes		sands
coefficient definition	no		CoeffDef
flow rate calculation	displacement		flowRateCal
displacement	200	cm ³	disp
minimum absolute mass flow rate	0.0001	kg/s	minflow
▾ □ efficiencies			
inputs for efficiency's definition	tau, N[rev/min]		ParamNum
filename or expression for volumetric efficiency = f(tau, N[rev/min], (X1), (X2))		0.6	volEff
filename or expression for isentropic efficiency = f(tau, N[rev/min], (X1), (X2))		0.75	isEff
filename or expression for mechanical efficiency = f(tau, N[rev/min], (X1), (X2))		0.9	mecEff

Figure 66. Parameters for the compressor model in the simulation

The volumetric efficiency is used to compute the mass flow rate as follows:

$$dm_2 = \eta_v \cdot \rho_{suc} \cdot N \cdot disp \quad (33)$$

where η_v is volumetric efficiency, ρ_{suc} is suction density, N is the rotary speed of the compressor, $disp$ is the displacement of the compressor pump.

The isentropic efficiency is used to compute the enthalpy increase through the compressor. The isentropic efficiency can be expressed as follows:

$$\eta_{is} = \frac{h_{dis} - h_s}{h_d - h_s} \quad (34)$$

where η_{is} is isentropic efficiency, h_{dis} isentropic discharge specific enthalpy, h_s is suction specific enthalpy, h_d is discharge specific enthalpy.

Therefore, the enthalpy increase is calculated as follows:

$$h_{inc} = h_d - h_s = \frac{h_{dis} - h_s}{\eta_{is}} \quad (35)$$

The mechanical efficiency is used to compute the torque and can be expressed as follows:

$$\eta_{mech} = \frac{dm_2 \cdot h_{inc}}{\tau_3 \cdot N} \quad (36)$$

where η_{mech} is mechanical efficiency, dm_2 is compressor/pump mass flow rate, h_{inc} is enthalpy increase, τ_3 is torque, N is compressor/pump rotary speed.

3.8.2 Heat Exchangers

Both the external and internal heat exchangers are fins and tubes type. There are two external heat exchangers (EHX) in parallel, but sharing one thermal expansion valve. Each of them features 7 channels for refrigerant to pass through. 2 out of the 7 channels circulate the heat exchanger 10 times, while the other 5 channels circulate 8 times. The details of the external heat exchangers could be seen in Table 10 and Figure 67.

Table 10. Details of the external heat exchanger of Eberspächer AC136 AE HP

Numbers of heat exchangers	2
Type of arrangement	Staggered
Number of tube banks per exchanger	4

Number of tubes per bank	15
Bank pitch [mm]	20
Tube pitch [mm]	25
Tube length [mm]	1600
Tube inner diameter [mm]	8

There are two internal heat exchangers (IHX) in parallel, located at each side of the bus. Each of them features 7 channels. All of the channels circulate 4 times. The details of the internal heat exchangers could be seen in Table 11 and Figure 68.

Table 11. Details of the internal heat exchanger of Eberspächer AC136 AE HP.

Numbers of heat exchangers	2
Type of arrangement	Staggered
Number of tube banks per exchanger	4
Number of tubes per bank	7
Bank pitch [mm]	21.5
Tube pitch [mm]	25
Tube length [mm]	1380
Tube inner diameter [mm]	8

AMESim offers the way to simulate fins and tubes heat exchangers in detail, which is further discussed below as method (a). There is also another method in which EHXs and IHXs are modelled as several basic heat exchangers, which is further discussed below as method (b). In comparison, method (a) prevails in terms of accuracy, but method (b) is eventually chosen for much less computational efforts.

(a) A detailed model of fins and tubes heat exchanger

This method utilizes the fins and tubes heat exchanger designer app in AMESim. It is a complete user interface to set connections between tubes and launch the automatic sketch generation of the heat exchanger. Compared with the method (b), a more detailed simulation could be achieved, including the heat exchange correlations at fins level (moist air) and at tubes level (refrigerant), and the pressure drop in the tubes and the bends. The downside of using this method is that this method is computationally heavy since a detailed submodel is created by the designer app containing hundreds of components, compared with one single component in method (b). The simulation time is dramatically increased and the method could cause regular crashes of the software.

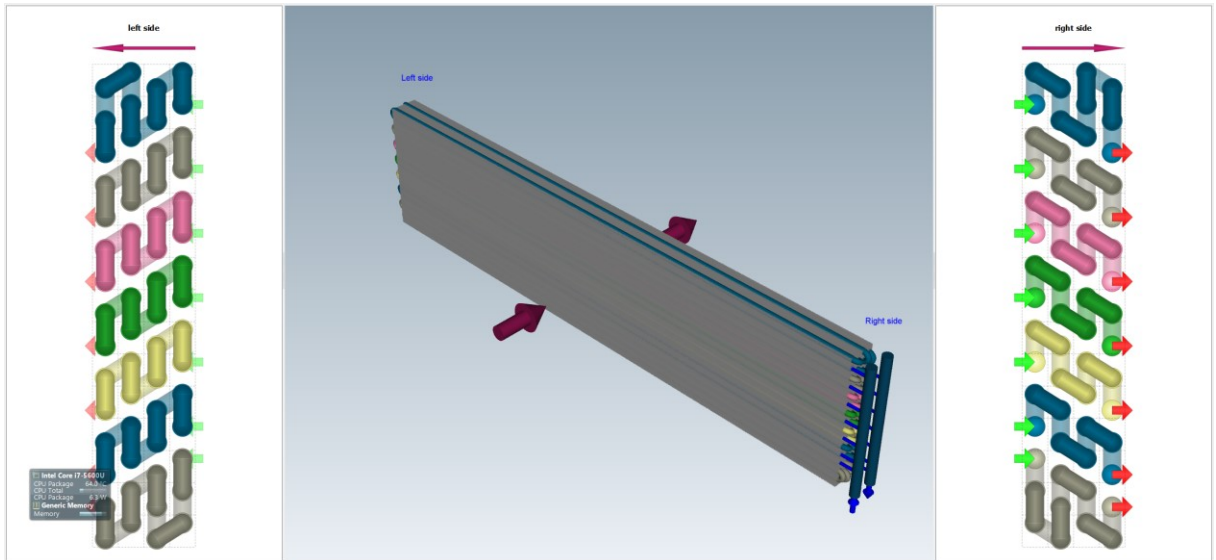


Figure 67. Detailed model of an external heat exchanger in the simulation

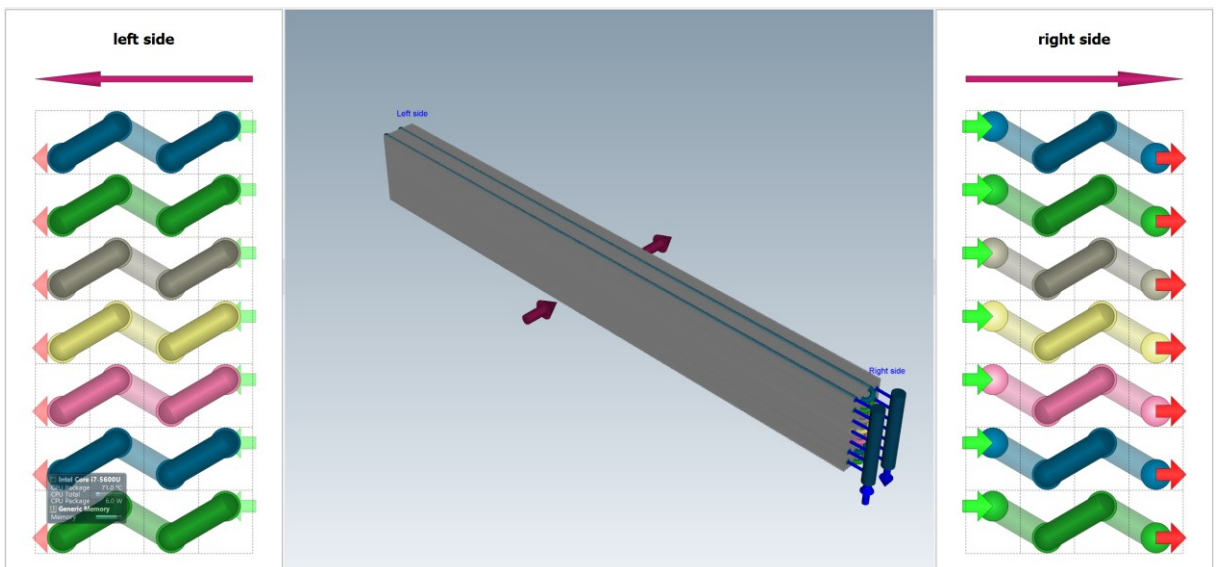
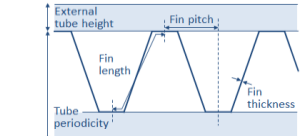


Figure 68. Detailed model of an internal heat exchanger in the simulation

(b) A general model of heat exchangers

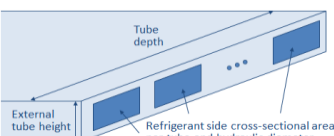
In this method, EHX is modelled as eight microchannel tube and fins heat exchangers arranged in series; IHX is modelled as two U-channel plate and fins heat exchangers arranged in series, with left and right IHX in parallel. The settings for the model follow the parameters of the heat exchangers of AC136 AE HP; more details are shown in Figure 69 - Figure 72.

Parameters for external side



Fin pitch [mm]	1.2
Fin thickness [mm]	0.1
Fin length [mm]	16.714
Tube periodicity [mm]	25
External tube height [mm]	10

Parameters for internal side



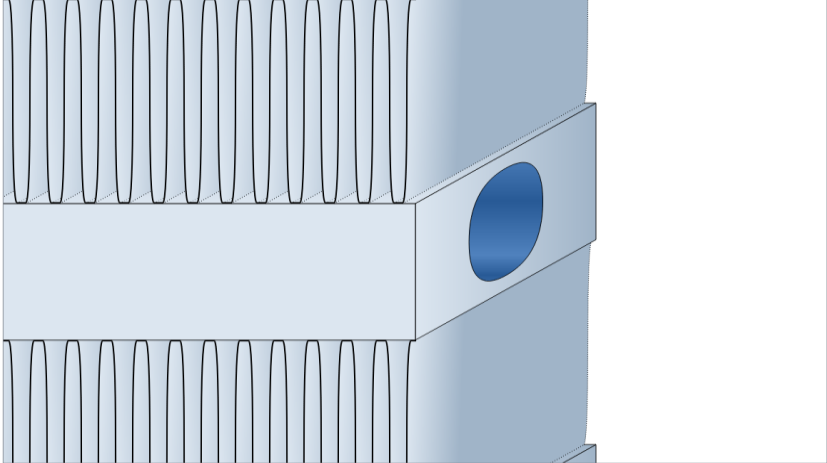
Tube depth [mm]	20
External tube height [mm]	10
Refrigerant cross sectional area per tube [mm**2]	50.3
Refrigerant hydraulic diameter [mm]	8

Indicative scaled drawing Global heat exchanger geometry

The parameters and the drawing below are set for convenience only. There is no direct link with the simulation model.

External side: type of drawing for fins
 Internal side: type of drawing for micro channels
 Internal side: orientation of micro channels
 Internal side: number of micro channels (max=1)

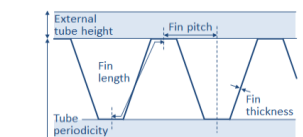
Arc	▼
Ellipse	▼
Horizontal	▼
1	↕



Drawing values for fins	
Fin hydraulic diameter as drawn [mm]	1.823
Fin length as drawn [mm]	16.714
Drawing values for micro channels	
Height of micro channels as drawn [mm]	7.856
Width of micro channels as drawn [mm]	8.152
Thickness between box edge and micro channels (along width) [mm]	5.924
Thickness between box edge and micro channels (along height) [mm]	1.072

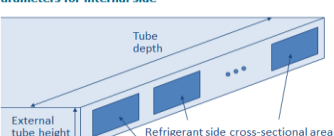
Figure 69. Indicative scaled drawing settings for external heat exchangers in the simulation

Parameters for external side



Fin pitch [mm]	1.2
Fin thickness [mm]	0.1
Fin length [mm]	16.714
Tube periodicity [mm]	25
External tube height [mm]	10

Parameters for internal side



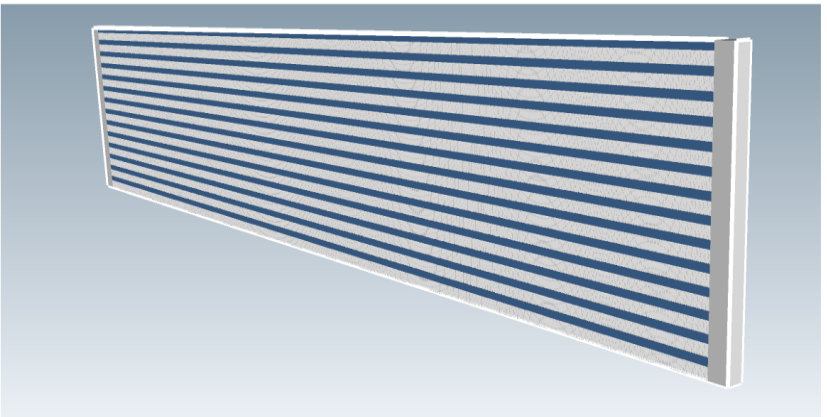
Tube depth [mm]	20
External tube height [mm]	10
Refrigerant cross sectional area per tube [mm**2]	50.3
Refrigerant hydraulic diameter [mm]	8

Indicative scaled drawing Global heat exchanger geometry

Tube width [mm] **1600**
 Collector cross sectional area [mm**2] **500**

The parameters and the drawing below are set for convenience only. There is no direct link with the simulation model.

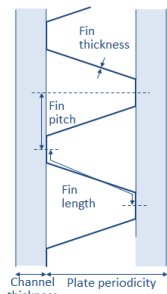
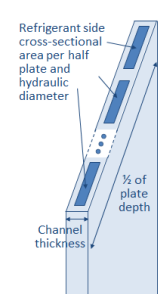
Total number of passes **1**
 Number of tubes for each pass (top to down) **14**



General values			
Core width [mm]	1600.000	Solid total volume [mm**3]	3977269.333
Core height [mm]	350.000	Solid (alu@20degC) total mass [kg]	10.747
Core depth [mm]	20.000		
External side values			
Air frontal area [mm**2]	560000.000	Air cross-sectional area [mm**2]	304800.533
Air hydraulic diameter [mm]	1.823	Air convective exchange area [mm**2]	13375786.66
Internal side values			
Refrigerant hydraulic diameter [mm]	8.000	Refrigerant convective exchange area [mm**2]	563360.000
Refrigerant all channels volume [mm**3]	1126720.000	Refrigerant (one) collector volume [mm**3]	175000.000

Figure 70. Global heat exchanger geometry settings for external heat exchangers in the simulation

Parameters

Fin pitch [mm]	1.6
Fin thickness [mm]	0.18
Fin length [mm]	16.755
Plate periodicity [mm]	25
External channel thickness [mm]	10

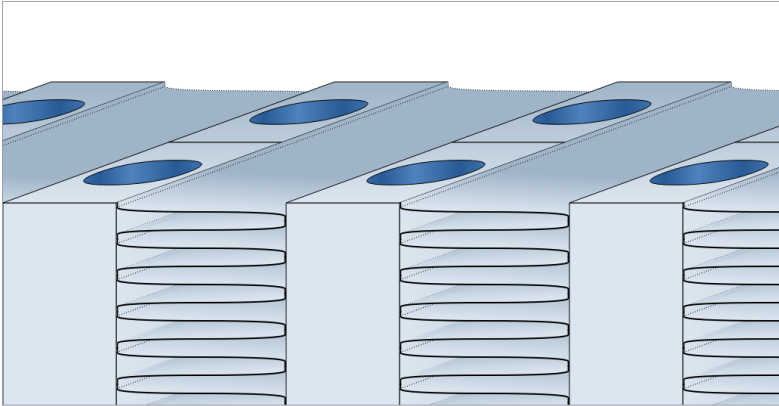
Plate depth [mm]	40
External channel thickness [mm]	10
Refrigerant cross sectional area per half plate [mm**2]	50.3
Refrigerant hydraulic diameter [mm]	8

Indicative scaled drawing Global heat exchanger geometry

The parameters and the drawing below are set for convenience only. There is no direct link with the simulation model.

External side: type of drawing for fins
Internal side: type of drawing for micro channels
Internal side: orientation of micro channels
Internal side: number of micro channels (max=1)

Arc
 Ellipse
 Horizontal
 1



Drawing values for fins

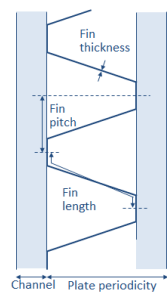
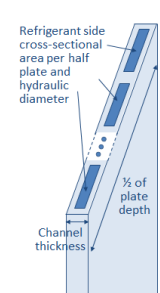
Fin hydraulic diameter as drawn [mm]	2.286
Fin length as drawn [mm]	16.755

Drawing values for micro channels

Height of micro channels as drawn [mm]	7.856
Width of micro channels as drawn [mm]	8.152
Thickness between box edge and micro channels (along width) [mm]	5.924
Thickness between box edge and micro channels (along height) [mm]	1.072

Figure 71. Indicative scaled drawing settings for internal heat exchangers in the simulation

Parameters

Fin pitch [mm]	1.6
Fin thickness [mm]	0.18
Fin length [mm]	16.755
Plate periodicity [mm]	25
External channel thickness [mm]	10

Plate depth [mm]	40
External channel thickness [mm]	10
Refrigerant cross sectional area per half plate [mm**2]	50.3
Refrigerant hydraulic diameter [mm]	8

Indicative scaled drawing Global heat exchanger geometry

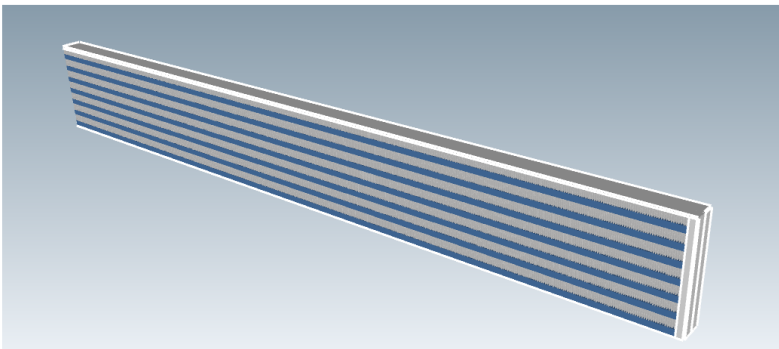
Plate height [mm] **1380**

Collector cross sectional area [mm**2] **200**

The parameters and the drawing below are set for convenience only. There is no direct link with the simulation model.

Total number of passes **1**

Number of plates for each pass (right to left) **7**



General values

Core width [mm]	175.000	Solid total volume [mm**3]	3620543.850
Core height [mm]	1380.000	Solid (alu@20degC) total mass [kg]	9.783
Core depth [mm]	40.000		

External side values

Air frontal area [mm**2]	241500.000	Air cross-sectional area [mm**2]	126691.504
Air hydraulic diameter [mm]	2.286	Air convective exchange area [mm**2]	8865465.000

Internal side values

Refrigerant hydraulic diameter [mm]	8.000	Refrigerant convective exchange area [mm**2]	242949.000
Refrigerant all channels volume [mm**3]	971796.000	Refrigerant (one) collector volume [mm**3]	35000.000

Figure 72. Global heat exchanger geometry settings for internal heat exchangers in the simulation

For both of the EHX and IHX, the convective heat exchange between the refrigerant and the heat exchanger wall is calculated as follows for each refrigerant cell:

$$\phi_{int,i} = h_{c,i} \cdot S_i \cdot (T_{ref,i} - T_{wall,i}) \quad (37)$$

where $\phi_{int,i}$ is the internal heat flux at the cell level, $h_{c,i}$ is the convective heat exchange coefficient at the cell level, S_i is the internal exchange surface at the cell level, $T_{ref,i}$ is the refrigerant temperature at cell level, $T_{wall,i}$ is the wall temperature at cell level.

For external heat exchange, moist air conditions are applied on each cell of the heat exchanger. External heat transfer will lead to new moist air property for each cell. The moist air obtained for each cell is mixed to give the global outgoing moist air flow.

$$\phi_{ext} = \sum_i \phi_{ext,i} \quad (38)$$

The calculation of the wall temperatures depends on the internal and external heat exchanges for each cell of the component. The wall temperatures are state variables and are computed from their time derivatives as follows:

$$\frac{dT_{wall,i}}{dt} = \frac{\phi_{int,i} + \phi_{ext,i}}{m_i \cdot C_{p,i}} \quad (39)$$

where $T_{wall,i}$ is the wall temperature at the cell level, $\phi_{int,i}$ is the internal heat flux at the cell level, $\phi_{ext,i}$ is the external heat flux at the cell level, m_i is the mass of material involved at the cell level, $C_{p,i}$ is the wall material specific heat at the cell level.

3.8.3 Thermal Expansion Valve

There are a total number of three thermal expansion valves (TXV); each one of them is in front of a heat exchanger. In the model, all of the TXVs are configured as H-valve, or block valve. In heating mode, the external heat exchanger is used as an evaporator. Therefore, the TXV for EHX is in use, while two TXVs for IHXs are bypassed. The parameters for the TXV for EHX is shown in Figure 73.

Title	Value	Unit	Name
⊕ bulb temperature	10	degC	tbulb
index of fluid	1		fi
maximum hydraulic diameter	1	mm	hdmax
critical flow number	10000	null	lamc
maximum mass flow rate at reference conditions	0.5	kg/s	dmmax
m coefficient	1	null	mc
bulb saturation pressure at 0 degC (p0)	2.8	barA	p0
bulb saturation pressure at 10 degC (p10)	4.5	barA	p10
reference pressure (pref)	5	barA	pref
valve opening temperature at p0	0	degC	top
valve full-opening temperature at p0	20	degC	tfo
reference subcooling	5	degC	scref
time constant	5	s	tau

Figure 73. Parameters for the thermal expansion valve for an external heat exchanger in the simulation

The TXV is defined using the 4-quadrant diagram, which has been discussed in Section 2.2. In the model, the bulb saturation curve shown in quadrant 1 is simplified into a straight line which is defined by two pressure points: P_0 = Pressure of the bulb at 0°C, P_{10} = Pressure of the bulb at 10°C. The bulb pressure could be calculated as:

$$P_B = P_0 + \frac{T_E}{10} (P_{10} - P_0) \quad (40)$$

where T_E is the evaporator outlet temperature and P_B is the bulb pressure.

The opening of the valve x is given by:

$$x = \frac{h}{h_{max}} = \frac{T_E - T_{OP}}{T_{CL} - T_{OP}} + \frac{10(P_0 - P_E)}{P_{10} - P_0} \times \frac{1}{T_{CL} - T_{OP}} \quad (41)$$

where T_{OP} is the valve opening temperature at P_E (pressure at evaporator outlet) = P_0 , and T_{CL} is the temperature of full opening at $P_E = P_0$.

The balance of the rod can be written as follows:

$$h = \frac{A}{k} (P_B - P_E) - l_0 \quad (42)$$

where $A = \frac{\pi \cdot D_h^2}{4}$ with D_h the hydraulic diameter of the TXV, k is stiffness of the spring, l_0 the length of the spring with no load, h is the displacement of the rod.

3.8.4 Blower and Fan

According to the data for Eberspächer AC136 AE HP in Table 9, the evaporator air flow rate is $6600 \text{ m}^3/\text{h}$. This could be understood as the blower air flow. Assuming the air density $\rho = 1.225 \text{ kg/m}^3$, the mass flow rate for the blower is set to be:

$$Q_{m_{blower,max}} = \frac{6600 \cdot 1.225}{3600} \text{ kg/s} = 2.2458 \text{ kg/s}$$

There is no data regarding the power consumption of the blower in the data from Eberspächer. It is known that there are 6 blowers module installed, with 3 on each side of the bus, so the max airflow for each unit is $1100 \text{ m}^3/\text{h}$. Also considering the voltage and the installation size of the blower, a similar blower product, Tonada Konvekta H11-002-206 EC blower 24V (Tonada, 2019a), is selected as reference. Therefore, the power consumption at maximum load is:

$$P_{blower,max} = 6 \cdot 24V \cdot 9.7A = 1396.8 \text{ W}$$

There are 5 levels of air speed for the blower, the mass flow rate for level k ($1 \leq k \leq 5$) is set to be:

$$Q_{m_{blower,k}} = \sqrt{\frac{k}{5}} \cdot Q_{m_{blower,max}} \quad (43)$$

The power consumption is set under the same rule.

There is also no data regarding the top fan for external heat exchanger. It is known from CAD drawings that there are 4 EHX fans with a diameter of less than 320 mm . Also considering the voltage, a similar product, Tonada SPAL VA89-BBL300-94A EC fan 24V 305mm (Tonada, 2019), is selected as reference. Therefore, the max mass flow rate of the fan is set to be:

$$Q_{m_{fan,max}} = \frac{2760 \cdot 4 \cdot 1.225}{3600} \text{ kg/s} = 3.757 \text{ kg/s}$$

The power consumption at maximum load is:

$$P_{fan,max} = 4 \cdot 24V \cdot 7.3A = 700.8 \text{ W}$$

Currently, there is no speed controlling method utilized for the fans. The fans are at the maximum speed once they are on.

3.9 Thermal Management Controller

The thermal management controller (TMC) consists of 3 parts which control HVAC, battery cooling, powertrain cooling respectively. The control scheme diagram is shown in Figure 75. Figure 74 shows the external look of the thermal energy controller in the model.

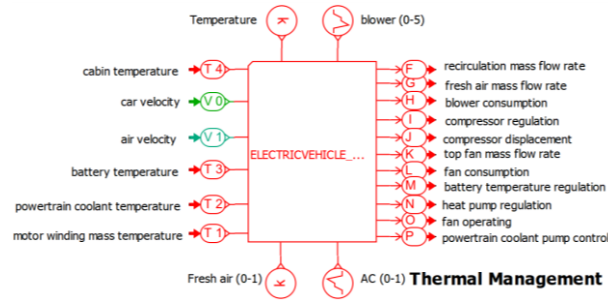


Figure 74. Thermal management controller model in the simulation

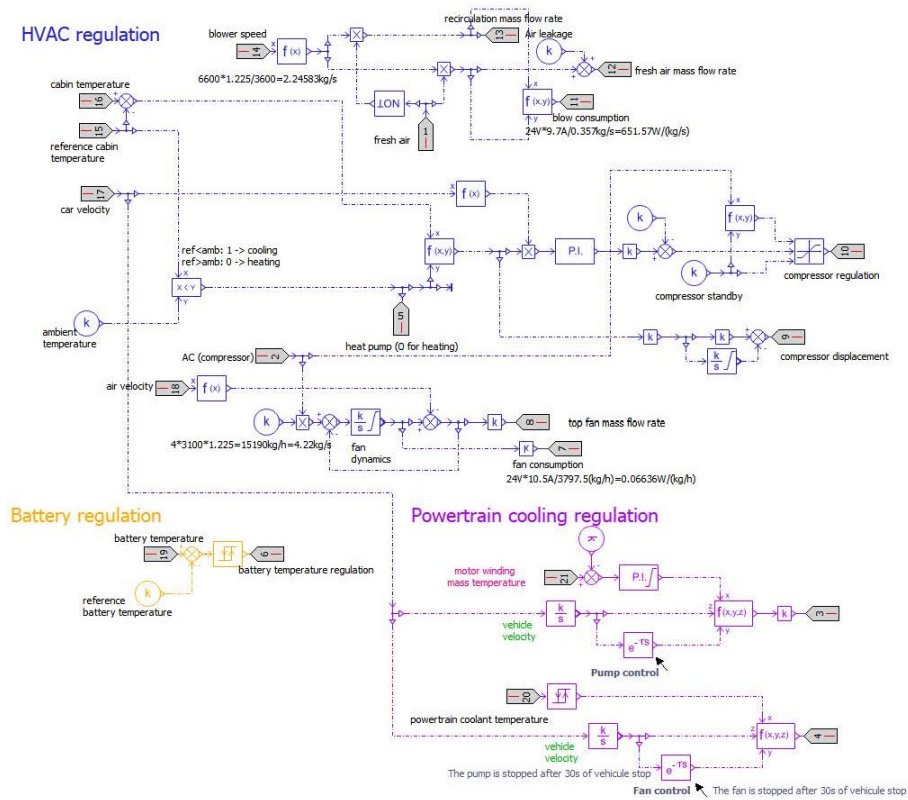


Figure 75. Thermal management controller control scheme diagram in the simulation

There are 6 system inputs, 4 control inputs, and 11 outputs for the TMC, all of which are listed in Table 12.

Table 12. Inputs and outputs of the thermal management controller in the simulation

Name	Remarks
------	---------

System inputs	Cabin temperature	Cabin temperature from cabin sensor
	Car velocity	Car velocity from powertrain sensor
	Air velocity	Air velocity from an external sensor
	Battery temperature	Battery cell temperature
	Powertrain coolant temperature	Coolant temperature before pump
	Motor winding temperature	Motor stator temperature
Control inputs	Cabin target temperature	The target temperature for HVAC
	Blower control	5 levels (1 - 5) and off (0)
	Fresh air control	On (1) and off (0)
	AC control	On (1) and off (0)
Outputs	Recirculation mass flow rate	Controls blower recirculation
	Fresh air mass flow rate	Controls blower fresh air intake
	Blower consumption	Indicates blower power consumption
	Compressor regulation	Control compressor inverter
	Compressor displacement	Alternative control for compressor
	Top fan mass flow rate	Controls EHX fan (top fan)
	Fan consumption	Indicates top fan power consumption
	Battery temperature regulation	Controls air flow to the battery pack
	Heat pump regulation	Controls heat pump, heating mode (0) and cooling mode (1)
	(Radiator) fan operating regulation	Controls radiator fan in coolant loop
Powertrain coolant pump control	Controls pump in coolant loop	

4 Model Characterization and Validation

This chapter discusses the characteristics of the simulations model and the validation of the simulation model by the experiments carried out on e-Muuli. The characteristics of the HVAC system and the powertrain cooling loops are examined. The model is further validated by:

- The dynamometer experiment, which validates the powertrain simulation model.
- The temperature experiment, which include:
 - The cabin cool-down test, which validates the cabin simulation model.
 - The heat pump test, which validates the HVAC (heat pump mode) simulation model.

4.1 HVAC Characterization

4.1.1 Temperature Characteristics

As discussed in Section 2.2.1, both internal and external heat exchangers transfer heat between air and liquid (refrigerant). Therefore, the ambient and cabin temperature could affect the performance of the HVAC. In this section, the temperature characteristics of HVAC are investigated by manually set ambient and cabin temperature to various levels.

(a) Cooling

The cooling (air conditioning) mode is tested with a batch of simulation runs with different ambient temperature from 10°C to 50°C. The initial cabin temperature is set by $T_{cabin} = T_{ambient}$. The compressor, blower, and top fan are all set to run at full speed. The air recirculation is turned off, and fresh air intake is turned on.

Figure 76 shows the pressure-enthalpy diagrams (PH diagrams) of the vapour compression cycle in different ambient temperatures. Figure 77 presents the coefficient of performance (COP) of the HVAC in cooling mode. It is calculated as:

$$COP_{cooling} = \frac{|Q_{IHX}|}{W} \quad (44)$$

where Q_{IHX} is the thermal energy removed from the internal heat exchanger, and W is the work required by the system, which includes compressor power, blower power, and top fan power. Figure 77 also shows the cooling power \dot{Q}_{IHX} and total power consumption \dot{W} of the HVAC system.

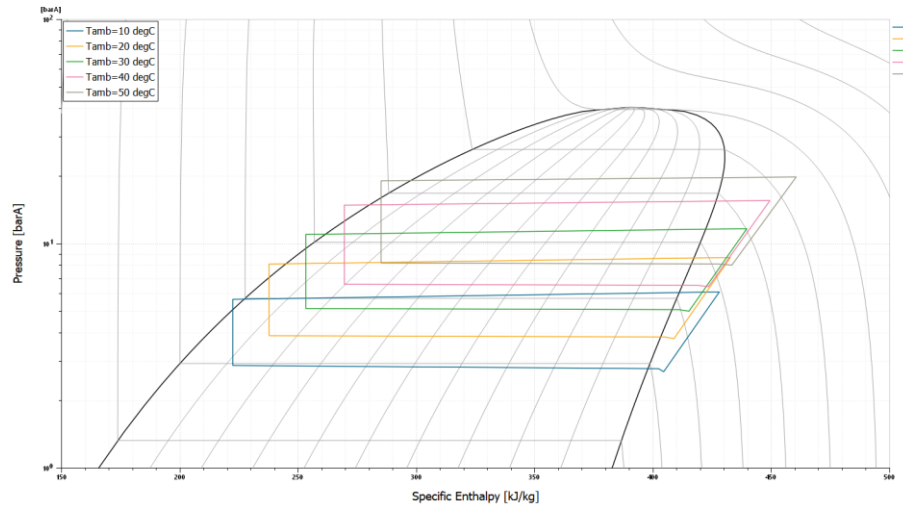


Figure 76. Simulation results - PH diagram of the vapour compression cycle in cooling mode in various ambient temperatures

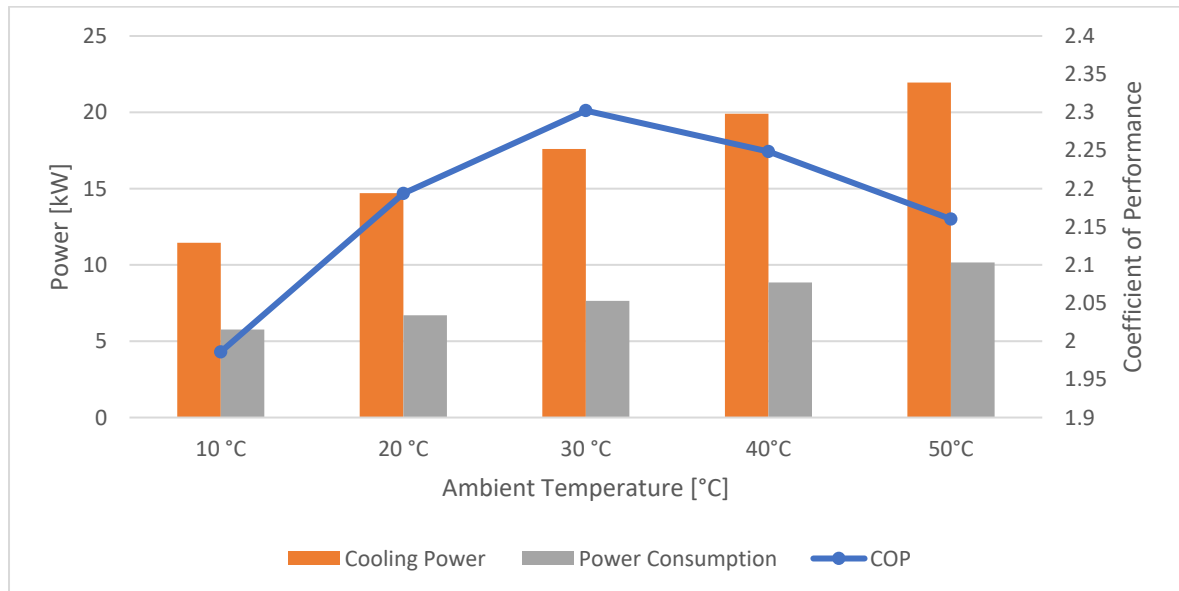


Figure 77. Simulation results - Performance curve of HVAC cooling mode in various ambient temperatures

It could be seen from the PH diagram that the operating pressure will increase significantly with the increase of T_{amb} . It could be seen from the Figure 77 that the both cooling power and power consumption increase with T_{amb} . However, the highest efficiency is achieved at around $T_{amb} = 28^{\circ}\text{C}$.

(b) Heating

The heating (heat pump) mode is tested with a batch of simulation runs with different ambient temperature from -20°C to 10°C . The initial cabin temperature is set by $T_{cabin} = T_{ambient}$. The compressor, blower, and top fan are all set to run at full speed. The air recirculation is turned off, and fresh air intake is turned on. In heating mode, the refrigerant is pre-heated to 20°C to improve system stability.

Figure 78 shows the pressure-enthalpy diagrams (PH diagrams) of the vapour compression cycle in different ambient temperatures. Figure 79 presents the coefficient of performance (COP) of the HVAC in heating mode. It is calculated as:

$$COP_{cooling} = \frac{|Q_{IHX}|}{W} \quad (45)$$

where Q_{IHX} is the thermal energy supplied to the internal heat exchanger, and W is work required by the system, which includes compressor power, blower power, and top fan power. Figure 79 also shows the heating power \dot{Q}_{IHX} and the total power consumption \dot{W} of the HVAC system.

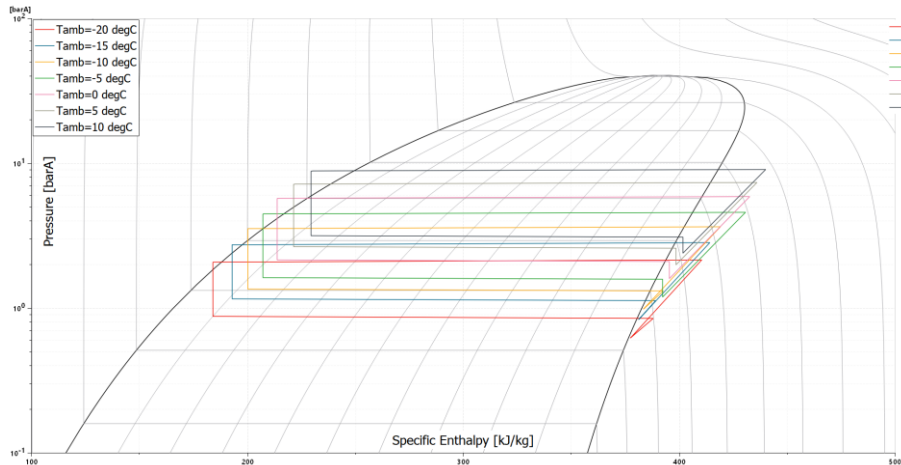


Figure 78. Simulation results - PH diagram of the vapour compression cycle in heating mode in various ambient temperatures

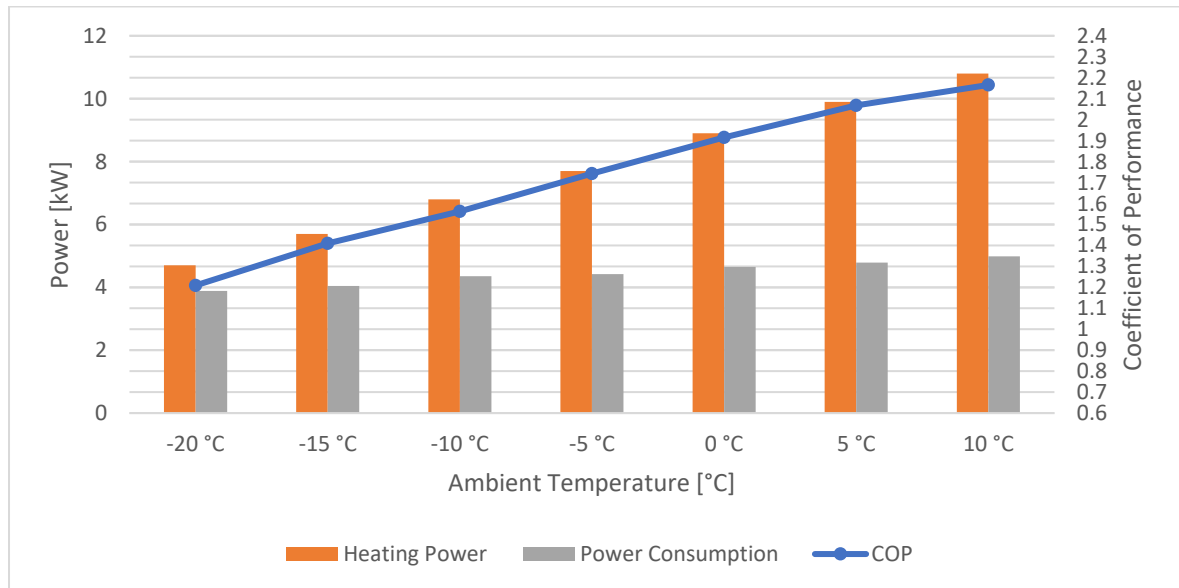


Figure 79. Simulation results - Performance curve of HVAC heat pump mode in various ambient temperatures

It could be seen from the PH diagram that the system operating temperature drops significantly with the decrease of T_{amb} . It could be seen from Figure 79 that the heating efficiency as well as heating power and power consumption decrease when T_{amb} decreases. From the tendency, we could speculate that, when the ambient temperature T_{amb} drops beyond a certain temperature, the COP of the heat pump could drop below 1, in which case

the heat pump starts to lose competitiveness regarding efficiency compared with resistive heating, since some PTC heater could achieve a minimum efficiency of 93% (Jeong and Lee, 2015).

4.1.2 Compressor Characteristics

As discussed in section 3.9, the compressor speed is controlled by the ‘compressor regulation’ command (0-1) from the thermal management controller, while 1 will result in maximum compressor speed. In this section, the speed of the compressor is manually set in 5 levels from 0.2 to 1 in order to demonstrate the characteristics of HVAC’s compressor. During the tests, heating (heat pump) mode is used and the ambient and cabin temperatures are both set to -10°C . Blower speed is set to maximum. Air circulation is turned off and the fresh air intake is turned on.

Figure 80 shows the pressure-enthalpy diagrams (PH diagrams) of the vapour compression cycle with different compressor speeds. Figure 81 presents the coefficient of performance (COP) as well as heating power and power consumption of the HVAC.

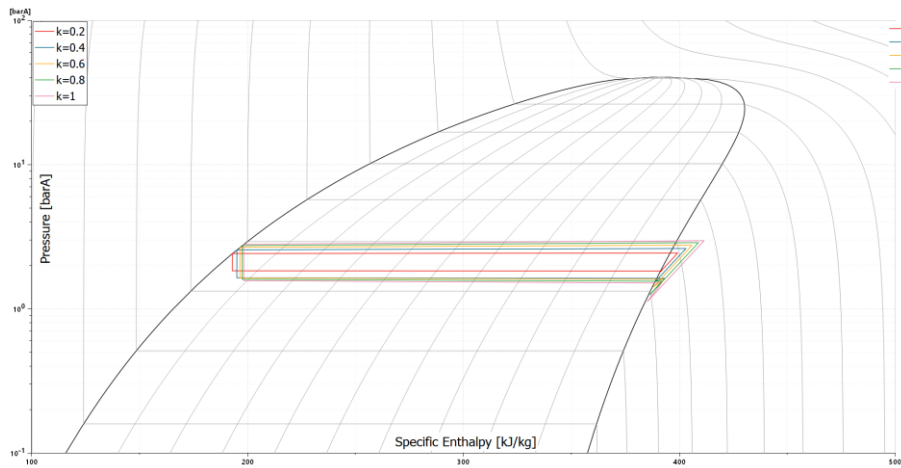


Figure 80. Simulation results - PH diagram of the vapour compression cycle with various compressor speeds

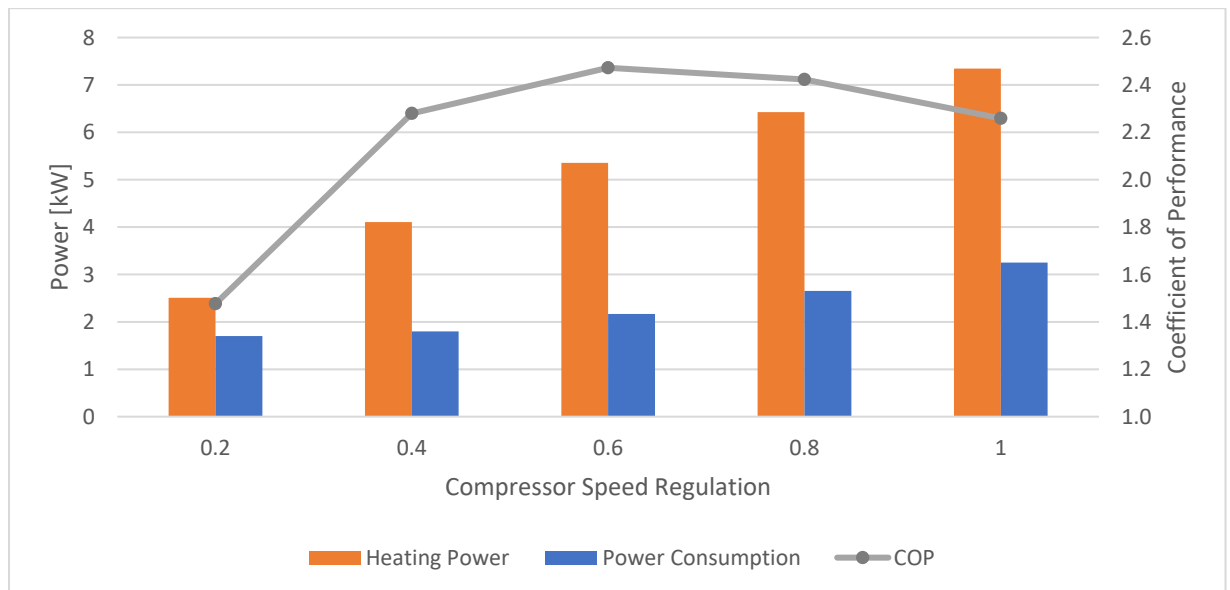


Figure 81. Simulation results - Performance curve of HVAC with various compressor speeds

As can be seen from the PH diagram, higher compressor speed will result in higher pressure difference between suction and discharge sides of the vapour-compression cycle. It could be seen from Figure 81 that the heating power and power consumption increase with the increase of compressor speed. However, the COP reaches its maximum at around 0.6 compressor speed.

4.1.3 Blower Characteristics

As discussed in Section 3.8.4, there are 5 linear levels of blower speeds with the maximum being 2.2458 kg/s . In this section, the characteristics of HVAC's blower are investigated by manually setting blower speed to the 5 different levels. During the tests, heating (heat pump) mode is used and the ambient and cabin temperatures are both set to -10°C . Compressor speed is set to maximum. Air circulation is turned off and the fresh air intake is turned on.

Figure 82 shows the pressure-enthalpy diagrams (PH diagrams) of the vapour compression cycle with different blower speeds. Figure 83 presents the coefficient of performance (COP) as well as heating power and power consumption of the HVAC.

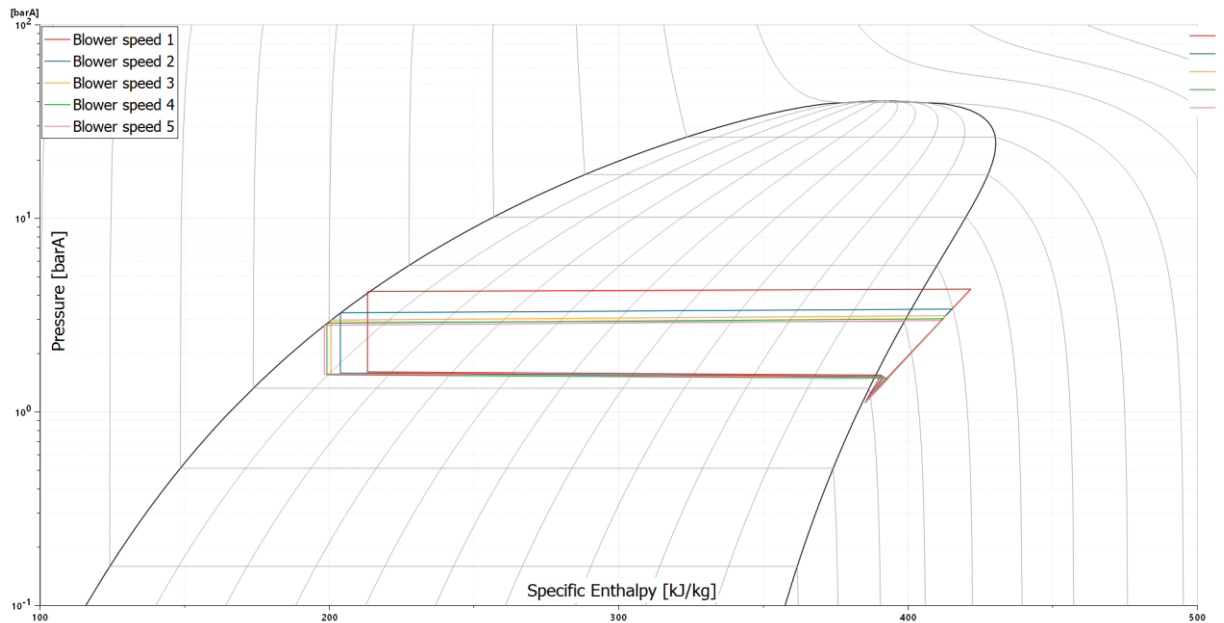


Figure 82. Simulation results - PH diagram of the vapour compression cycle with various blower speeds

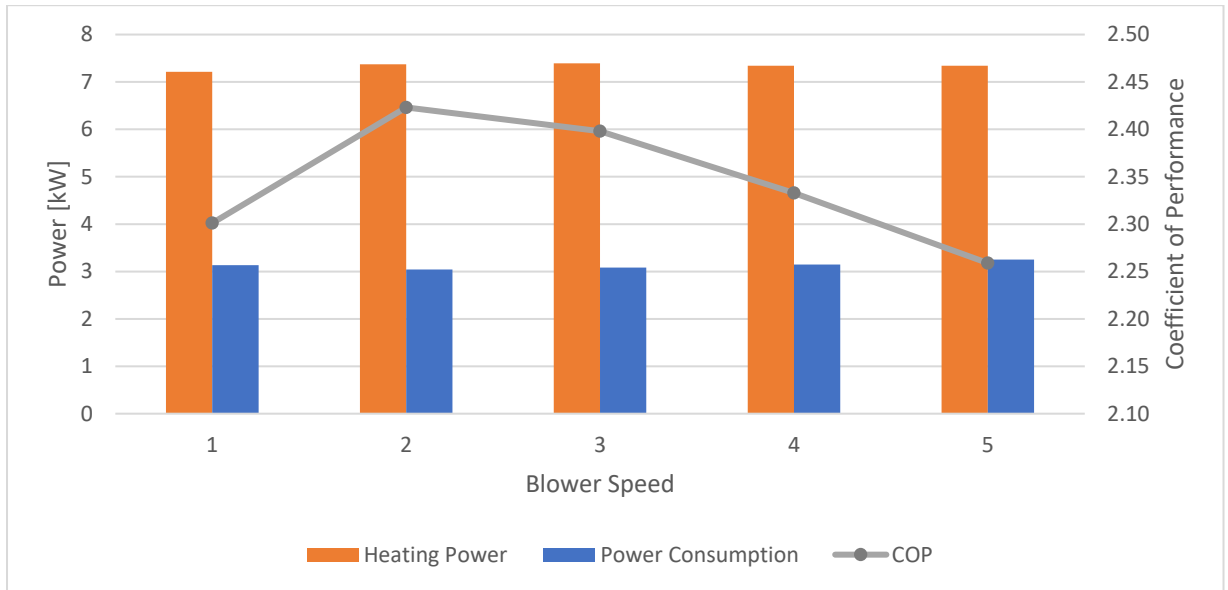


Figure 83. Simulation results - Performance curve of HVAC with various blower speeds

It could be seen from the PH diagram that lower blower speed results in higher discharge side pressure, due to a slower condensation process. It could be seen from Figure 83 that the effects of the blower speed on HVAC performance is on a smaller scale than ambient temperature and compressor speed. The efficiency of the HVAC is the highest when blower is set to level 2, although only by a small margin.

4.1.4 Comparison to Eberspächer AC136 AE HP

To compare with official data for Eberspächer AC136 AE HP, two additional tests are carried out in cooling and heating modes, both of which features a nominal condition and a max condition. The official data is denoted as *real* while the simulated results as *sim*. The relative value η is the percentage of the simulated result compared with the official data.

Table 13. Cooling results comparison between simulation and Eberspächer AC136 AE HP

Conditions		Cooling power comparison			Power assumption comparison		
		$P_{cool_{real}}$	$P_{cool_{sim}}$	η_{cool}	$P_{W_{real}}$	$P_{W_{sim}}$	η_W
Nominal	$T_{amb} = 35^\circ\text{C}$ $T_{cab} = 27^\circ\text{C}$	20 kW	15.49 kW	77.5 %	4.8 kW	6.9 kW	143.8 %
Max	$T_{amb} = 35^\circ\text{C}$ $T_{cab} = 40^\circ\text{C}$	26 kW	21.85 kW	84.0 %	5.4 kW	7.1 kW	131.5 %

Table 14. Heating results comparison between simulation and Eberspächer AC136 AE HP

Conditions		Heating power comparison			Power assumption comparison		
		$P_{heat_{real}}$	$P_{heat_{sim}}$	η_{heat}	$P_{W_{real}}$	$P_{W_{sim}}$	η_W
Nominal	$T_{amb} = -5^\circ\text{C}$ $T_{cab} = 16^\circ\text{C}$	11 kW	8 kW	72.7 %	2.4 kW	4.1 kW	170.8 %

Max	T_{amb} = 10°C T_{cab} = 20°C	18 kW	11 kW	61.1 %	3.3 kW	4.3 kW	130.3 %
-----	--	-------	-------	--------	--------	--------	---------

It could be seen from the results that there is still some performance gap between simulation and Eberspächer AC136 AE HP. This could be resulting from several reasons:

- Heat exchangers: although the size and pipe layout of the heat exchangers are known, there are still some data that is unknown, such as fin size, collector size, etc. These could all contribute to the gap.
- Thermal expansion valves: there is no data available for thermal expansion valve used in Eberspächer AC136 AE HP so the setting of TXVs could cause the difference. It is worth noting that the TXV for EHX which is used in heat pump mode is quite difficult to setup since it is difficult for a TXV to cover a wide temperature range of -20 °C to 10 °C .
- Pipes and refrigerant charge: in CAD drawings, there are data regarding the external diameters of pipes in the HVAC system. However, the insulation thickness, inner diameter, and length of pipeline are unknown. Additionally, the R134a refrigerant charge is unknown. Both factors could result in incorrect system pressure which will affect the performance of the HVAC.
- Top fans: there is no speed control in the simulation for the 0.7 kW top fans. In the real system, the fan is normally PWM or voltage controlled. Especially in heating mode, the EHXs could serve as evaporator quite well even without fans. This could cause more power consumption in the simulation.
- Compressor: the displacement and speed of the compressor are both unknown. It is only known that the maximum power consumption of the compressor is around 3 kW , which is simulated in the model. However, there might be some performance gap to the real system.

Nevertheless, the simulation model of the HVAC system delivers the performance needed for cooling and heating of the bus and works well as an HVAC system with heat pump mode. It could well-satisfy the purpose of the thesis – investigating the thermal solution of the battery electric bus.

4.2 Powertrain Cooling Performance

To demonstrate the cooling performance of the powertrain cooling loop, two simulations with a different ambient temperature of 30 °C and -10 °C were carried out using the same driving cycle. The driving cycle in use is (former) Espoo bus line 11 cycle. The coolant pump activation temperature is set at 50 °C , the radiator fan activation temperature is also set at 50 °C .

Figure 84 and Figure 85 upper part shows the temperature of the coolant as well as motor winding and inverter. It could be seen that in 30 °C environments, the cooling loop is able to keep the motor winding temperature at around $55 - 90\text{ °C}$ and inverter temperature at around $40 - 75\text{ °C}$. In -10 °C environment, the motor winding temperature is around $25 - 70\text{ °C}$ while the inverter is around $20 - 55\text{ °C}$. All within normal working conditions.

In 30 °C condition, the pump is working at its maximum for all the driving cycle while the radiator fan kicks in several times. In -10 °C condition, the pump is working at low speed for more than half of the cycle, and the radiator fan is never activated.

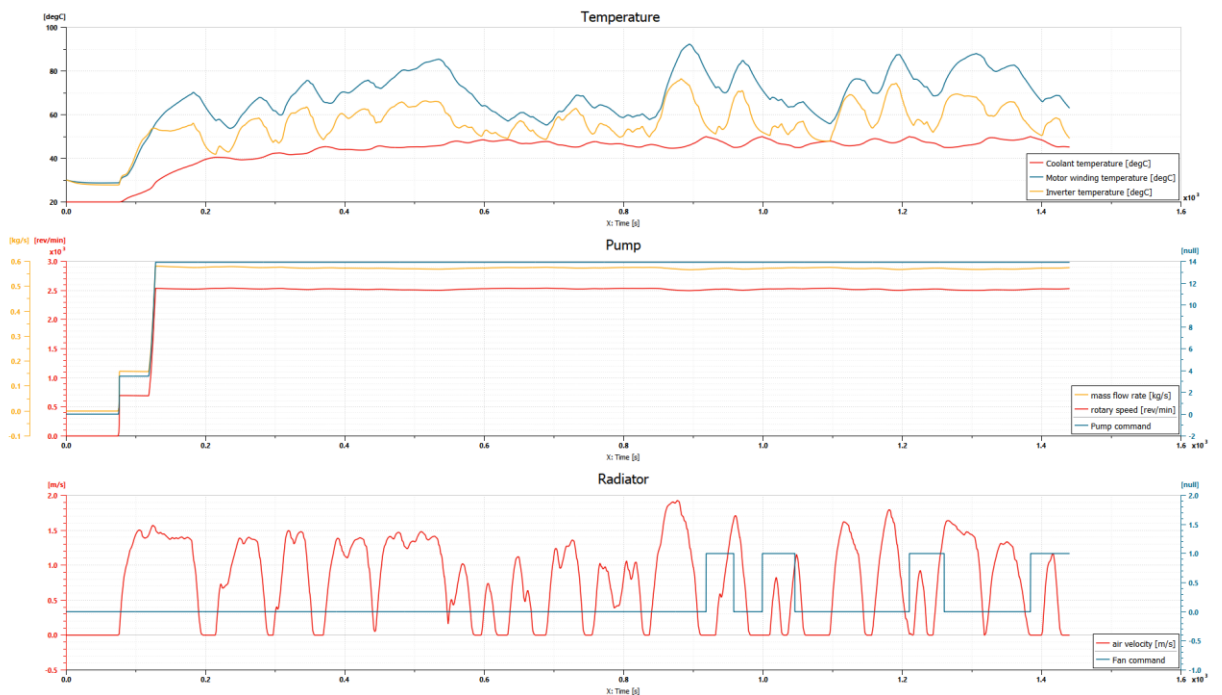


Figure 84. Powertrain cooling loop simulation results at 30 °C ambient

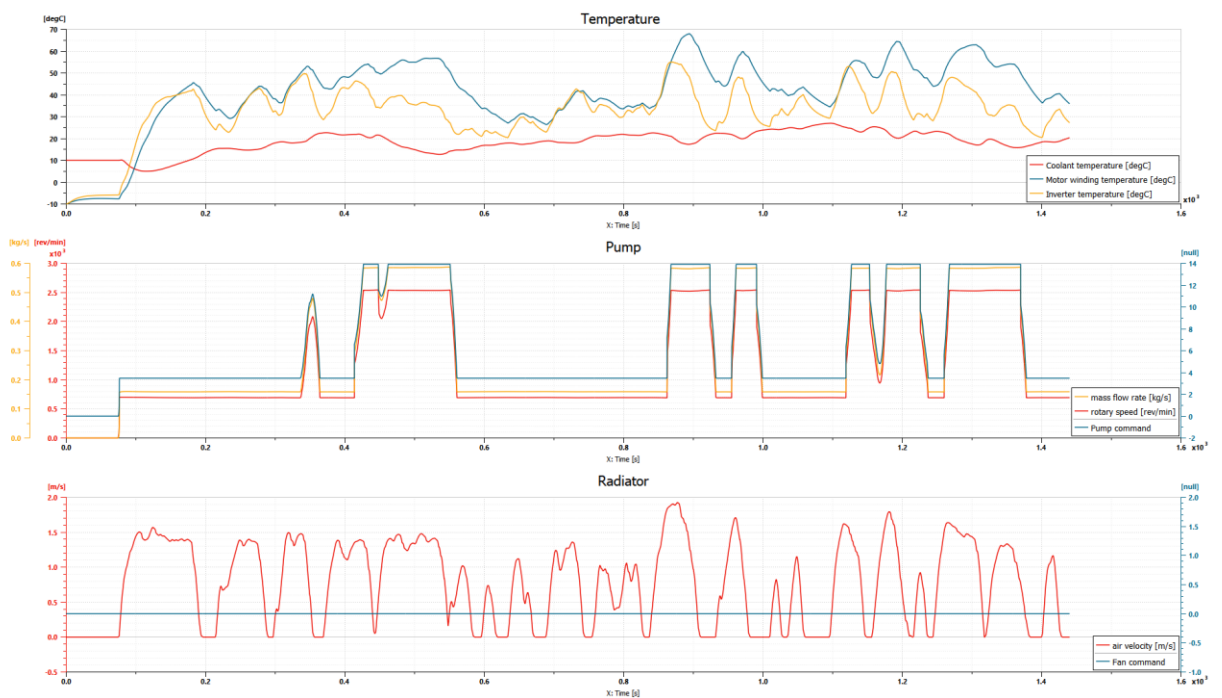


Figure 85. Powertrain cooling loop simulation results at -10 °C ambient

4.3 Powertrain Validation – Dynamometer Experiment

The data for the dynamometer test of e-Muuli in 2017 is used for validating the powertrain the simulation in the thesis. The test was carried out on the heavy-duty chassis dynamometer

of VTT shown in Figure 86 and **Error! Reference source not found.** The dynamometer has the ability to test vehicle from 2.5 to 60 tons and is able to handle continuous power of 300 kW. For power consumption measurement, the accuracy could reach $\pm 1\%$.

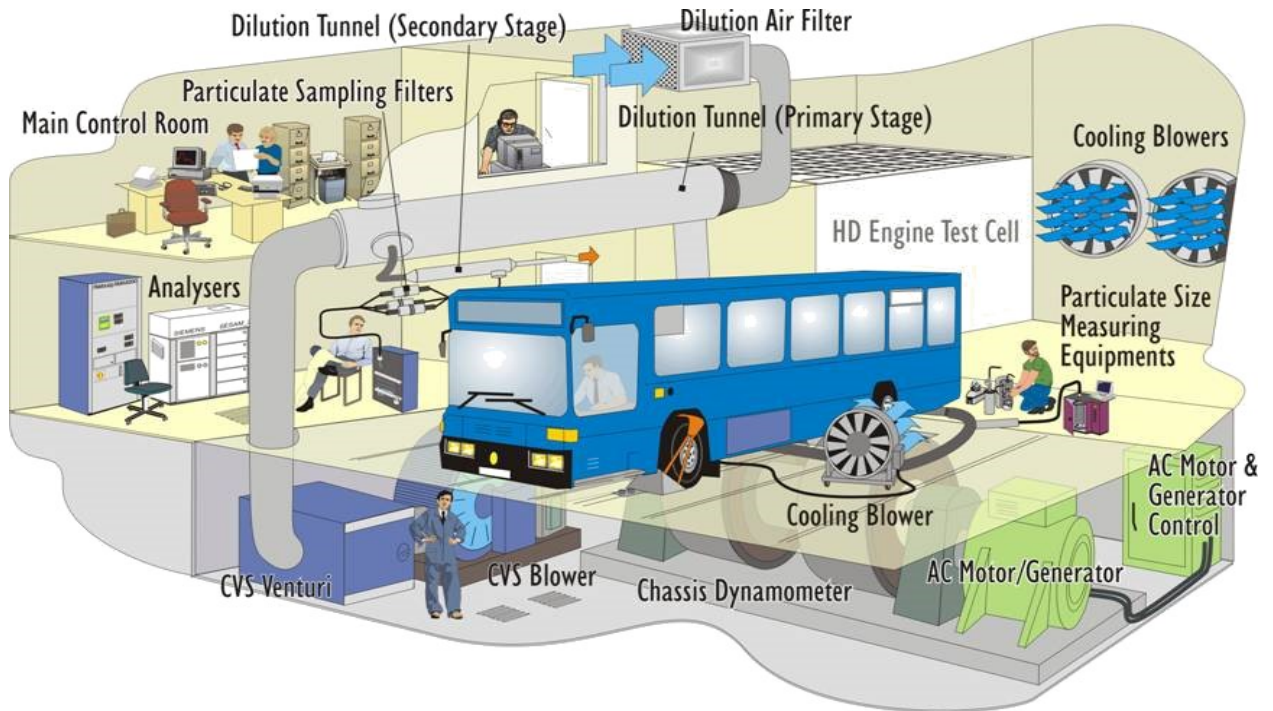


Figure 86. Schematic drawing for chassis dynamometer in VTT (VTT, 2015)

4.3.1 Experiment Setup

The cycle that was used for the dynamometer is Espoo bus line 11. The speed profile is shown in Figure 87 as the blue line. The red line in the figure also shows how the driver in the simulation follows the speed profile.

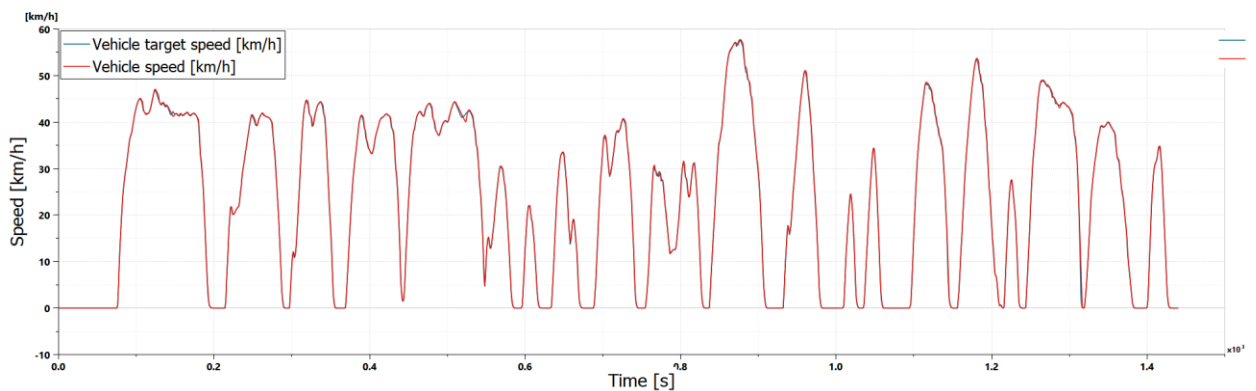


Figure 87. Speed profile of Espoo bus line 11

As discussed in section 3.4.3, the vehicle model is configured as ‘roller test bench’ mode, with resistance calculated as:

$$F_{res} = F_{cl} + a + b \cdot v + c \cdot v^2 = 852 + 0.983 \cdot v + 0.125 \cdot v^2$$

4.3.2 Results and Discussion

Figure 88 and Figure 89 present the motor torque and inverter output power related to time, with negative values represent regenerative braking. The blue line shows the result from Hioki power analyser measured during dynamometer experiment, while the red line shows the result from the simulation.

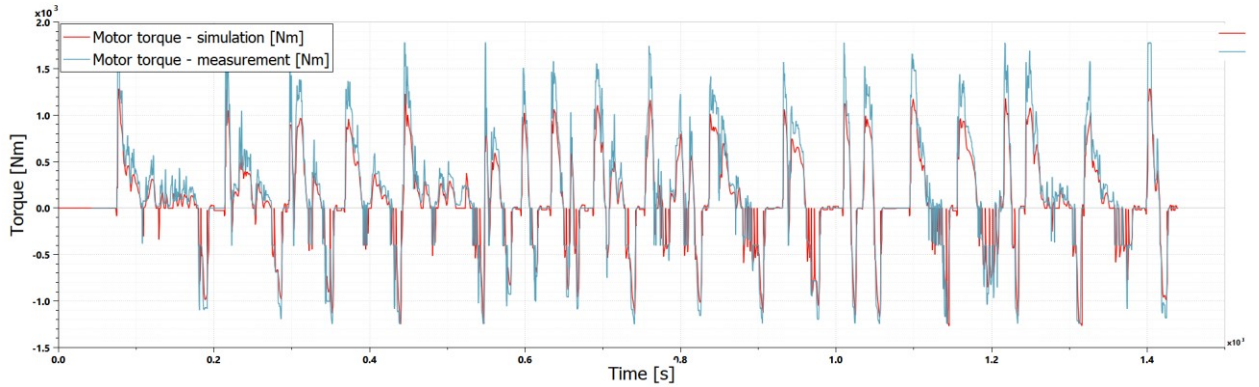


Figure 88. Motor torque comparison between simulation and measurement

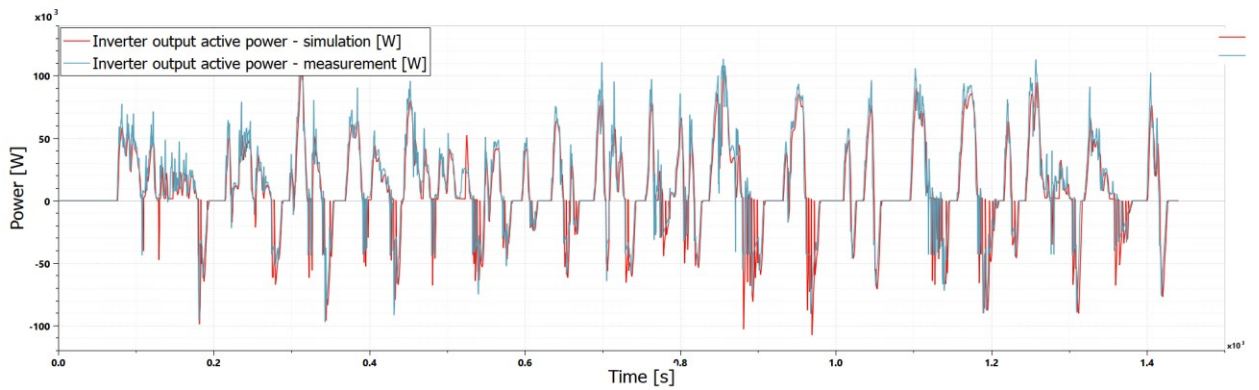


Figure 89. Inverter output active power comparison between simulation and measurement

It could be seen from the results that the simulation generally matches the measurement. There are more fast transitions in the measurement values. The trend of the simulated torque and power is consistent with the measurement. However, there are some differences in value, especially during the peaks. To quantify the difference, the following equation is used to calculate the root-mean-square error (RMSE):

$$RMSE(\hat{\theta}) = \sqrt{E((\hat{\theta} - \theta)^2)} \quad (46)$$

For speed, torque, and power, with the original sampling frequency from simulation, the RMSE is calculated as follow.

$$RMSE(v) = \sqrt{\frac{\sum_{t=0}^N (v_{sim,t} - v_{measure,t})^2}{N}} = 0.4123 \text{ km/h}$$

$$RMSE(T) = \sqrt{\frac{\sum_{t=0}^N (T_{sim,t} - T_{measure,t})^2}{N}} = 241.79 \text{ kNm}$$

$$RMSE(P) = \sqrt{\frac{\sum_{t=0}^N (P_{sim,t} - P_{measure,t})^2}{N}} = 17.454 \cdot 10^3 \text{ W}$$

The simulated results are in the correct magnitude range. The difference could come from the modelling of the powertrain. As discussed in Section 3.4.3, the resistance of the bus is calculated by Equation (23):

$$F_{res} = F_{cl} + a + b \cdot v + c \cdot v^2 = F_{cl} + 852.42 + 0.983 \cdot v + 0.1253 \cdot v^2$$

The dynamometer used to test e-Muuli uses a slightly different way to calculate the resistance:

$$F'_{res} = F_0 + F_1 \cdot v + F_2 \cdot v^2 = 265 + 0.983 \cdot v + 0.1253 \cdot v^2$$

Compared with F_{res} , F'_{res} does not consider the rolling resistance on the rear axle, which is measured directly by the dynamometer in the experiment. In the simulation, an approximation is made that the rolling resistance is:

$$F_{rol} = m \cdot g \cdot \eta \cdot f = 10715 \cdot 9.81 \cdot 0.7 \cdot 0.008 \text{ N} = 587.42 \text{ N} \quad (47)$$

where η is the weight distribution to rear axle, f is the rolling coefficient. F_{rol} is added to a in the equation. In the experiment, the rolling resistance coefficient could be related to speed, which will cause inaccuracy in resistance calculation, resulting in inaccurate torque and power values.

4.4 Thermal Validation – Temperature Experiments

For the purpose of validating the thermal simulation model, the temperature experiments were carried out on e-Muuli.

4.4.1 Experiment Setup

The cabin of e-Muuli was divided into 6 zones as shown in Figure 90. Temperature sensors were placed in each zone to measure and record the temperature of the cabin. One more sensor is used to measure the external temperature. The placement of the sensors is shown in Table 15 and Figure 91.

During 3 test days, two experiments are carried out. The cabin cool-down test was conducted on March 12th and will be further discussed in section 4.4.2. The heat pump test was conducted on March 13th and will be further discussed in section 4.4.3. March 11th was used to set up the electric bus e-Muuli and measuring equipment. Different measuring equipment is used for the two experiments, as shown in Table 15. Hioki power analyser is connected with three current sensors and one pair of voltage sensors to measure the voltage, current, and power.

Table 15. Experiment schedule and measurement equipment

	Test date	Test subject	Test duration	Temperature sensors	IR Thermometer	Hioki power analyser

1	March 12 th	Heat pump test	9:08 AM – 9:48 AM (40 min)	Yes	No	Yes
2	March 13 th	Cabin cool-down test	9:24 AM – 13:24 AM (4 hours)	Yes	Yes	No

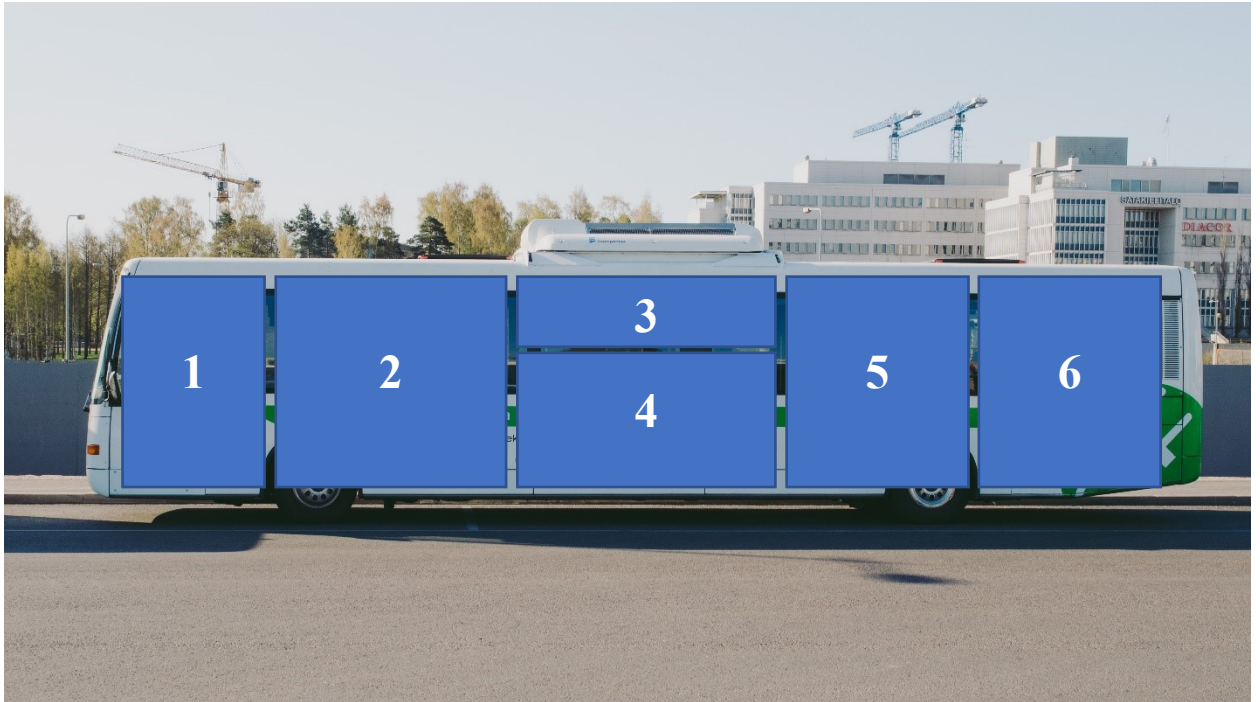
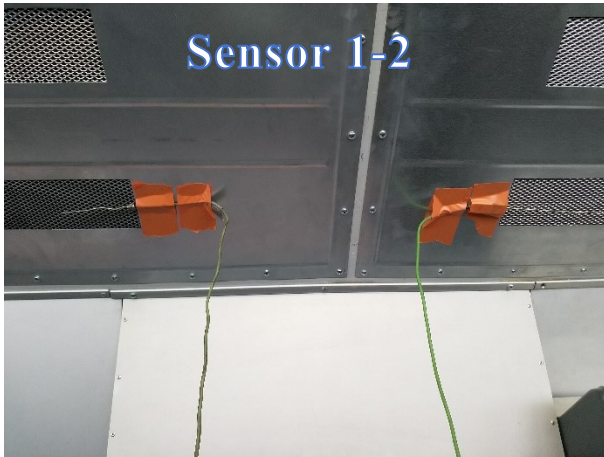


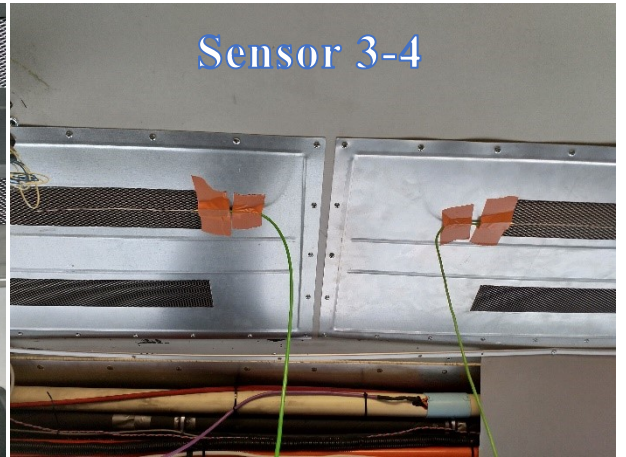
Figure 90. E-Muuli cabin zone division for the temperature experiments

Table 16. Temperature sensor details for the temperature experiments

Sensor number	Location description	Zone number
1	Air outlet	3
2	Air outlet	3
3	Air inlet	3
4	Air inlet	3
5	Cabin front	1
6	Cabin mid-front	2
7	Cabin middle	4
8	Cabin mid-rear	5
9	Cabin rear	6
10	Outside	N/A



Sensor 1-2



Sensor 3-4



Sensor 5



Sensor 6



Sensor 7



Sensor 8

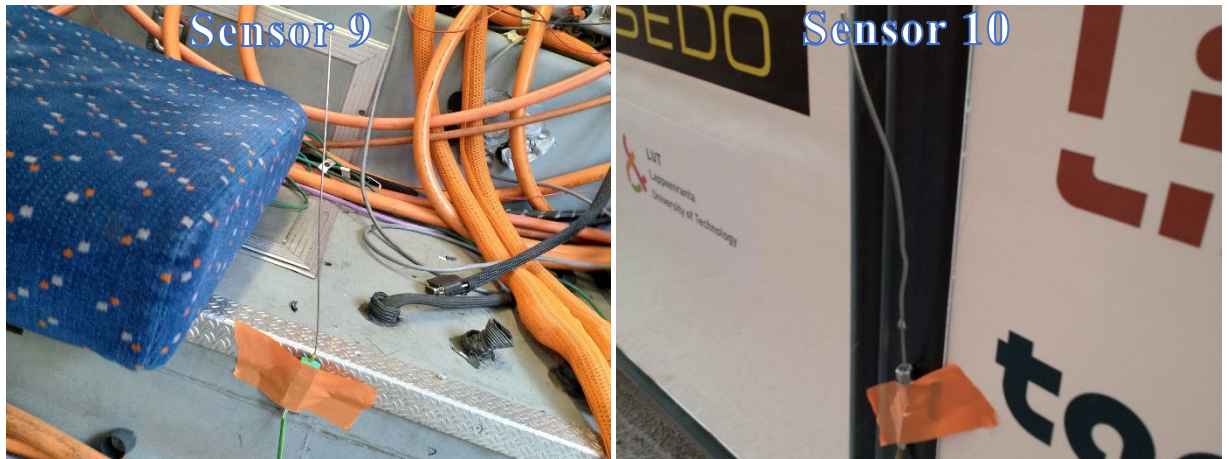


Figure 91. Sensors setup for the temperature experiment

The environmental data provided by Aalto IT (Aalto IT, 2019) (shown in Figure 92 - Figure 94) was used as the reference. These data are from sensors located in Otaniemi, which is within 500m range to the location of the experiment. These data are used for simulations that were setup to simulate the experiments.

The temperature and the relative humidity data are directly used in the simulation. The solar illuminance E (in lx or lm/m^2) need to be changed into solar irradiance I (in W/m^2) to be used in the simulation. As discussed in Section 3.7.5, Equation (32) is used:

$$I = 0.0095 \cdot \frac{W}{lm} \cdot E$$

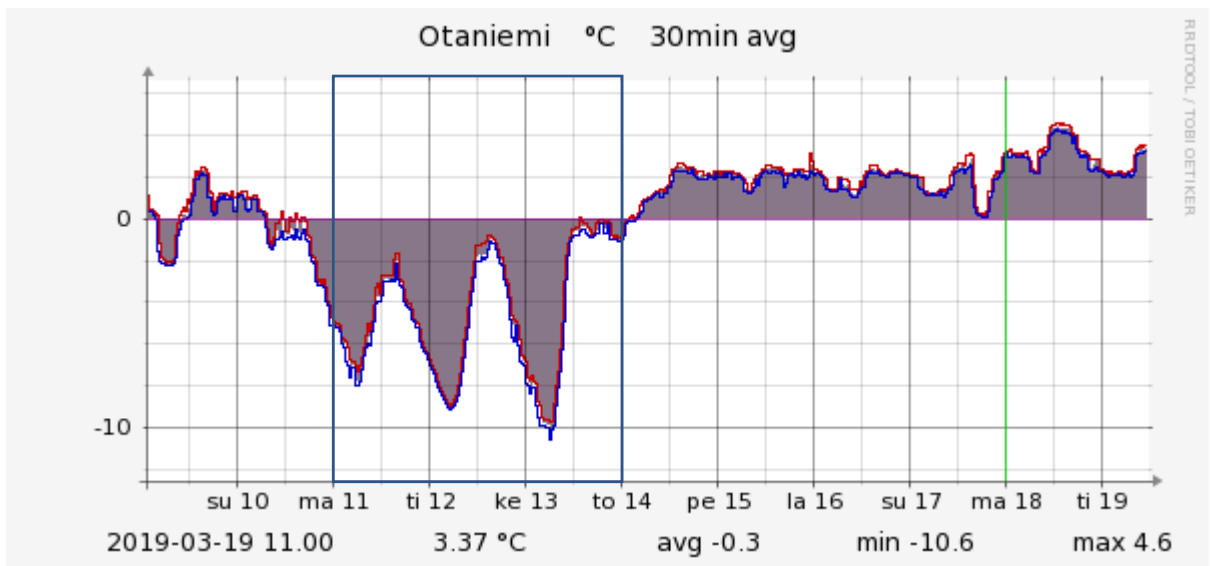


Figure 92. Temperature data for test dates (Aalto IT, 2019)

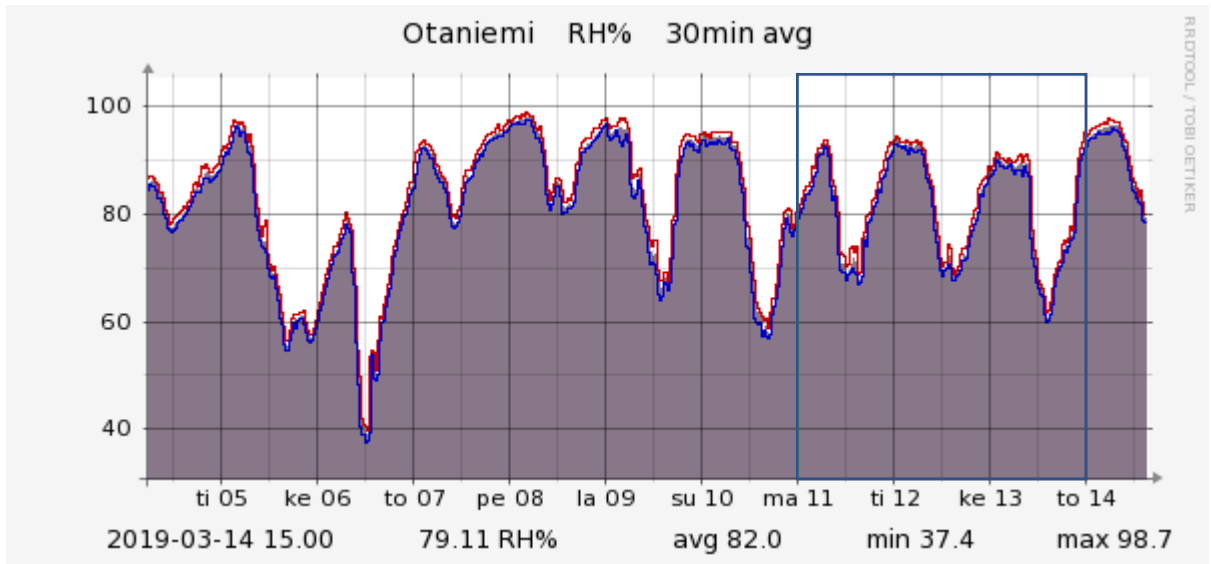


Figure 93. Relative humidity data for test dates (Aalto IT, 2019)

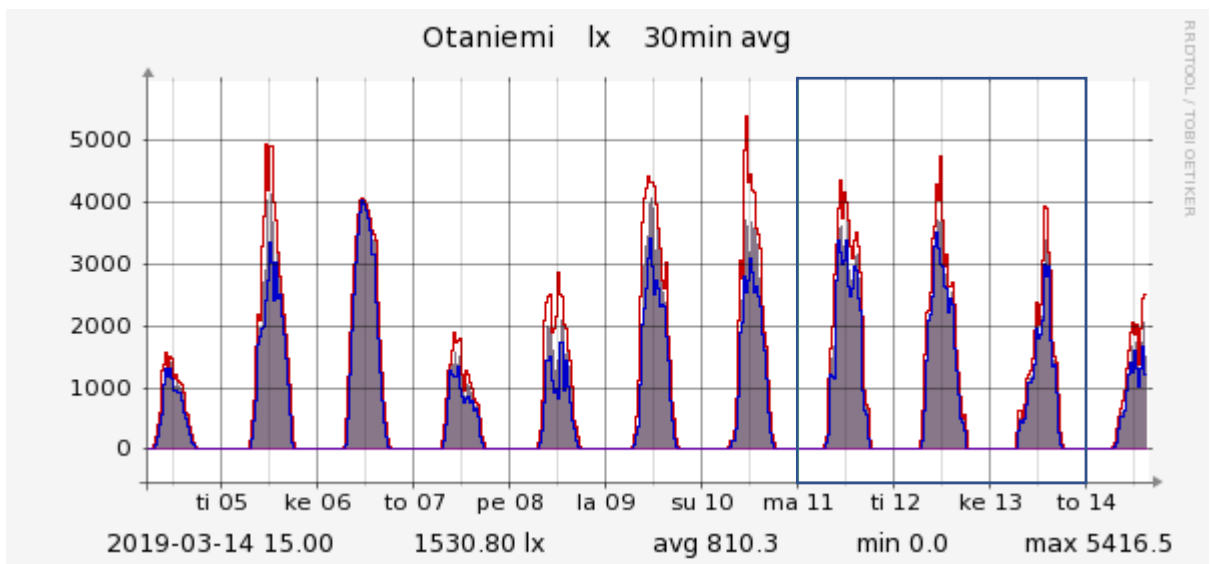


Figure 94. Solar illuminance data for test dates (Aalto IT, 2019)

4.4.2 Cabin Cool-down Test

For the cabin cool-down test, the bus was moved from the garage (warmer environment) to outside (cooler environment). The bus is kept outside for roughly 4 hours with door closed and electronics shut off. The temperature from 10 sensors is measured.

In the simulation, the solar irradiance is set to be an average value between the beginning I_0 and the end I_1 of the test using equation (32).

$$I_0 = 500 * 0.0095 \text{ W/m}^2 = 4.75 \text{ W/m}^2$$

$$I_1 = 2000 * 0.0095 \text{ W/m}^2 = 19 \text{ W/m}^2$$

$$\bar{I} = \frac{I_0 + I_1}{2} = 11.875 \text{ W/m}^2$$

There are 3 instances during the test where there is human inside the cabin to check the status of the test. As discussed in Section 3.7.4, the heat generated by a human is equivalent to a 100W heat source; the human factor is also taken into consideration in the simulation. A full list of testing information is shown in Table 17, the data is also used in setting up the simulation.

Table 17. Testing information of cabin cool-down test

Testing Period	March 3 rd , 9:24 – 13:29 (15596s in simulation)
Ambient Temperature	0 °C
Initial Cabin Temperature	12.1 °C
Initial Air Relative Humidity	70 %
Solar irradiance	11.875 W/m ²
Human Factor	Yes
Cabin Air Infiltration	Yes
Doors opening	No
HVAC	No

4.4.3 Heat Pump Test

For the heat pump test, the bus was moved from the garage (warmer environment) to outside (cooler environment). The heat pump is operated as the test cycle containing four 10-minute periods, as described in Table 18. The temperature from 10 sensors is measured.

Table 18. Heat pump test cycle

	0-10 min Period 1	10-20min Period 2	20-30 min Period 3	30-40 min Period 4
Heat pump	On	Off	On	Off
Blower	On, level 2	Off	On, level 5	Off

In the simulation, the solar irradiance is set to be

$$I_0 = 1580 * 0.0095 \text{ W/m}^2 = 15 \text{ W/m}^2.$$

A full list of testing information is shown in Table 19, the data is also used in setting up the simulation.

Table 19. Testing information for the heat pump test

Testing Duration	2560s in simulation
Ambient Temperature	-5 °C
Initial Cabin Temperature	10 °C
Initial Air Relative Humidity	70 %
Solar irradiance	15 W/m ²
Human Factor	No
Cabin Air Infiltration	Yes
Doors opening	No
HVAC	No

4.4.4 Results and Discussion

The result of the cabin cool-down test is presented in Figure 95. The measured average temperature shown in Figure 95 shows the weighted average of the 9 sensors in the cabin. The weights being used are the volumes of different zones shown in Figure 90.

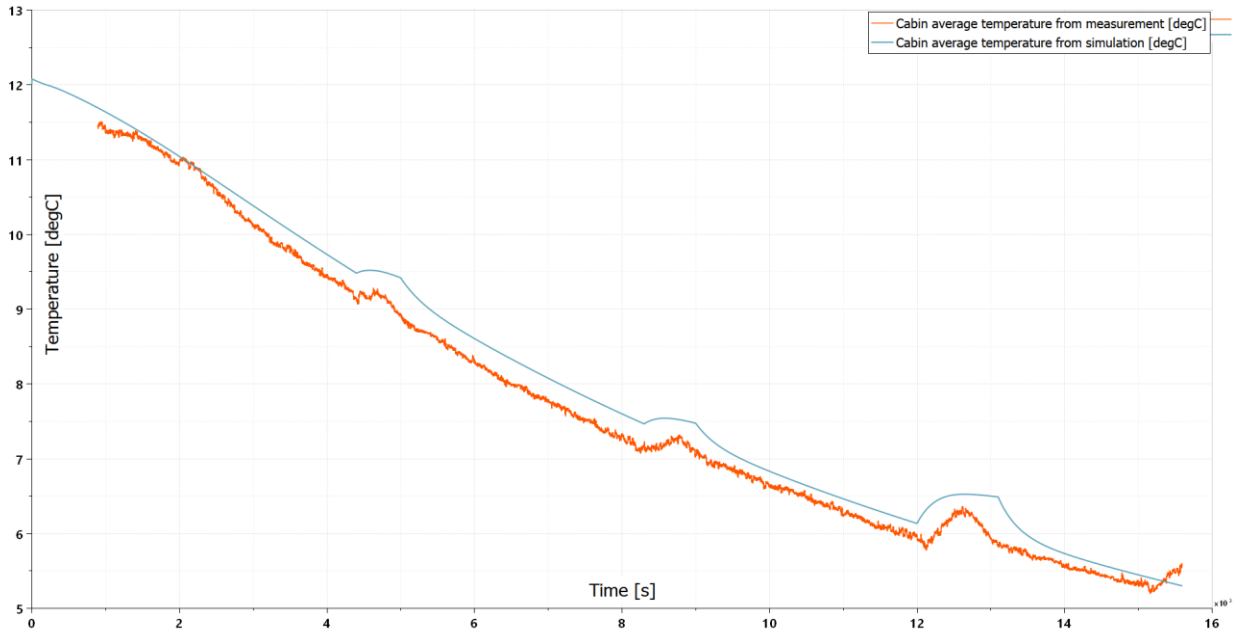


Figure 95. Simulation and measurement results comparison of the cabin cool-down test

As can be seen from the result, the temperature of the cabin drops below 6 °C at the end of the experiment. The temperature falling rate in the simulation resembles the measurement. To evaluate the accuracy of the simulation, the root-mean-square error is calculated by equation (46) with a sample period of 1s:

$$RMSE(T) = \sqrt{\frac{\sum_{t=896}^{15596} (T_{sim,t} - T_{real,t})^2}{15596 - 896}} = 0.2745 \text{ } ^\circ\text{C}$$

The RMSE is relatively low, suggesting an accurate cabin simulation in this condition.

The result of the heat pump test is presented in top two figures of Figure, while the lower two are the measurement data. The temperatures are shown on the left side while the electrical parameters, including power, current and voltage, are on the right.

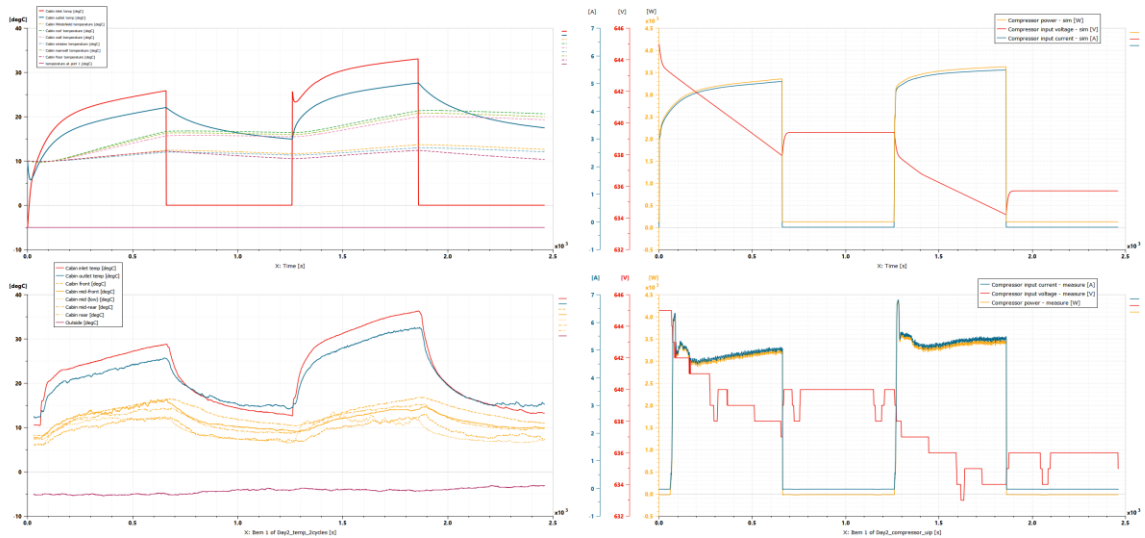


Figure 96. Simulation and measurement results comparison of the heat pump test

Table 20 shows the values of various data points including both measurement and simulation data. Only the cabin inlet (HVAC outlet) and cabin outlet (HVAC inlet) temperatures are compared, because other temperatures are not comparable – simulation results shows the solid temperatures of surface material while measurement data shows the air temperatures near surface material. From Figure 96 and Table 20, it could be seen that the temperature of cabin inlet and outlet as well as the electrical parameters of the HVAC system are consistent with the measurement data. Despite being slightly less powerful compared to the real-world system, the simulated heat pump system could satisfy the needs for the thesis.

Additionally, the voltage drop matches well with just 0.2V difference after one heat pump cycle, which indicates the OCV (open circuit voltage) curve used for the high-voltage battery (discussed in Section 3.5.1) is accurate.

Table 20 Data points comparison of the heat pump test

	Section 1		Section 2		Section 3		Section 4	
	Sim	Real	Sim	Real	Sim	Real	Sim	Real
Cabin inlet temperature	26°C	28°C	13°C	13°C	33°C	36°C	14°C	14°C
Cabin outlet temperature	22°C	26°C	15°C	15°C	28°C	32°C	18°C	16°C
Compressor current	5.1A	5.1A	0A	0A	5.6A	5.5A	0A	0A
Compressor voltage	638.0V	637.0V	639.3V	640.0V	634.2V	634.0V	635.8V	636.0V
Compressor power	3.3kW	3.2kW	0kW	0kW	3.6kW	3.4kW	0kW	0kW

As shown in the temperature figures in Figure 96, the cabin inlet temperature (shown in red curve) will drop to 0 °C once the heat pump is turned off. This is because in the simulation model, the temperature sensor is for cabin inlet is put after the internal heat exchanger's air outlet; once the blower is stopped, there is no air flow through the sensor resulting in the sensor showing the default value 0 °C.

As mentioned before, the cabin temperature results could not be compared with the measurement. However, it could be seen that the cabin temperature in the simulation result does not drop as much as the measurement data. At the end of period 2 and 4, the blue curve which represents the cabin outlet temperature as well as the average cabin temperature is higher than some of the cabin temperatures curve, which indicates the cabin air is gaining energy from the surfaces. This situation is contrary to the result established earlier by

Lajunen *et al.* (2017) shown in Figure 97. This indicates some inaccuracy in cabin modelling, possibly due to lack of accurate measurement of cabin body's material properties and thickness.

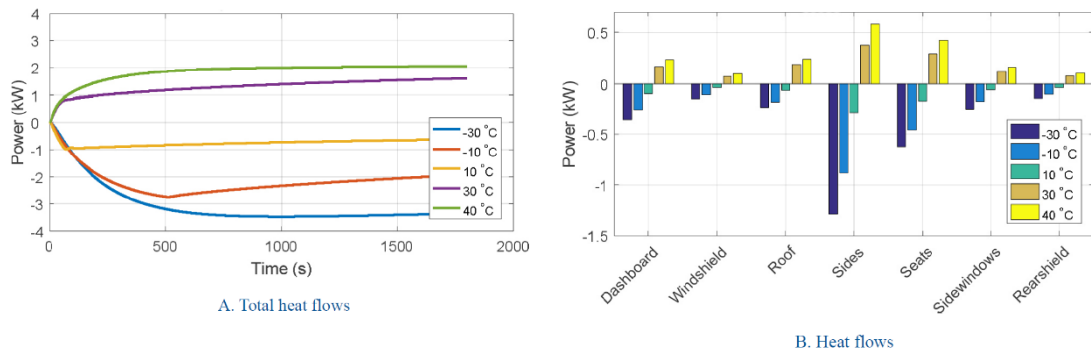


Figure 97 Simulation results of cabin heat flow in different ambient temperatures by Lajunen *et al.*, (2017)

5 Thermal Management Solutions

5.1 Thermal Management Solutions and Modelling

5.1.1 Positive Temperature Coefficient (PTC) Heater

In this section, the positive temperature coefficient (PTC) heater or resistive heating is introduced to the existing system.

PTC heater normally contains four layers: control board part, upper coolant passage part, PTC element part, and lower coolant passage part (Zhang *et al.*, 2018a). The PTC element has its unique characteristics – the resistance will increase rapidly at a certain temperature. This will result in reducing current under certain voltage. This property will keep the material from overheating (Jeong and Lee, 2015).

PTC heating is used in electric vehicles for cabin heating. As discussed in Chapter 4.1.1, the efficiency of a heat pump will drop greatly with the decrease in ambient temperature. The COP of the heat pump system in the electric bus simulation will drop from 291% to 180% when the ambient temperature drops from 10 °C to –20 °C. Therefore, PTC is currently used as a common way for cabin heating in extremely cold condition to compensate the inefficiency of heat pumps.

The PTC heater in the simulation model is shown in Figure 98. The PTC heater is directly powered by the high voltage battery. The maximum power is set at 2.5 kW, and the power delivery has 5 different levels: 500W, 1000W, 1500W, 2000W, 2500W. The heater is connected with a simple heat core that is exchange thermal energy with cabin ventilation air.

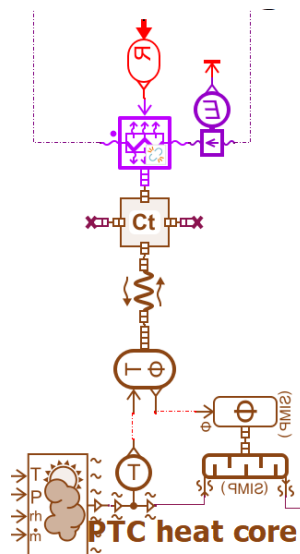


Figure 98. PTC heating system model in the simulation

5.1.2 Powertrain Waste Energy Harvesting through Chiller

In this section, the chiller or liquid-to-air heat pump is introduced to the existing system. Powertrain wasted heat is harvested from the powertrain cooling loop to the HVAC system, which will be eventually used to heat up the cabin.

In vehicles that are powered by an internal combustion engine (ICE), waste heat from the engine is normally used for heating up the cabin in cold weather. For a battery electric

vehicle, the electrified powertrain is much more efficient than ICE powertrains thus generate much less waste heat; the traditional method could not be used in electric vehicles. Nevertheless, the powertrain of a heavy-duty electric vehicle such as electric city bus could still generate a decent amount of heat that is previously been collected by the powertrain cooling loop and dissipated through radiator. As discussed in the powertrain cooling test in Section 4.2, in -10°C ambient temperature, the powertrain coolant could still heat up to 25°C during a driving cycle.

However, 25°C is not enough to directly heat up the cabin using the cabin heating solutions from conventional vehicles. It is because that for coolant to heat up cabin air, the heat needs to be transferred from coolant to the metal on heat exchanger and then from the metal to cabin air. Both the heat transfer procedure could be seen as a combination of conduction and convection which has been discussed in Section 2.1.1. As can be seen from the equations of convection and conduction, the energy transfer is proportional to the temperature difference. If the temperature difference between coolant and air is too small, for example $T_{cabin} = 10^{\circ}\text{C}$ and $T_{coolant} = 20^{\circ}\text{C}$, the heat transfer will not be enough to heat up the cabin.

To harvest the energy from the coolant loop, an agent that is much cooler than the cabin temperature needed to be found. In this sense, the refrigerant in the HVAC system that has just pass the thermal expansion valve satisfies the requirement. As discussed in Section 2.2.1, the refrigerant that has just passed through thermal expansion valve going into the evaporator is in the coolest state of the loop. Depending on the cabin and ambient temperature, the temperature of the R134a refrigerant could be as cold as -20°C . It could be used to serve the purpose of absorbing heat from the powertrain coolant.

Therefore, a corrugated plate heat exchanger (or called chiller) is installed to the system. It comes with a dedicated thermal expansion valve. The chiller is used to transfer heat between two fluid, refrigerant and coolant. The chiller with its TXV is placed parallel to the external heat exchanger on the HVAC side and parallel to the radiator on the powertrain cooling loop side. Once enabled, the chiller will bypass both the EHX and the radiator. The HVAC system now works as a liquid-to-air heat pump which transfers heat from coolant to cabin air, in addition to the air-to-air heat pump which transfers heat from ambient air to cabin air. The modified system is shown in Figure 99.

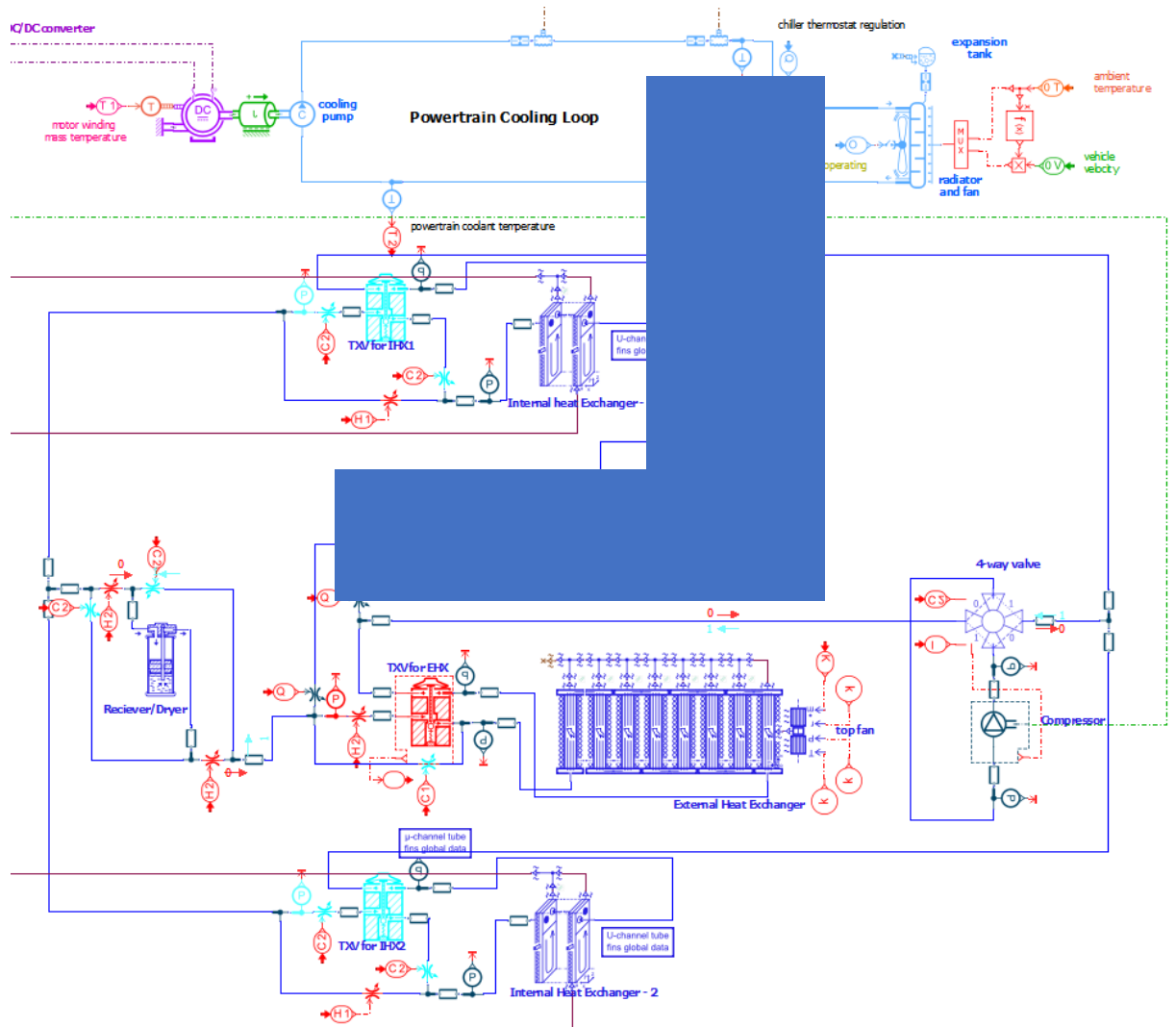


Figure 99. Modified HVAC and powertrain cooling system model with a chiller in the simulation

Title	Value	Unit	Name
index of fluid	1		fiTPF
index of thermal hydraulic fluid	1		fi
solid type index	1		sol1
expression for mass of material [kg] = f(numPlates)	2.346		massTHExp
<ul style="list-style-type: none"> □ initialization <ul style="list-style-type: none"> □ liquid side <ul style="list-style-type: none"> liquid side initial pressure liquid side initial temperature □ refrigerant side <ul style="list-style-type: none"> type of initialization pressure temperature 			
	1.013	barA	plnitTHH
	20	degC	tempInitCTHH
	...d temperature		hcond
	24.8	barA	plnit
	30	degC	tempClnit

<ul style="list-style-type: none"> global configuration 			
number of cells	3 cells		nbCells
number of liquid channels	7		nChannelTHH
number of refrigerant channels	6		nChannelTPF
<ul style="list-style-type: none"> geometrical parameters 			
channel height	325 mm		height
heat exchange area per plate and per side	...0000000e-06 mm**2		ceArea
<ul style="list-style-type: none"> liquid side 			
liquid side hydraulic diameter per channel	1.5 mm		diamTHH
liquid side cross-sectional area per channel	150 mm**2		xAreaTHH
liquid side volume per channel	0.2/7 L		volChannelTHH
<ul style="list-style-type: none"> refrigerant side 			
refrigerant side hydraulic diameter per channel	1.5 mm		diamTPF
refrigerant side cross-sectional area per channel	150 mm**2		xAreaTPF
refrigerant side volume per channel	0.2/6 L		volChannelTPF
<ul style="list-style-type: none"> pressure drop 			
<ul style="list-style-type: none"> liquid side 			
liquid side relative roughness	1e-05 null		rrTHH
<ul style="list-style-type: none"> refrigerant side 			
acceleration pressure drop calculation	no		acc
two-phase flow frictional pressure drop correlation	...ms correlation		dp2pCorr
refrigerant side absolute roughness	0 mm		rabsTPF
refrigerant side frictional pressure drop gain	1 null		kdpTPF
<ul style="list-style-type: none"> heat exchange 			
<ul style="list-style-type: none"> liquid side 			
convective heat transfer definition	Nusselt number		hexDef
expression for free Nusselt number = f(Gr, Pr, cdim[mm], th...	...3*(Gr*Pr)^(1/3)		freeNuExp
laminar to turbulent transition for convection: lower Reynol...	2300 null		ReTrans1
laminar to turbulent transition for convection: upper Reynol...	10000 null		ReTrans2
expression for forced laminar Nusselt number = f(Re, Pr, len...	...us)^0.14, 3.66)		forcedNuLamExp
expression for forced turbulent Nusselt number = f(Re, Pr, L...	...8)*(Pr^(2/3)-1))		forcedNuTurbExp
liquid side heat transfer gain	3 null		kHeatTHH
<ul style="list-style-type: none"> refrigerant side 			
laminar Nusselt number (see description)	3.66 null		nuLamTPF
single-phase: correlation choice	...tion (Gnielinski)		spCorr
condensation: correlation choice	Shah correlation		condCorr
condensation: Nusselt number definition (Shah)	...n (Mac Adams)		condNundef1
boiling: correlation choice	...bes correlation		boilCorr
boiling: Nusselt number definition (VDI for vertical tubes)	...tion (Gnielinski)		boilNundef2
refrigerant side heat transfer gain	3 null		kHeatTPF

Figure 100. Parameters for the chiller model in the simulation

Title	Value	Unit	Name
Ⓢ bulb temperature	20	degC	tbulb
index of fluid	1		fi
maximum hydraulic diameter	5	mm	hdmax
critical flow number	10000	null	lamc
maximum mass flow rate at reference conditions	0.07	kg/s	dmmmax
m coefficient	1	null	mc
bulb saturation pressure at 0 degC (p0)	2.9	barA	p0
bulb saturation pressure at 10 degC (p10)	4	barA	p10
reference pressure (pref)	18	barA	pref
valve opening temperature at p0	0.5	degC	top
valve full-opening temperature at p0	5.5	degC	tfo
reference subcooling	5	degC	scref
time constant	20	s	tau

Figure 101. Parameters for the Chiller TXV model in the simulation

On the HVAC side, the refrigerant flow towards the chiller is controlled by two magnetic valves, which will open when the chiller is turned on and keep close on other occasions. It is worth noting that even if the chiller is turned on, most part of the flow will still be directed to the EHX because the chiller or liquid-to-air heat pump alone will not be able to produce enough heating power for the cabin. The chiller works as a supplement to the existing system.

On the powertrain cooling loop side, the coolant flow towards the chiller is controlled by a thermostat. The thermostat senses the coolant temperature and helps it maintain a designated

level. Once the coolant temperature exceeds the designated temperature, the flow will be directed to the chiller thus transferring energy to the refrigerant in HVAC. When the coolant drops beneath the designated temperature, the thermostat will direct the flow to the radiator inside the cooling loop. Currently the target temperature is set to be 15°C. The lower the target temperature, the more aggressive the chiller harvest energy. However, the target should not be set lower than the operating temperature of powertrain components.

Therefore, under the same environmental conditions, the level of powertrain waste heat that could be harvested through the liquid-to-air heat pump is determined by the controlled temperature of the thermostat. The lower the temperature, the more heat could be used to heat up the cabin. However, the coolant temperature should be kept above a level that the minimum working temperature of motor and inverter could be reached.

5.1.3 Thermal Energy Storage through Phase Change Material (PCM)

In this section, phase change material (PCM) is used for pre-storing thermal energy during charging, which will be released to a heat exchanger that heats up the cabin.

As discussed in Section 1.2.2, PCMs are a group of materials that uses latent heat while changing phase (typically melting and freezing) to absorb or release a relatively large amount of thermal energy at essentially constant temperature (Wang *et al.*, 2017). PCM will absorb energy during liquefaction and release energy during solidification. The phase changing temperatures varies from materials. Wang *et al.* investigates five families of PCM, synthesized several PCM candidates, and use Differential Scanning Calorimeter (DSC) to measure the melting temperature and the latent heat. The results are shown in Table 21.

Table 21. Properties of various phase change materials (PCMs)

PCM	Melting point (°C)	Latent heat (J/g)	Latent heat ratio over water
DPTm12	-12	267	0.80
DPT14	14	298	0.89
DPT23	23	335	1.00
DPT38	38	320	0.96
DPT50	50	343	1.03
DPT68	68	342	1.02
DPT83	83	348	1.04
DPT86	86	321	0.96

Because of the combination of high melting point and high latent heat, DPT83 is chosen to be the material used in the simulation. The setting for the PCM is shown in Figure 102. It is assumed that the PCM is charged to 90 °C. Assume that the PCM will solidify to 20 °C in its final state. The total thermal energy it preserves could be calculated as:

$$Q = Q_{sens_{liq}} + Q_{latent} + Q_{sense_{solid}} \quad (48)$$

where $Q_{sens_{liq}}$ is the sensible heat of PCM in liquid form:

$$Q_{sens_{liq}} = m \cdot C_{pL} \cdot \Delta T = 100 \cdot 2 \cdot (90 - 83) J = 1.4 kJ \quad (49)$$

Q_{latent} is the latent heat while phase changing:

$$Q_{latent} = m \cdot H_{lat} = 100 \cdot 348 \text{ kJ} = 34800 \text{ kJ} \quad (50)$$

$Q_{sens_{solid}}$ is the sensible heat of PCM in solid form:

$$Q_{sens_{liq}} = m \cdot C_{pS} \cdot \Delta T = 100 \cdot 1.5 \cdot (83 - 20) \text{ J} = 9.45 \text{ kJ} \quad (51)$$

Therefore, $Q = 34810.85 \text{ kJ}$.

The thermal energy could be stored to the PCM heater during charging, similar to charging a battery. If a 5 kW heater is used, it will take $t = 34810.85 / (5 \cdot 3600) = 1.93 \text{ h}$ to charge the PCM. Additionally, more electric buses are adopting fast charging technology, which will result in high heat energy loss during both fast charging from the grid and regenerative braking (Smith *et al.*, 2018). The heat generated by battery pack could also be used to charge the PCM.

Title	Value	Unit	Name
Ⓢ PCM temperature at port 1	90	degC	Tout1
type of Cp equivalent variation	triangle shape variation		Ctype
mass	100	kg	mass
Cp of solid phase	1.5	kJ/kg/K	CpS
Cp of liquid phase	2	kJ/kg/K	CpL
melting temperature	83	degC	Tm
latent heat fusion	348	kJ/kg	Hlat
melting temperature range	1	degC	range

Figure 102. Parameters for the PCM model in the simulation

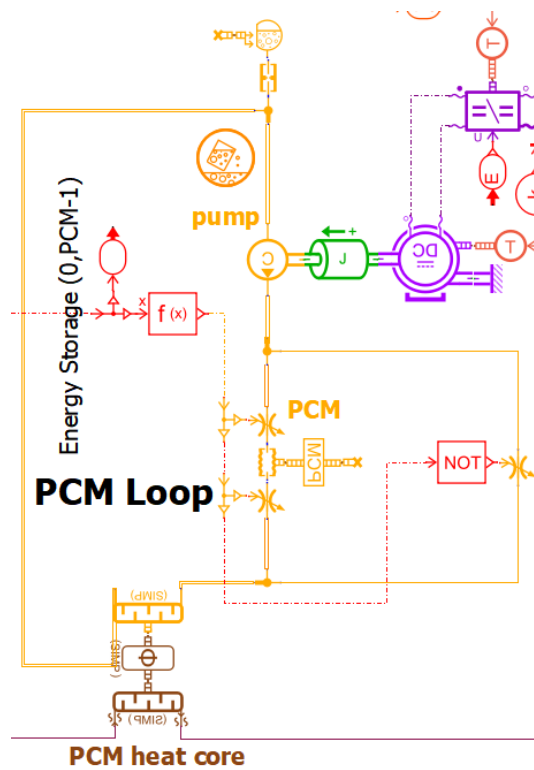


Figure 103. PCM loop model in the simulation

Figure 103 shows the simulation model of the PCM heater, which is a coolant loop transferring heat from PCM to the heat exchanger located in the cabin. Water is chosen to be the coolant in the loop for it is easily accessible. The loop is driven by a pump connected to the 24V auxiliary circuit. The power delivery of the PCM heater is determined by the pump speed which is controlled by adjusting the input voltage. The PCM is located within a branch in the loop. When PCM heater is turned on, two magnetic valves will direct the coolant flow through the branch. When PCM heater is turned off, the branch will be bypassed. In the simulation model. The PCM is ideally insulated with no energy loss through PCM casing or coolant.

The water in the loop will carry energy from PCM to a heat exchanger that connects the PCM loop and the ventilation air. A simple heat exchanger model is used. Because the power of the heat exchanger is heavily depend on the temperature difference between the coolant and the ventilation air (Lajunen *et al.*, 2017), the ability of PCM to release thermal energy while remaining mostly at a constant temperature will result in much stable heat exchange, compared to traditional thermal energy storage solutions such as coolant storage tank.

The PCM heater is designed to deliver a maximum of 3.8 kW during operation. It could be used separately or as a supplement to the PTC heater or HVAC. When the PCM loop is running at full power, the energy of the PCM could be used continuously for 2.54 h.

5.2 Simulation Setup

A real-life driving cycle of a bus line in Helsinki is used to test the battery electric bus simulation model. Factors such as passenger loads, doors openings, and slope are considered. Different thermal management solutions, including heat pump, PTC heater, chiller, and PCM heat storage, are simulated in different configurations in various ambient temperatures. Energy consumption is measured and analysed.

5.2.1 Driving Cycle

The selected driving cycle is 35 km long and takes 10110 s to finish. The cycle consists of two back-and-forth runs of a same bus line in the morning rush hour when the payload and bus stops frequency are at maximum of the day. The selected cycle also represents various workloads; it could be seen from the Table 22 that the second run of each direction (segment 3 and 4) carries more passenger than the previous runs (segment 1 and 2). All the data used in the driving cycle is measured from the sensors installed on-board the bus.

Table 22 Segmentation of the driving cycle used in the simulation

Segments	Direction	Time		Bus status	Door open time	Average passenger
Segment 1	A-B	2151s	0-242s	Stop	0%	8.18
			242-2151s	Running	16.92%	
Segment 2	B-A	2749s	2151-2804s	Stop	0%	6.43
			2804-4900s	Running	5.68%	
Segment 3	A-B	2743s	4900-5740s	Stop	0%	11.95
			5740-7643s	Running	16.40%	
Segment 4	B-A	2467s	7643-8140s	Stop	0%	16.45
			8140-10110s	Running	11.88%	

The speed profile shown in Figure 104 is used as the speed command for the driver model in the simulation model.

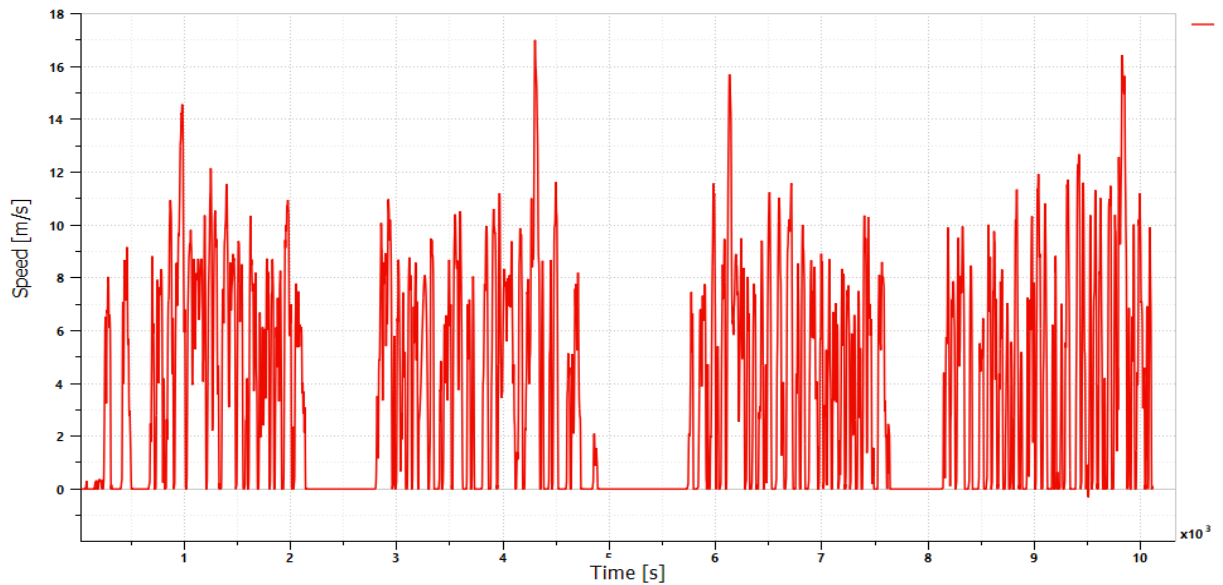


Figure 104. Speed profile of the driving cycle

The payload is shown as a blue line in Figure 105, which is used as payload of the bus, as well as used to calculate the number of passengers on on-board. An average weight of 70 kg is used for each passenger. The passenger load is then used for the human heat generation inside the cabin. The stacked distribution of passenger load is shown in Figure 106. Each colour represents one segment in the cycle and the distribution is stacked together to represent the whole cycle.

The bus stops are shown in Figure 105 as a red line. It is used in the model as the doors opening cycle for the doors opening model.

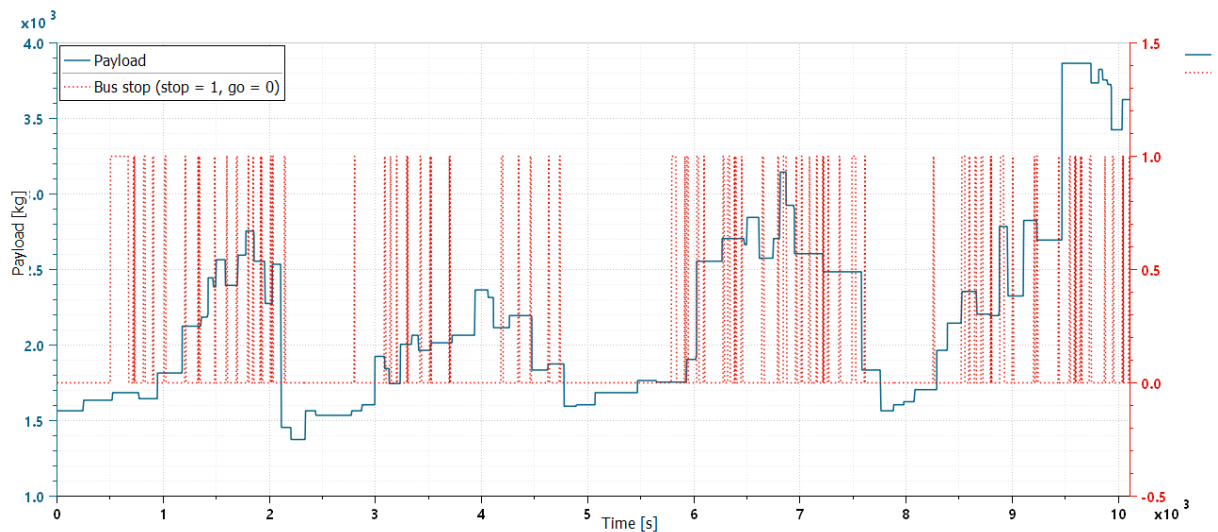


Figure 105. Payload and bus stops of the driving cycle

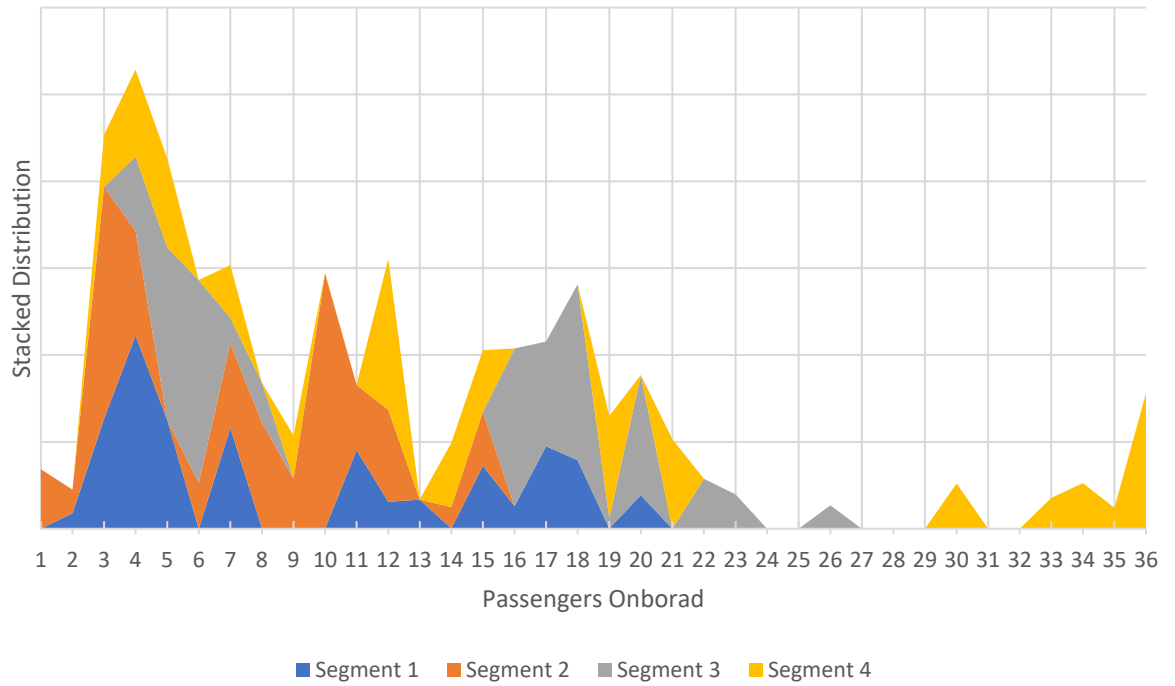


Figure 106. Passengers stacked distribution for each segments of the driving cycle

Figure 107 shows the slope in percentage related to the driving distance of the bus. It is used as the slope information in the bus simulation model.

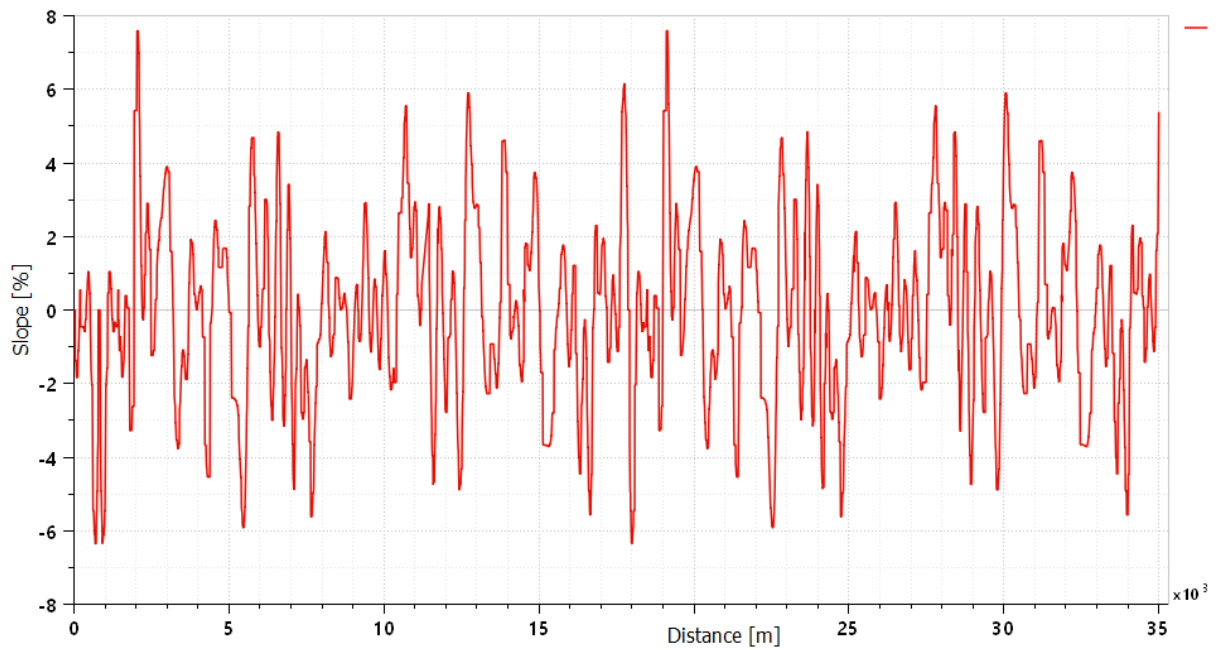


Figure 107. Slope-distance graph of the driving cycle

5.2.2 Thermal Management Configurations

The cabin thermal management solutions discussed in the thesis, including HVAC (cooling and heat pump), PTC heater, chiller and PCM, are grouped into 5 possible configurations listed in Table 23.

Table 23. Thermal management configurations for the simulation

No.	Configurations	Abbreviations
1	Heat pump + 1.5 kW PTC heater	HP+PTC
2	HVAC (heat pump / cooling)	HP / AC
3	Heat pump + Chiller	HP+Chiller
4	Heat pump + 3.8 kW PCM heating loop	HP+PCM
5	Heat pump + Chiller + 3.8 kW PCM heating loop	HP+Chiller+PCM

In the simulation configurations, PTC heater, chiller, and the PCM heating loop are all used in addition to the heat pump. It is worth noting that PTC heater and PCM heating loop could be used unaccompanied by the heat pump, while chiller would always work with the heat pump, because the waste thermal energy is harvested to the HVAC refrigerant loop.

The ambient temperatures for the simulations are set between -20°C to 40°C . The details for the configurations in each temperature setting is listed in Table 24. For all the configurations, the target cabin temperature is set to 20°C .

Table 24 Simulation setup with different configurations

Ambient Temperature	Thermal Management Configurations
-20°C	1 – 5
-10°C	1 – 5
0°C	1 – 5
10°C	1 – 5
20°C	2
30°C	2
40°C	2

Additionally, the ambient relative humidity is set to be 50%, and solar radiation is set to be $15\text{ W}/\text{m}^2$.

5.3 Simulation Results

Figure 108 and Figure 109 present the simulation results of the specific energy consumption (in Wh/km) of different thermal management configurations in various ambient temperatures. Figure 108 shows the results without doors opening model, while Figure 109 shows the result with the doors opening model. The energy consumption from different systems are shown in different colour: Motor in blue, HVAC Compressor in orange, Auxiliary including HVAC Blower and Fan in yellow, PTC heater in grey. The performance of each solution is represented by the average cabin temperature shown as the thin green bar in the middle, in comparison with the target temperature of 20°C .

Figure 110 presents the thermal energy (re)generation (in Wh/km) for different methods. The figure shows the results both with the doors opening model (w/o doors) and the results

without the doors opening model (w/ doors). For chiller, the value represents the amount of energy harvested by the chiller on the coolant side. For PTC, the value represents the amount of energy released from the PTC heater to the heat exchanger. For PCM, the value represents the amount of energy released from the PCM to the coolant. For HP, the value represents the heating power of the internal heat exchanger. It is worth noting that the value only represents the energy (re)generation for each solution in certain configurations – the values for PTC, HP, chiller and PCM are obtained from configuration 1, 2, 3 and 4 respectively.

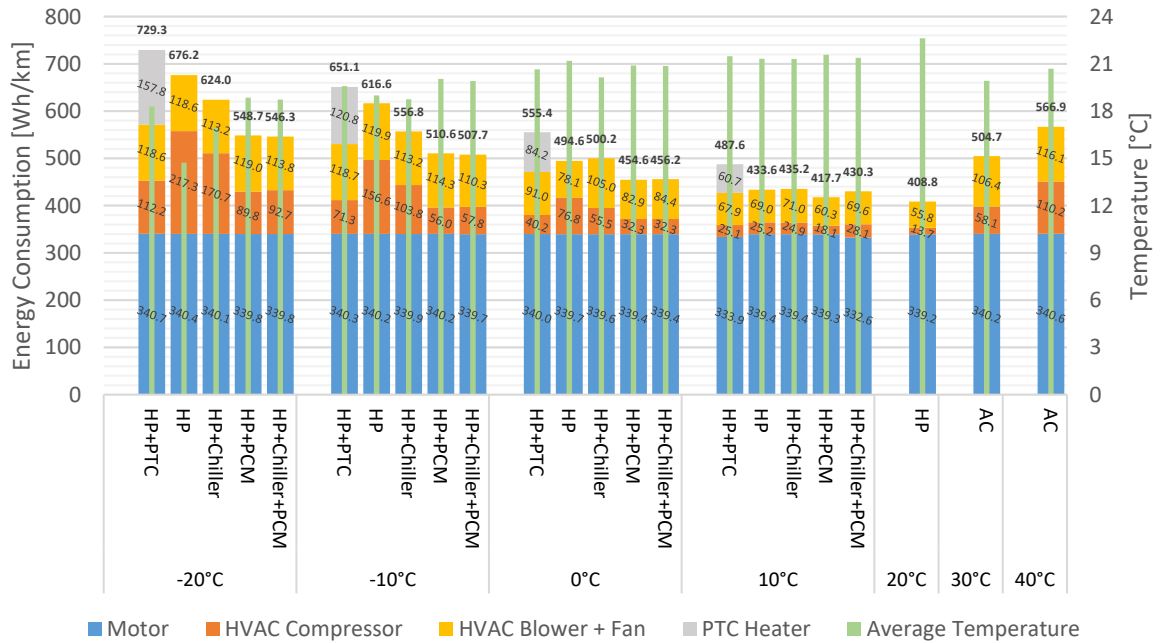


Figure 108. Simulation results of energy consumption and cabin temperature for different thermal management solutions - without doors opening model

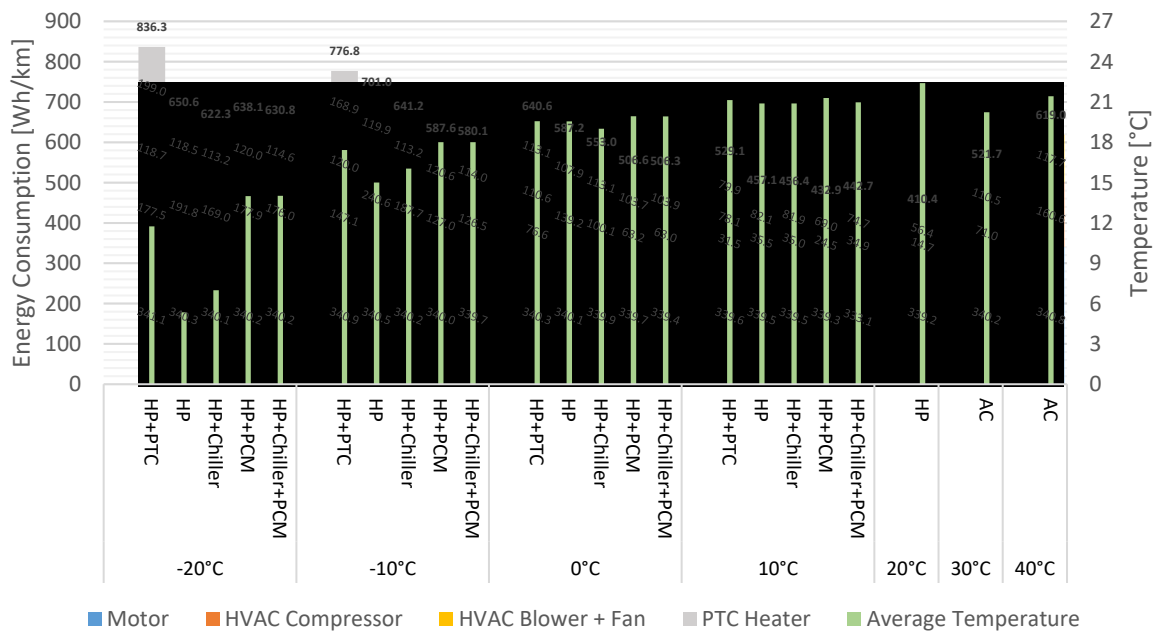


Figure 109. Simulation results of energy consumption and cabin temperature for different thermal management solutions - with doors opening model

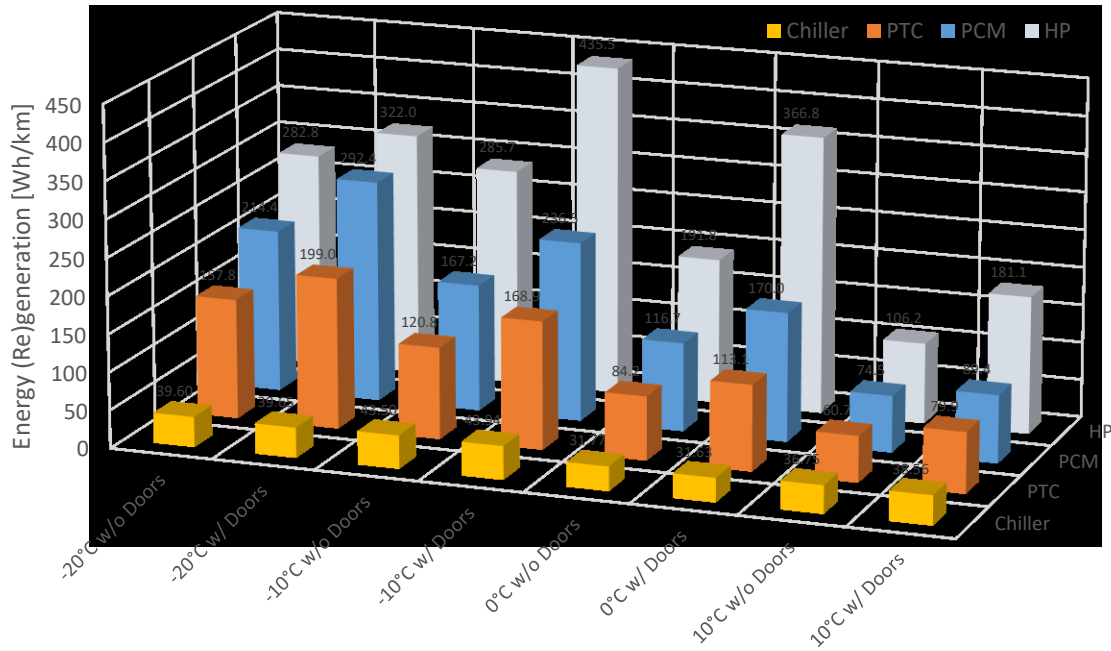


Figure 110. Simulation results for thermal energy (re)generation for different methods

5.3.1 Heat Pump Results

As illustrated in Figure 108 and Figure 109, the power consumption of the heat pump system showing an increasing trend with decreasing ambient temperature, rising from 117.6 Wh/km in 10 °C to 335.9 Wh/km in -20 °C (without the doors opening model).

The average cabin temperature drops with the decrease of ambient temperature. In -20 °C, the average temperature reaches 15 °C without the doors opening model and 5 °C with the model.

The thermal efficiency, which is calculated by dividing the energy generation with energy consumption, drops with the decrease of ambient temperature, which is in agreement with the heat pump characteristics discussed in Section 4.1.1. In 10 °C, the COP is 1.12 and 1.53 respectively without and with doors opening model. In -20 °C, the COP drops to 0.84 and 1.04 respectively.

In the process of showing other thermal management configurations, heat pump configuration could be considered as a benchmark for comparing energy consumption.

5.3.2 PTC Heater Results

As shown in Figure 108 and Figure 109, the power consumption of the HP+PTC configuration increases with decreasing ambient temperature, rising from 153.7 Wh/km in 10 °C to 388.6 Wh/km in -20 °C (without the doors opening model). The energy consumption of the heat pump decrease compared to the HP configuration. However, PTC heater consumes a significant amount of energy, resulting in a higher energy consumption.

The average cabin temperature drops with the decrease of ambient temperature, but with significant improvement compared to the HP configuration. In -20 °C, the average temperature reaches 18.3 °C without the doors opening model and 11.7 °C with the model.

As shown in Figure 110, the heating power of the PTC heater rises with the decrease of ambient temperature, indicating that the heating performance is not affected by the ambient temperature.

In the process of showing other thermal management configurations, HP+PTC configuration could be considered as a benchmark for comparing average cabin temperature (heating performance).

5.3.3 Chiller Results

A heat pump with a chiller (liquid-to-air heat pump) leads to a moderate increase in cabin temperature and a moderate decrease in battery energy consumption compared to HP configuration; yet both of them are not as significant as the HP+PTC configuration.

For the current driving cycle, the chiller could regenerate 30-45 Wh/km of thermal energy from the powertrain cooling loop across all temperatures. It could be speculated that the energy harvesting performance could vary from driving cycles; more power-demanding the cycle is, the more energy could be regenerated by the chiller.

5.3.4 PCM Heating Loop Results

The HP+PCM offers similar, if not better, heating performance compared to the HP+PTC, and is much better than the HP and HP+Chiller configuration, while consume significantly less energy from the battery. The PCM heating loop has a similar heating principle to the PTC heater, releasing 10-50% more thermal energy than PTC heater. The difference between the two methods is that PCM is pre-charged during vehicle charging while only consumes a little amount of additional energy to power the pump in the PCM heating loop. Unlike heat pump, the efficiency for both PCM and PTC is not affected by the temperature; the thermal energy generation is only affected by the heating demand. Hence, PCM and PTC are supplements to the heat pump in cold temperature.

Combining PCM heating loop with chiller, the HP+Chiller+PCM configuration has nearly identical characteristics compared with HP+PCM. In this case, an additional chiller will only marginally reduce the battery energy consumption. The insignificance of chiller is because the heat pump is working much less while using the PCM heating loop.

5.3.5 Doors Opening Model

The energy consumptions of each simulation configuration differ in the simulations with and without the door opening model. The differences are listed in Table 25. The differences are present in percentage which is calculated by $(P_{w.doors} - P_{wo.doors})/P_{wo.doors}$, where $P_{w.doors}$ is the power consumption of thermal management system (in Wh/km) with the doors opening model, and $P_{wo.doors}$ is the power consumption of thermal management system without the doors opening model.

Table 25 Comparison of the power consumption simulation results between the simulation with the door opening model to the simulation without the door opening model

	-20 °C	-10 °C	0 °C	10 °C	20 °C	30 °C	40 °C
HP+PTC	27.41%	40.27%	39.38%	23.29%			
HP/AC	-7.59%	30.40%	59.53%	24.87%	2.36%	10.27%	22.97%
HP+Chiller	-0.60%	38.71%	32.76%	21.94%			
HP+PCM	42.63%	45.36%	45.03%	19.33%			
HP+Chiller+PCM	40.77%	43.07%	42.97%	12.14%			

It could be seen from Table 25 that using the door opening model, the power consumption of the thermal management system could be significantly increased in both cold and hot conditions. Some seemingly odd exceptions are in $-20\text{ }^{\circ}\text{C}$, which will be discussed in Section 5.4. Table 25 demonstrates the importance of considering the thermal effects of air exchange through open doors in bus simulation.

5.3.6 Driving Range

Figure 111 shows the driving range for the battery electric bus simulation model based on the energy consumption; the left and right figures shows the results without and with doors opening model respectively.

The driving range of electric bus depends on the ambient temperature. Using a heat pump, the driving range of the bus would decrease by 49.81 km compared with the simulation result in $20\text{ }^{\circ}\text{C}$ (about 40% range reduction). An additional PTC heater will decrease the driving range further by another 5.54 km (55.35 km or about 44% range reduction). Adding a chiller to the heat pump will improve the driving range in colder temperatures (6.36 km or about 8% increase to heat pump in $-20\text{ }^{\circ}\text{C}$). Using PCM with heat pump could significantly improve range (17.70 km or about 23% increase to heat pump in $-20\text{ }^{\circ}\text{C}$). Using PCM and chiller with heat pump could improve range even more (18.11 km or about 24% increase to heat pump in $-20\text{ }^{\circ}\text{C}$). In mild temperature ($10\text{ }^{\circ}\text{C}$) the benefits of using chiller and PCM are less significant.

Compared to the simulation without the doors opening model, the simulation with the doors opening model results in lower driving range, especially in lower temperatures. From $-20\text{ }^{\circ}\text{C}$ to $40\text{ }^{\circ}\text{C}$, the average range reductions compared to the results from the model without doors opening model are 7.2% in $-20\text{ }^{\circ}\text{C}$, 13.4% in $-10\text{ }^{\circ}\text{C}$, 11.8% in $0\text{ }^{\circ}\text{C}$, 4.8% in $10\text{ }^{\circ}\text{C}$, 4.0% in $20\text{ }^{\circ}\text{C}$, 3.3% in $30\text{ }^{\circ}\text{C}$, 8.4% in $40\text{ }^{\circ}\text{C}$.

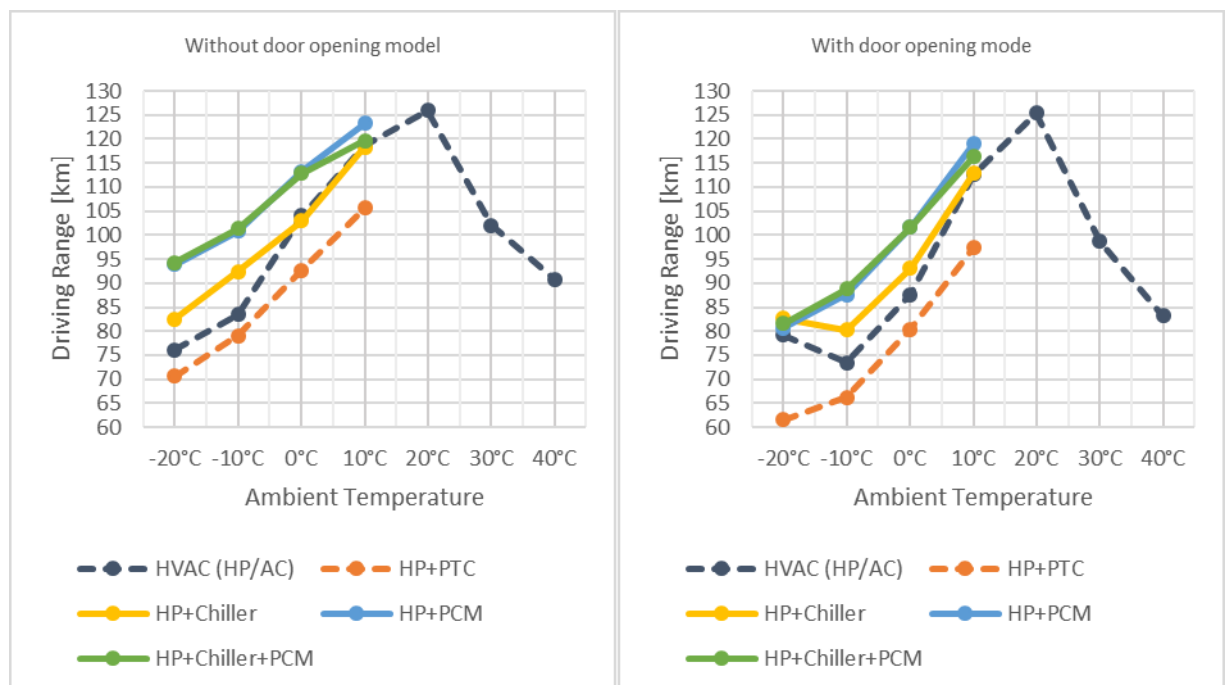


Figure 111. Simulation results of driving range for different thermal management solutions, without and with door opening model

5.4 Results Discussion

The driving range results shown in Figure 111 are in accord with the results from previous studies by Lajunen *et al.* (2017) shown in Figure 112. The blue curve in Figure 112 presents the driving range for an electric passenger car in different ambient temperatures, which is not studied in the thesis because the thesis did not consider the temperature's effects on the powertrain and battery. The red curve in Figure 112 presents the energy consumption of the vehicle with only a PTC heater. The yellow curve in Figure 112 presents the energy consumption of the vehicle with a heat pump and a PTC heater, which is considered in the thesis. The curve shows similar trends compared to the results of corresponding configurations shown in Figure 111.

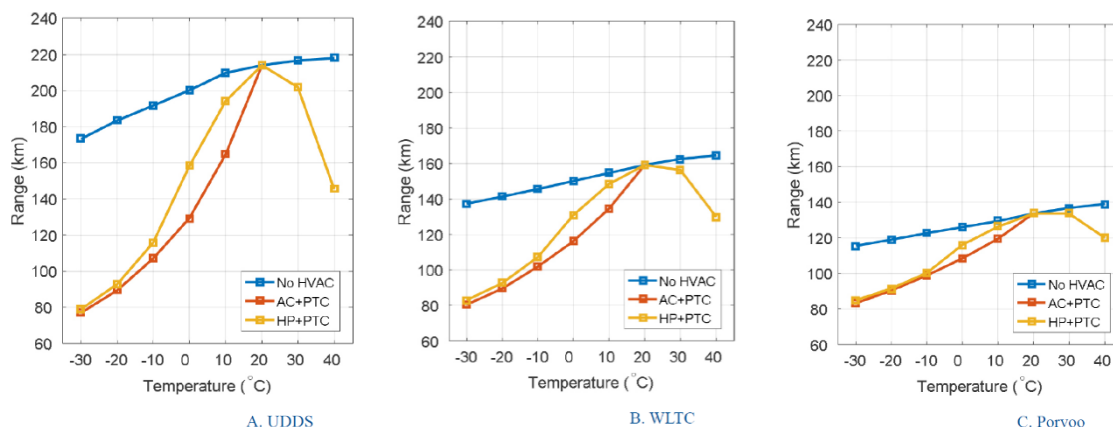


Figure 112 Simulation results of electric vehicle driving range by Lajunen, (2017)

Lajunen *et al.* (2017) did not consider the effects of the doors on the cabin. Inspecting the energy consumption and driving range results with the doors opening model shown in Figure 109 and Figure 111, we could find that there are some inconsistencies of the curve from -10 °C to -20 °C. In -20 °C, the energy consumption of every configurations but HP+PTC does not increase from the values in -10°C by a huge margin, despite higher heating demands; the energy consumption of HP and HP+Chiller configurations is even lower than the corresponding values in -10°C.

The phenomenon could be explained by the compressor regulations shown in Figure 113 and Figure 114, representing the workload of the heat pump.

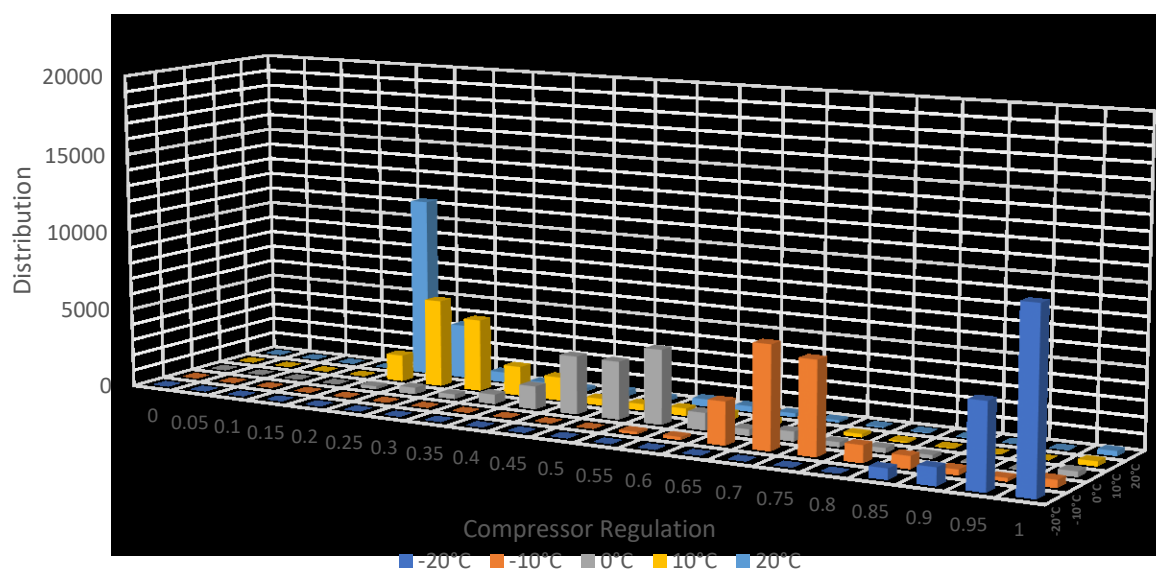


Figure 113. Simulation results of compressor regulation histogram for heat pump - without doors opening model

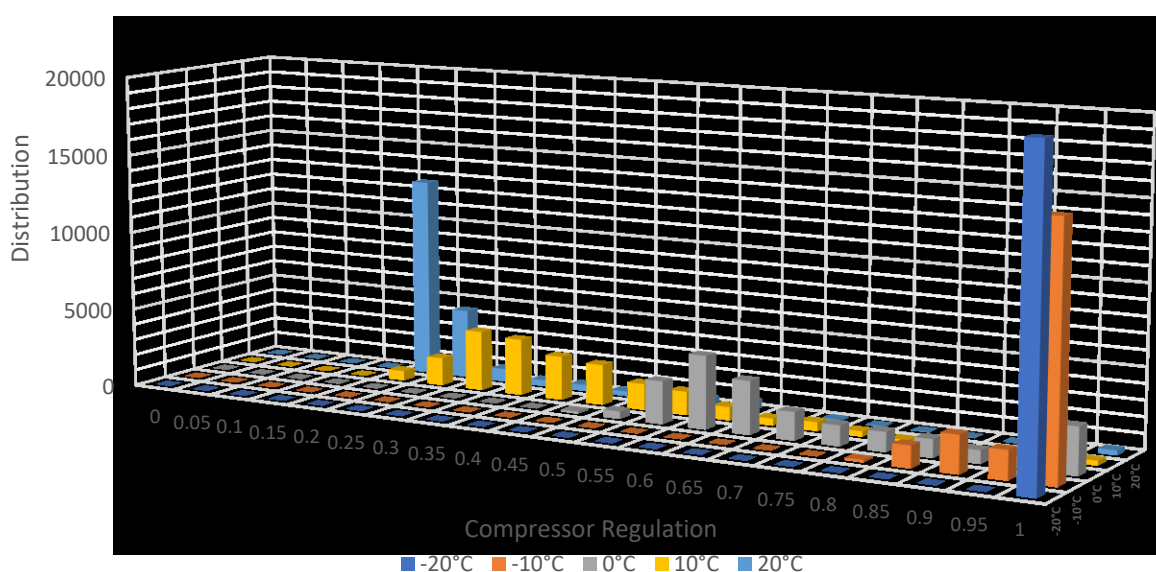


Figure 114. Simulation results of compressor regulation histogram for heat pump - with doors opening model

Comparing Figure 113 and Figure 114, it could be seen that:

- The workload of the heat pump is more concentrated without the doors opening model, and more dispersive with the doors opening model. This is because constant doors opening will disrupt the thermal balance of the cabin.
- The average value of the heat pump is higher with the doors opening model, especially in lower temperatures. For example, in -10 °C the mean value of the compressor regulation distribution is 0.7-0.75 without the doors opening model and 0.95-1.0 with the doors opening model. This is because the cold air pouring into the cabin increase the cabin heating demands.

In -20 °C, the compressor is running at full speed all the time with the doors opening model. Combining with the fact that the average cabin temperature for HP configurations is 5 °C (much lower than the 20 °C target), it could be speculated that the heat pump is reaching its performance limit in -20 °C. Therefore, in -20 °C the energy consumption is not determined by the demand anymore, but rather by the system efficiency. From the discussion about HVAC characteristics in Section 4.1.1, it could be seen that the COP of heat pump drops with decreasing temperature, and maximizing compressor load also leads to lower COP. Therefore, the energy consumption for heat pump configuration is lower than the corresponding values in -10°C, despite the higher heating demands. The explanation could also be applied to other configurations.

6 Conclusion

The thesis has developed a system-level battery electric bus simulation model based on electric bus prototype e-Muuli of VTT using the Siemens AMESim software; the simulation model was validated with various experiments. Based on the battery electric bus simulation model, the thesis further evaluated several innovative thermal management solutions by simulations using real-life driving cycle in various ambient temperatures from -20°C to 40°C .

The simulation model uses multi-level simulation approach and focuses on the details of thermal simulation; the systems that are thermal-related are modelled in detail, such as cabin model and HVAC model.

6.1 Thesis Outcome

The thesis shows the effects of ambient temperature on the energy consumption and driving range of electric city buses, and demonstrate the significance of using various thermal management solutions in improving energy consumption and heating performance.

The simulation results show that using heat pumps in low temperatures will significantly reduce driving range, and the current heat pump model with 11 kW maximum heating power is insufficient in cabin heating in -20°C ambient temperatures due to its efficiency and performance drop in extreme low temperatures. Using an additional 1.5 kW positive energy coefficient or PTC heater, which consume energy from the main battery and generates resistive heat, will overcome the insufficiency in heating performance of the heat pump, but will consume more energy from the main battery, resulting in even less driving range. A chiller (liquid-to-air heat pump), which harvests waste thermal energy from the powertrain cooling loop to the HVAC refrigerant loop, will provide a moderate improvement in both driving range and heating performance in all ambient temperatures. Phase change materials or PCMs provide new possibilities in electric vehicle cabin heating. A 100 kg PCM will store enough thermal energy to heat up the cabin for nearly 4 hours at 2.5 kW heating power; and it could be recharged simultaneously during battery charging. Using a dedicated coolant loop to transfer thermal energy from the PCM in addition to a heat pump, the driving range could be significantly improved, and the heating performance is on par with PTC heater.

The thesis includes a detailed cabin model specifically built for buses. In addition to the effects of solar radiations, human heat dissipation, which are included in previous researches in passenger cars cabin modelling, some unique characteristics for buses are modelled, such as air exchanges through open doors. When the bus is running on a morning rush-hour driving cycle when the doors are opened frequently, the energy consumption of thermal management could be increases by as much as 60% and cause severe range reduction. The final results demonstrate the importance of considering the doors opening model in bus simulations, which previous studies about vehicle system-level simulation has rarely considered.

6.2 Limitations and Recommendations for Future Research

Due to the limitations in time, resource, and knowledge, there are many parts of the thesis work that could still be improved.

- Improving Powertrain and Auxiliary Simulation: The powertrain models (especially the motor and inverter) could be fined tuned. More auxiliary load, such as the air compressor,

power steering, and lightings should be included. Visualization tools such as the energy flow diagram could be included in future iterations of the model.

- **Improving Cabin Model:** Currently utilised mono-zonal model is limited to a single input and a single output, which will cause inaccuracy for the intake air properties of the HVAC model due to the air stratification effects. In future work, a multi-zonal lumped-parameter cabin model or a CFD model need to be implemented, which could simulate the difference of air properties inside the cabin and provide a more accurate input to the HVAC simulation. The doors opening model should be improved with more CFD simulations and real-world measurements.
- **Improving Thermal Management Solutions:** The thermal management solutions that are currently considered in the thesis could be modelled in better detail, and validated with real-world experiments. More solutions and cooperation between solutions should be included. For example, the waste heat collected by the chiller could be stored in the PCM.
- **Including Charging:** Models of the charger should be included to perform simulations on real-world full-day driving cycles. On-board charger is also a part of thermal management systems. In e-Muuli, the 24-kW on-board charger (converter) that converts 3 phase AC to DC will generate waste heat during charging that is used for cabin (pre)heating. Additionally, the thermal energy storage devices, such as the phase change material, could also be charged during the charging time, as discussed in Section 5.1.3.
- **Including Other Contributing Factors:** During the modelling and simulations, there are a number of contributing factors that are set to constants, and thus their effects on the simulation results are not investigated. Additional work could be done to investigate the effects of contributing factors such as the solar radiation and vehicle heading angle, as well as initial system temperatures.

Reference

- Aalto IT (2019) *outside.aalto.fi*. Available at: <http://outside.aalto.fi/> (Accessed: 27 June 2019).
- Andersson, C. (2004) *On auxiliary systems in commercial vehicles, Simulation*. Available at: <http://www.iea.lth.se/publications/Theses/LTH-IEA-1039.pdf>.
- Brèque, F. and Nemer, M. (2017) ‘Cabin Thermal Needs: Modeling and Assumption Analysis’, *Proceedings of the 12th International Modelica Conference, Prague, Czech Republic, May 15-17, 2017*, 132, pp. 771–781. doi: 10.3384/ecp17132771.
- Carrier (2019) *Heat Pump vs Air Conditioners*. Available at: <https://www.carrier.com/residential/en/us/products/heat-pumps/heat-pumps-vs-air-conditioners/>.
- Cengel, Y. A. and Boles, M. A. (2004) *Thermodynamics - an engineering approach 5th edition*. Available at: <https://cruncheez.files.wordpress.com/2015/06/thermodynamics-an-engineering-approach-5th-edition.pdf>.
- Chowdhury, S. *et al.* (2018) ‘Total Thermal Management of Battery Electric Vehicles (BEVs)’, (June), pp. 6–8. doi: 10.4271/2018-37-0026.
- Dartmouth College (2019) *Specific Heat and Latent Heat*. Available at: <http://www.dartmouth.edu/~ears5/handouts/heat.html> (Accessed: 18 June 2019).
- Eberspächer (2019) *Eberspächer - Exhaust technology, Vehicle Heaters, Automotive Electronics*. Available at: <https://www.eberspaecher.com>.
- Erkkilä, K. *et al.* (2013) ‘eBUS -Electric bus test platform in Finland’, in *ESV27*.
- Fiala, D. (1998) ‘Dynamic Simulation of Human Heat Transfer and Thermal Comfort (Poster)’, 45(2001), p. 1.
- Göhlich, D. *et al.* (2018a) ‘Design of urban electric bus systems’, *Design Science*, 4, p. e15. doi: 10.1017/dsj.2018.10.
- Göhlich, D. *et al.* (2018b) ‘Design of urban electric bus systems’, *Design Science*, 4, p. e15. doi: 10.1017/dsj.2018.10.
- Havenith, G. *et al.* (1998) ‘Relevance of individual characteristics for human heat stress response is dependent on exercise intensity and climate type’, *European Journal of Applied Physiology and Occupational Physiology*, 77(3), pp. 231–241. doi: 10.1007/s004210050327.
- HSL (2018) ‘Clean and quiet - 35 new electric buses to enter service’, pp. 2018–2019.
- Ianniciello, L., Biwolé, P. H. and Achard, P. (2018) ‘Electric vehicles batteries thermal management systems employing phase change materials’, *Journal of Power Sources*. Elsevier, 378(October 2017), pp. 383–403. doi: 10.1016/j.jpowsour.2017.12.071.
- International Energy Agency (2018) ‘Global EV Outlook 2018’, *Global EV Outlook 2018*. doi: 10.1787/9789264302365-en.
- Jeong, J. W. and Lee, Y. L. (2015) ‘A study on the efficiency of high voltage ptc heaters for electric vehicles’, *ARPN Journal of Engineering and Applied Sciences*, 10(6), pp. 2504–2508.

- Kim, K. Y., Kim, S. C. and Kim, M. S. (2012) 'Experimental studies on the heating performance of the PTC heater and heat pump combined system in fuel cells and electric vehicles', *International Journal of Automotive Technology*, 13(6), pp. 971–977. doi: 10.1007/s12239-012-0099-z.
- Kiss, T., Lustbader, J. and Leighton, D. (2015) 'Modeling of an Electric Vehicle Thermal Management System in MATLAB/Simulink', *SAE Technical Paper Series*, 1(April), pp. 21–23. doi: 10.4271/2015-01-1708.
- Lajunen, A. (2017) 'Energy Efficiency and Performance of Cabin Thermal Management in Electric Vehicles', *SAE Technical Papers*, 2017-March(March). doi: 10.4271/2017-01-0192.
- Lajunen, A. *et al.* (2017) 'Thermal energy storage for increasing heating performance and efficiency in electric vehicles', *2017 IEEE Transportation and Electrification Conference and Expo, ITEC 2017*. IEEE, pp. 95–100. doi: 10.1109/ITEC.2017.7993253.
- Lajunen, A. and Kalttonen, A. (2015) 'Investigation of thermal energy losses in the powertrain of an electric city bus', *2015 IEEE Transportation Electrification Conference and Expo, ITEC 2015*. doi: 10.1109/ITEC.2015.7165776.
- Lajunen, A. and Lipman, T. (2016) 'Lifecycle cost assessment and carbon dioxide emissions of diesel, natural gas, hybrid electric, fuel cell hybrid and electric transit buses', *Energy*. Elsevier Ltd, 106, pp. 329–342. doi: 10.1016/j.energy.2016.03.075.
- Lam, J. C. and Li, D. H. W. (1996) 'Luminous efficacy of daylight under different sky conditions', *Energy Conversion and Management*, 37(12), pp. 1703–1711. doi: 10.1016/0196-8904(96)00021-0.
- Laurikko, J. *et al.* (2015) 'Electric city bus and infrastructure demonstration environment in Espoo, Finland', *EVS28 International Electric Vehicle Symposium and Exhibition*, pp. 1–11.
- Leong, J. C. *et al.* (2011) 'Cabin heat removal from an electric car', *World Electric Vehicle Journal*, 4(1), pp. 760–766.
- Li, W. and Sun, J. (2013) 'Numerical simulation and analysis of transport air conditioning system integrated with passenger compartment', *Applied Thermal Engineering*. Elsevier Ltd, 50(1), pp. 37–45. doi: 10.1016/j.applthermaleng.2012.05.030.
- Li, X., Castellanos, S. and Maassen, A. (2018) 'Emerging trends and innovations for electric bus adoption—a comparative case study of contracting and financing of 22 cities in the Americas, Asia-Pacific, and Europe', *Research in Transportation Economics*. Elsevier, 69(June), pp. 470–481. doi: 10.1016/j.retrec.2018.06.016.
- Liddament, M. (1986) 'Air Filtration Calculation Techniques: An Application Guide'.
- Lindh, P. *et al.* (2019) 'Direct Liquid Cooling Method verified with a Permanent-Magnet Traction Motor in a Bus', *IEEE Transactions on Industry Applications*, (April), pp. 1–1. doi: 10.1109/TIA.2019.2908801.
- Littlefair, P. J. (1985) 'The luminous efficacy of daylight: a review', *Lighting Research & Technology*, 17(4), pp. 162–182. doi: 10.1177/14771535850170040401.
- Mahmoud, M. *et al.* (2016) 'Electric buses: A review of alternative powertrains', *Renewable and Sustainable Energy Reviews*, 62, pp. 673–684. doi: 10.1016/j.rser.2016.05.019.

- Mahmud, K. and Town, G. E. (2016) 'A review of computer tools for modeling electric vehicle energy requirements and their impact on power distribution networks', *Applied Energy*. Elsevier Ltd, 172, pp. 337–359. doi: 10.1016/j.apenergy.2016.03.100.
- Marcos, D. *et al.* (2014) 'The development and validation of a thermal model for the cabin of a vehicle', *Applied Thermal Engineering*. Elsevier Ltd, 66(1–2), pp. 646–656. doi: 10.1016/j.applthermaleng.2014.02.054.
- Mater, A. *et al.* (2016) 'Thermal management model for a Plug-In Hybrid Electric Vehicle'.
- Mitalas, G. P. and Stephenson, D. G. (1962) 'Absorption and Transmission of Thermal Radiation by Single and Double Glazed Windows'.
- Nassajfar, M. N. (2018) *CFD Simulation of Electric Vehicle Thermal System and Investigation of Thermal Insulation for Cabin*. Lappeenranta University of Technology.
- Niu, W., Lai, X. and Wei, C. (2018) '汽车空调热力膨胀阀的标定及验证方法', 华东科技: 学术版, (1), p. 380.
- Pihlatie, M. *et al.* (2015) 'Fully electric city buses - The viable option', *2014 IEEE International Electric Vehicle Conference, IEVC 2014*. doi: 10.1109/IEVC.2014.7056145.
- Du Pont (2015) 'HCFC-123'.
- Qi, Z. (2014) 'Advances on air conditioning and heat pump system in electric vehicles - A review', *Renewable and Sustainable Energy Reviews*. Elsevier, 38, pp. 754–764. doi: 10.1016/j.rser.2014.07.038.
- Raghunatha Reddy, D. V, Bhramara, P. and Govindarajulu, K. (2015) 'Performance prediction of a vapor compression refrigeration system with fuzzy modeling', (May). Available at: https://www.researchgate.net/profile/D_V_Reddy/publication/302909030_Performance_prediction_of_a_vapor_compression_refrigeration_system_with_fuzzy_modeling/links/57331f4108ae9f741b260a59/Performance-prediction-of-a-vapor-compression-refrigeration-system-w.
- Rashid, A., Hofman, T. and Rosca, B. (2018) 'Enhanced Battery Thermal Management Systems with Optimal Charge Control for Electric Vehicles', *Proceedings of the American Control Conference*. AACC, 2018-June, pp. 1849–1854. doi: 10.23919/ACC.2018.8431216.
- Reif, K. (2004) *Automotive Mechatronics*. doi: 10.1016/j.conengprac.2003.10.004.
- Schenubel, M. (2017) *Automotive Heating & Air Conditioning*. 6th Editio. Waterbury, Connecticut: Cengage Learning.
- Shahidinejad, S., Bibeau, E. and Filizadeh, S. (2012) 'Design and Simulation of a Thermal Management System for Plug-In Electric Vehicles in Cold Climates'. doi: 10.4271/2012-01-0118.
- Siemens (2019) 'Siemens AMESim 17.0 Documentation'.
- Smith, J. *et al.* (2018) 'Battery thermal management system for electric vehicle using heat pipes', *International Journal of Thermal Sciences*. Elsevier, 134(June 2017), pp. 517–529. doi: 10.1016/j.ijthermalsci.2018.08.022.
- Stanfield, C. and Skaves, D. (2017) *Fundamentals of HVACR*. 3rd Editio. Edited by A.

Gilfillan.

Tonada (2019a) *Konvekta H11-002-206 Replacements, Tonada EC Blowers 24V--Hispacold, Spal, EBM, Tonada EC Fans & EC Blowers*. Available at: <http://www.tonada.cn/?Products/Blowers/150.html> (Accessed: 17 June 2019).

Tonada (2019b) *SPAL VA89-BBL300-94A Replacement, Tonada EC Fans 24V, 305MM--Hispacold, Spal, EBM, Tonada EC Fans & EC Blowers*. Available at: <http://www.tonada.cn/?Products/Product52/161.html> (Accessed: 17 June 2019).

Torregrosa-Jaime, B. *et al.* (2015) ‘Transient thermal model of a vehicle’s cabin validated under variable ambient conditions’, *Applied Thermal Engineering*, 75, pp. 45–53. doi: 10.1016/j.applthermaleng.2014.05.074.

Wang, M. *et al.* (2016) ‘Design and Testing of a Thermal Storage System for Electric Vehicle Cabin Heating’, *SAE Technical Paper Series*, 1, pp. 1–7. doi: 10.4271/2016-01-0248.

Wang, M. *et al.* (2017) ‘Integration and Validation of a Thermal Energy Storage System for Electric Vehicle Cabin Heating’, *SAE Technical Paper Series*, 1. doi: 10.4271/2017-01-0183.

Webasto (2017) *Webasto: Webasto at the Busworld 2017*. Available at: <https://www.webasto.com/index.php?id=11463&articleId=910> (Accessed: 10 June 2019).

Webasto (2019) *Air Heaters for Heavy-duty Trucks*. Available at: <https://www.webasto-comfort.com/en-us/heating-solutions/heavy-duty-truck/air-heaters/>.

Wirth, S., Eimler, M. and Niebling, F. (2014) *Thermal Insulation of Electric Vehicle Cabins*, *Auto Tech Review*. doi: 10.1365/s40112-014-0521-1.

Zhang, Z. *et al.* (2018a) ‘The solutions to electric vehicle air conditioning systems: A review’, *Renewable and Sustainable Energy Reviews*. Elsevier Ltd, 91(February), pp. 443–463. doi: 10.1016/j.rser.2018.04.005.

Zhang, Z. *et al.* (2018b) ‘The solutions to electric vehicle air conditioning systems: A review’, *Renewable and Sustainable Energy Reviews*. Elsevier Ltd, 91(August 2015), pp. 443–463. doi: 10.1016/j.rser.2018.04.005.

Zhu, S., Demokritou, P. and Spengler, J. (2010) ‘Experimental and numerical investigation of micro-environmental conditions in public transportation buses’, *Building and Environment*, 45(10), pp. 2077–2088. doi: 10.1016/j.buildenv.2010.03.004.